Investigations and modeling of droplet behavior and heat transfer under post-dryout conditions

Zur Erlangung des akademischen Grades einer
DOKTORIN DER INGENIEURWISSENSCHAFTEN (Dr.-Ing.)

von der KIT-Fakultät für Maschinenbau des
Karlsruher Instituts für Technologie (KIT)

genehmigte

DISSERTATION

von

M. Sc. Zihan Xia

Tag der mündlichen Prüfung: 21.08.2025

Hauptreferent: Prof. Dr.-Ing. Xu CHENG

Korreferent: Prof. Dr. Seiichi KOSHIZUKA

Acknowledgements

Completing a PhD is a journey filled with challenges, growth, and discovery. There were moments of excitement when model and experiments worked as expected, and moments of frustration when progress seemed slow. Reflecting on the past five years, every step I took contributed to shaping both my scientific skills and personal character.

Foremost, I wish to express my most sincere and profound gratitude to my supervisor, Prof. Xu Cheng. Throughout my doctoral studies, his guidance has always been insightful, timely, and unfailingly correct. What truly distinguishes him is the extraordinary dedication he demonstrates toward PhD students. His visionary thinking, rigorous scientific attitude, and relentless passion for research have not only shaped this PhD work but have also inspired me to pursue excellence in my own academic endeavors. I am forever indebted to him for his patience, generosity, and unwavering belief in my potential.

I would also like to express my sincere gratitude to my co-supervisor, Prof. Seiichi Koshizuka, for his extraordinary patience and professionalism in reviewing my thesis. He overcame many difficulties to attend my defense, providing invaluable advice and wholehearted encouragement. His guidance and support have been instrumental in shaping the final outcome of this work, and I am deeply grateful for his trust and recognition.

I am deeply grateful to my colleagues at the Institute for Applied Thermofluidics (IATF). When I first arrived in Germany at the beginning of the pandemic, everything was in lockdown and I felt extremely isolated. During that difficult time, my colleagues offered me invaluable support, helping me to get through those lonely months. Later, in both research and daily work, they have always been generous with their time, knowledge, and encouragement. Their kindness and selfless help not only made my life here much easier, but also created an environment in which I could truly grow as a researcher.

Finally, I owe my heartfelt thanks to my family and friends. Their unconditional love, patience, and encouragement have been my anchor throughout the highs and lows of this journey. Their belief in me gave me the strength to persevere and complete this work.

To everyone who has supported, guided, and encouraged me along the way, I extend my sincerest gratitude—this thesis would not have been possible without you.

Zihan Xia
Karlsruhe, 15.09.2025

Abstract

During flow boiling, occurrence of dryout leads to deteriorated heat transfer and a dramatic increase in the temperature of the heated surface. The heat transfer mechanism in the post-dryout (PDO) region significantly influences the peak wall temperature, which is critical for maintaining the structural integrity of heat exchange devices. Over the past five decades, extensive research focused on PDO heat transfer, resulting in numerous experimental studies, empirical correlations and mechanistic models. While empirical correlations are widely used, mechanistic models offer better generalizability for predicting wall temperature by describing the individual heat transfer processes in the PDO region. However, the predictive accuracy of the interfacial heat transfer remains challenging due to the complex dynamics of droplets.

In this study, an integrated approach combining three-dimensional numerical simulations and visualization experiments is employed. The findings from CFD (Computational Fluid Dynamics) simulations and experimental studies are integrated to improve the predictive accuracy of interfacial heat transfer, enabling a more sophisticated, physical phenomena-based mechanistic model for PDO heat transfer prediction.

CFD simulations are performed to investigate post-dryout heat transfer, with the focus on elucidating droplet dynamics and interfacial heat transfer mechanisms. It is found that the droplet evaporation in the near-wall region is significant compared with the overall evaporation rate. The strong evaporation in the near-wall region also hinders droplet deposition from the central region toward the wall. Based on these findings, a two-region approach is developed to predict the interfacial heat transfer to capture the distinct evaporation difference in the near-wall and the central regions. Dimensionless radial profiles of vapor temperature and velocity, extracted from the simulations, are incorporated to capture the lateral droplet transport and the non-uniform evaporation.

Complementary flow visualization experiments in PDO conditions enable the measurement of droplet size and velocity, contributing to the extension of existing limited droplets database and the development of refined correlations of droplet size. The experimental results reveal that droplets radial velocity follows a normal distribution, while axial velocity exhibits a shifted normal distribution, both are strongly influenced by working pressure and mass flux. Droplet size is observed to decrease as pressure increases. Additionally, a decreasing trend in droplet size is observed with the increase in local steam quality. Based on these findings, a new droplet size correlation is derived, incorporating the Weber number, the density ratio, and the vapor Reynolds number.

An advanced mechanistic model for PDO heat transfer is developed, by integrating the new two-layer methodology, the improved models related to the interfacial heat transfer and the droplet dynamics into an existing mechanistic model. The proposed PDO model has been validated against nearly 8,000 data points from both water and R-134a experiments, demonstrating its high predictive accuracy and robustness across a wide range of parameters.

Zusammenfassung

Während des Strömungssiedens führt das Auftreten des Austrocknens einer beheizten Oberfläche (Dryout) zu einer Verschlechterung des Wärmeübergangs und einem drastischen Anstieg der Oberflächentemperatur. Der Wärmeübertragungsmechanismus in der Post-Dryout-(PDO-)Region beeinflusst maßgeblich die maximale Wandtemperatur, was entscheidend für die strukturelle Integrität von Wärmeüberträgern ist. In den letzten fünf Jahrzehnten wurde intensiv zur Wärmeübertragung in der PDO-Region geforscht, was zu zahlreichen experimentellen Studien, empirischen Korrelationen und mechanistischen Modellen geführt hat. Während empirische Korrelationen weit verbreitet sind, bieten mechanistische Modelle eine bessere Generalisierbarkeit für die Vorhersage der Wandtemperatur, da sie die einzelnen Wärmeübertragungsprozesse in der PDO-Region physikalisch beschreiben. Die genaue Vorhersage des Wärmeübergangs an der Phasengrenze zwischen dem Dampf und der Flüssigkeit bleibt jedoch aufgrund der komplexen Dynamik der Tröpfchen eine Herausforderung.

In dieser Arbeit wird ein integrierter Ansatz verfolgt, der dreidimensionale numerische Simulationen mit Visualisierungsexperimenten kombiniert. Die Ergebnisse der CFD-Simulationen (Computational Fluid Dynamics) und der Experimente werden zusammengeführt, um die Genauigkeit der Vorhersage des interphasischen Wärmeübergangs zu verbessern und ein fortschrittlicheres, physikalisch fundiertes mechanistisches Modell zur Beschreibung der Wärmeübertragung in der PDO-Region zu entwickeln.

Die CFD-Simulationen dienen der Untersuchung der Wärmeübertragung nach dem Dryout, mit besonderem Fokus auf die Dynamik der Tröpfchen und die Mechanismen des interphasischen Wärmeübergangs. Es zeigt sich, dass die Tröpfchenverdampfung in wandnahen Bereichen im Vergleich zur Gesamtverdampfung von erheblicher Bedeutung ist. Diese erhöhte Verdampfung verhindert auch die Ablagerung von Tröpfchen aus der zentralen Strömungsregion zur Wand hin. Auf Grundlage dieser Erkenntnisse wird ein Zwei-Zonen-Ansatz entwickelt, um die unterschiedliche Verdampfung in wandnahen und zentralen Bereichen zu erfassen. Zur Erfassung des lateralen Tröpfchentransports und der inhomogenen Verdampfung werden dimensionslose radiale Profile der Dampftemperatur und -geschwindigkeit aus den Simulationen einbezogen.

Ergänzende Strömungsvisualisierungsexperimente unter PDO-Bedingungen ermöglichen die Messung der Tröpfchengröße und -geschwindigkeit, erweitern die bislang begrenzte Tröpfchendatenbank und tragen zur Entwicklung verfeinerter Korrelationen der Tröpfchengröße bei. Die experimentellen Ergebnisse zeigen, dass die radiale Geschwindigkeit der Tröpfchen einer Normalverteilung folgt, während die axiale Geschwindigkeit eine verschobene Normalverteilung aufweist. Beide Größen werden stark vom Systemdruck und vom Massenstrom beeinflusst. Es wird beobachtet, dass die Tropfengröße mit zunehmendem Druck abnimmt. Darüber hinaus zeigt sich ein abnehmender Trend der Tropfengröße mit der Erhöhung der lokalen Dampfqualität. Auf dieser Basis wird eine neue Korrelation zur Vorhersage der Tröpfchengröße abgeleitet, welche die Weber-Zahl, das Dichteverhältnis und die Reynolds-Zahl des Dampfes berücksichtigt.

Ein fortschrittliches mechanistisches Modell für die Wärmeübertragung in der PDO-Region wird somit entwickelt, indem die neue Zwei-Zonen-Methodik sowie die verbesserten Modelle zum interphasischen Wärmeübergang und zur Tröpfchendynamik in ein bestehendes mechanistisches Modell integriert werden. Das vorgeschlagene PDO-Modell wurde anhand von fast 8.000 Datenpunkten aus Experimenten mit Wasser sowie R-134a validiert und zeigt eine hohe Vorhersagegenauigkeit und Robustheit über einen weiten Parameterbereich hinweg.

Contents

List of Figures

List of Tables

Nomenclature

General

Symbol	*Dimensions*	*Description*
A	$[m^2]$	surface area
A_{cont}	$[m^2]$	contact area of droplets and wall during collision
a	$[-]$	coefficient relating the drag effect
b	$[-]$	$(3\rho_v)/(2\rho_d + \rho_v)$, vapor acceleration
b_0	$[-]$	value determined by energy balance
b_1	$[-]$	constant for radial profile of dimensionless velocity
Bo	$[-]$	Boiling number
c	$[-]$	deviation factor from steady-state flow
c_{ofu}	$[-]$	coefficient for vapor velocity profile
c_{ow}	$[-]$	constant
c_p	$[J/(kg \cdot K)]$	heat capacity
C	$[kg/m^3]$	droplet concentration
C_D	$[-]$	drag coefficient
C_f	$[-]$	wall friction coefficient
d	$[m]$	droplet diameter
d_{p0}	$[m]$	droplet diameter at injection in CFD simulation
D_0	$[m]$	droplet diameter before impact
D_{max}	$[m]$	droplet maximum spreading diameter
D_t	$[m]$	tube diameter
$\vec{F}$	$[N]$	additional force
G	$[kg/(m^2 \cdot s)]$	mass flux
h	$[W/(m^2 \cdot K)]$	heat transfer coefficient
h_{lg}	$[J/kg]$	latent heat
H_{wd}	$[m]$	droplet center-point to wall distance

k	$[m^2/s^2]$	turbulent kinetic energy
k_d	$[m/s]$	droplet deposition velocity
k_l	$[W/(m \cdot K)]$	thermal conductivity of liquid droplet
k_Θ	$[-]$	Von Kármán constant= 0.41
K_{vd}	$[-]$	correction factor $(0, 1)$
L	$[m]$	heated length
m_d	$[kg/s]$	droplet mass flow rate
$\dot{m}_d$	$[kg/(m^2 \cdot s)]$	droplet mass flux
m_{dep}	$[kg/s]$	droplet deposition mass flow rate
n_d	$[1/m^3]$	droplet number per volume
n_{dep}	$[/m^2 \cdot s]$	droplet number per volume
Nu	$[-]$	Nusselt number
P	$[Pa]$	pressure
P_R	$[-]$	Reduced pressure
Pr	$[-]$	Prandtl number
Q	$[J]$	heat
q	$[W]$	heat power
q''	$[W/m^2]$	heat flux
r	$[m]$	distance to tube centerline
r_0	$[m]$	radius of tube
r_c	$[m]$	separation line of flow regions
Re	$[-]$	Reynolds number
Re_d	$[-]$	relative Reynolds number
S	$[-]$	slip ratio, u_v/u_d
t	$[s]$	time
t_d	$[s]$	droplet-wall contact time
T	$[K]$	temperature
T^+	$[-]$	dimensionless temperature: $(T_v - T_w)/T^*$, $T^* = -q_w/(\rho c_p u^*)$
T_d	$[K]$	droplet temperature
T_v	$[K]$	vapor temperature
T_w	$[K]$	wall temperature
u	$[m/s]$	time-avg velocity in streamline direction
$\vec{u}_d$	$[m/s]$	droplet velocity
$\vec{u}_v$	$[m/s]$	instantaneous vapor velocity

$\bar{u}_v$	$[m/s]$	time-averaged vapor velocity
u_v	$[m/s]$	u-direction vapor velocity component
u^*	$[m/s]$	shear/friction velocity
u^+	$[-]$	dimensionless velocity, $u^+ = u_v/u^*$
u', v', w'	$[m/s]$	fluctuation velocities in u, v, w
v'	$[m/s]$	fluctuation velocity in radial direction
v'^+	$[-]$	v'/u^*
We	$[-]$	Weber number
x	$[-]$	steam quality
x_d	$[m]$	droplet position in CFD simulation
y	$[m]$	distance from wall
y^+	$[-]$	dimensionless distance from wall, $y^+ = yu^*/(\mu_v/\rho_v)$
z	$[m]$	height position

Greek

α	$[-]$	void fraction
Δt	$[s]$	time step
ΔT_w	$[K]$	wall superheating, $T_w - T_s$
Δz	$[m]$	elevation change between two iterations
ϵ	$[m^2/s]$	turbulent diffusivity
η_b	$[-]$	amplitude ratio at boundary edge
η_e	$[-]$	fluctuation amplitude ratio in turbulent core
λ	$[W/(m \cdot K)]$	thermal conductivity
μ	$[Pa \cdot s]$	dynamic viscosity
μ_g	$[Pa \cdot s]$	molecular viscosity of vapor
μ_l	$[Pa \cdot s]$	molecular viscosity of liquid droplet
ρ	$[kg/m^3]$	density
ρ_d	$[kg/m^3]$	droplet density
ρ_g	$[kg/m^3]$	vapor density
σ	$[N/m]$	surface tension
τ_+	$[-]$	dimensionless particle relaxation time
ζ	$[-]$	random value in range $(-1, 1)$
π	$[-]$	constant 3.1415...

Subscripts & Superscripts

Symbol	*Description*
0	base
1	value after iteration
a	actual value
c	central region
c-n	from central region to near-wall region
cr	separation between central region and near wall region
cw	separation between wall boundary region and transition region
d	droplet
dep	deposition
dev	developing post-dryout region
do	dryout
e	equilibrium
g	gas
in	inlet
l	liquid
n	near wall region
nt	transition region
nw	wall boundary region
s	saturation
t	tube
tr	transition between regions
v	vapor
vb	vapor at the bulk temperature
vc	vapor at the central region
vd	vapor to droplet
vn	vapor at the near wall region
vs	vapor at saturation temperature
vw	vapor at the wall temperature
vwb	vapor at average of wall and bulk vapor temperature
w	wall
wv	wall to vapor
y^+	value at the position of y^+
$-$	between

Abbreviations

Abbreviation	*Full Form*
ATHLET	Analysis of THermal-hydraulics of LEaks and Transients
BWR	Boiling Water Reactor
CFD	Computational Fluid Dynamics
CHF	Critical Heat Flux
DC	Direct Currency
DFFB	Dispersed Flow Film Boiling
DPM	Dispersed Particle Method
HTC	Heat Transfer Coefficient
KIMOF	KIT Model Fluid Facility
KIT	Karlsruhe Institute of Technology
KTH	Royal Institute of Technology
LED	Light-Emitting Diode
ME	Mean Error
PDO	Post-DryOut
PDF	Probability Distribution Function
PWR	Pressurized Water Reactor
RMS	Root-Mean-Square
VOF	Volume of fraction
UDF	User Defined Function

1. Introduction

During the operation of heating exchange systems like thermal power plants and nuclear power reactors, the deterioration of heat transfer could happen on the heated surface. For example, when the surface heat power increases or the working fluid flow rate decreases, the evaporated liquid forms a vapor core in the tube center while the left liquid forms an annular liquid film. As the liquid film evaporates all its mass, the heated surface can no longer be covered by the liquid. The heat transfer mechanism suddenly change at this moment. The sharp drop in the heat transfer coefficient causes a sharp rise in the wall temperature of the heated surface. This phenomenon is called *dryout*. After the occurrence of dryout, the liquid exists only in the form of droplets and no continuous liquid can cover the heated surface anymore. The region beyond the dryout point is called *post-dryout* (PDO) region. The flow pattern in the PDO region is figured out as *dispersed flow*. Vapor conducts convective heat exchange with the heated surface and becomes superheated. The liquid droplets are dispersed in the superheated vapor at a saturated temperature. Driven by the temperature difference between droplets and vapor, the heat is transferred from the superheated vapor to droplets, which slows down the process of vapor superheating, thus affecting the developing trend of wall temperature after dryout. Therefore, figuring out the heat transfer mechanism in the PDO region is important in determining the wall temperature trend and the maximum wall temperature during the process of thermal dynamic design and safety analysis for heat transfer systems.

1.1 Post-dryout Heat Transfer

As shown in Figure 1.1, when the working fluid flows inside the tube with heating, the liquid is heated up and evaporated into vapor as small bubbles. As the heating length increases, the bubbles grow up and merge with the surrounding bubbles into a vapor core in the centerline of the tube with high velocity. The left liquid forms a liquid film covering the heating surface. This flow pattern is named as *annular flow*. During the process of annular flow, the velocity difference between the vapor core and the liquid film brings a shear stress force on the interfacial surface. The liquid is continuously entrained from the liquid film to the vapor core. This process is called *entrainment*. The entrained liquid forms droplets. Since the vapor temperature in annular flow is still at saturated temperature, there is no evaporation of droplets. But the droplets may not remain stable owing to aerodynamic behaviors like break-up into small sizes and deposition. One theory for break-up mechanism is that the droplet Weber number exceeds the free stream critical

Weber number (Hynek, 1969b). The droplet size and distribution change as the break-up, deposition, and entrainment process progresses. Further downstream of the flow, the thickness of the liquid film gradually decreases due to evaporation and entrainment. When the liquid film is completely depleted, the temperature of heated surface jumps to a significantly high value. This point marks the onset of dryout, beyond which lies the PDO region. In this region, the vapor—particularly that near the wall—is rapidly heated and becomes superheated almost immediately. In the PDO region, the dispersed droplets are carried by the vapor flow and remain at the saturated temperature. This temperature difference between the two phases is referred to as thermal non-equilibrium. The presence of thermal non-equilibrium in the PDO region has been observed in several experimental studies done by Forslund and Rohsenow (1966), Nijhawan et al. (1980), Evans et al. (1983) et al. Due to the temperature difference, heat is transferred from the vapor to the droplets, particularly in the near-wall region where vapor superheating is greatest. Additionally, droplets can deposit on the wall and remove heat through direct evaporation.

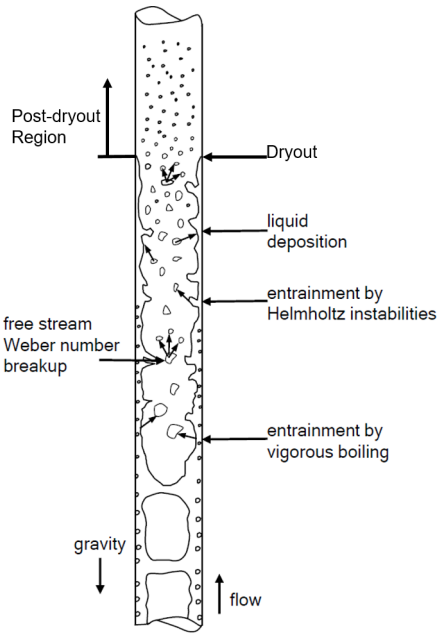

Figure 1.1: Flow pattern of two-phase flow inside tube

From Figure 1.2, the heat transfer mechanism in the PDO region can be decomposed as: forced convective heat transfer from the wall to the vapor $Q_{w\to v}$, interfacial heat transfer from the vapor to droplets $Q_{v\to d}$, direct contact heat transfer from wall to droplets $Q_{w\to d}$, and radiation heat exchange among wall, droplets, and vapor. Since the liquid droplets cannot wet the surface at high wall temperatures, the portion of heat transferred through the droplets-wall direct contact heat transfer is quite limited. The forced convection heat transfer between the wall and the vapor is considered as the primary mode of wall cooling. Most droplets are evaporated in the superheated vapor flow. The existence of droplets is not only important to the interfacial heat transfer but also affects the convection cooling efficiency. The presence and evaporation of liquid droplets changes the vapor velocity and temperature profile. Especially, when the droplets evaporate in the region near the wall, the thermal boundary layer of the vapor flow is altered, affecting the wall-vapor heat transfer efficiency. Thus, the convection heat transfer coefficient cannot be calculated directly using the correlation from single-phase flow heat transfer and needs modifications for dispersed flow. The efficiency of droplet evaporation affects the speed of vapor superheating and affects the convective heat transfer between wall and vapor. Understanding the droplet behaviors in the PDO region is important to understand the PDO heat transfer mechanism.

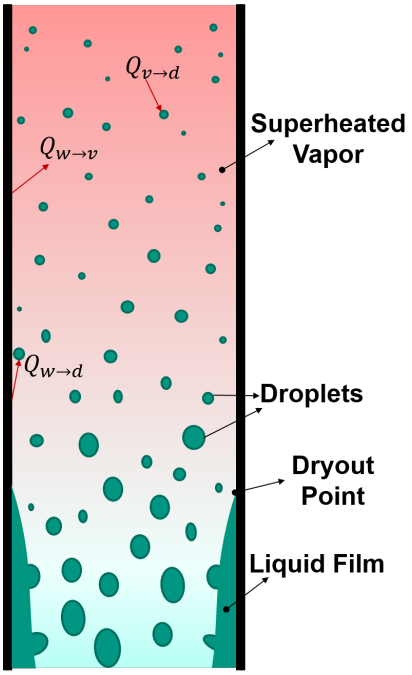

Figure 1.2: Schematic of dryout and post-dryout

1.2 Research Background

Since PDO heat transfer plays an important role in determining the maximum temperature of the thermal system, research on PDO heat transfer has been ongoing for more than 50 years. The research scope involves experimental and theoretical studies. Experimental studies conducted by previous researchers (Bennett et al., 1968; Becker et al., 1983; Era et al., 1966; Köckert et al., 2018) with different fluids cover a wider range of mass flux, heat flux, pressure, and tube size. Considering the growing importance of investigation and application of supercritical systems, more interest has been attracted to the heat transfer characteristics at very high pressure (Bishop et al., 1965; Swenson et al., 1962; Herkenrath et al., 1967; Nishikawa et al., 1983). From the analysis of the experimental data, several correlations for predicting the wall temperature and heat transfer coefficient have been developed by modifying the Dittus-Boelter correlation (Dittus and Boelter, 1930; Winterton, 1998). In these correlations (Liesch et al., 1975; Groeneveld and Moeck, 1969; Vojtek, 1978) the vapor temperature is taken as saturated temperature with the assumption that the vapor is not superheated until all the droplets are evaporated. However, with the improvement of the experimental technique, the vapor temperature in mist flow was measured. It was found that the vapor could be superheated even with the existence of a large amount of droplets (Parker and Grosh, 1961). The discovery of thermal non-equilibrium makes the assumption of saturated vapor temperature during PDO heat transfer prediction lack physical meaning. More research works then focus on how to describe and calculate the degree of thermal non-equilibrium. Some empirical or semi-empirical correlations based on parameters analysis and data fitting were developed to predict the actual vapor temperature or actual steam quality. For example, Chen et al. (1979) derived correlations for actual steam quality by analyzing the process of vapor-droplet interfacial heat transfer and data fitting. Yoder and Rohsenow (1983) built a first-order differential equation for the actual steam quality, with coefficients determined from experimental data. However, the accuracy of the empirical correlations is always

limited by the parameter range of the experimental data for regression analysis. To obtain a general model capable of elucidating heat transfer mechanisms and a wider application range, mechanistic models have been developed by modeling the individual heat transfer processes in the PDO region. The mechanism model takes dryout as the starting point and assumes dryout corresponds to a thermal equilibrium status (Yu, 2019; Guo and Mishima, 2002). The heat transferred between wall-vapor, vapor-droplet, and droplet-wall is calculated with correlations developed for single process. For example, the correlation used in the vapor-droplet heat transfer calculation is developed from the experiment of single droplet evaporation in superheated gas (Ranz et al., 1952; Lee and Ryley, 1968; Yuen and Chen, 1978). The heat transfer between the droplet and the wall usually uses correlations from single droplet evaporation on the heated wall and solid particle deposition rate in unheated gas (Liu and Ilori, 1974; Paleev and Filippovich, 1966). The droplet initial size and velocity are elementary for the initialization of the calculation procedure. The size was usually evaluated with correlations from annular flow (Tatterson et al., 1977; Kataoka et al., 1983; Lopes and Dukler, 1985) or the fitted correlation from limited experimental results (Ueda and Kim, 1982; Cumo et al., 1974). The velocity was evaluated at first by the homogeneous model (Forslund and Rohsenow, 1968; Hynek, 1969b) and later evaluated by the derived correlations(Yoder and Rohsenow, 1983; Plummer et al., 1974). Besides, the radiation heat transfer between wall, vapor, and droplet is ignored in several works (Forslund and Rohsenow, 1968; Moose and Ganić, 1982; Saha, 1980) while also included in the work of Guo and Mishima (2002) and Meholic (2011). The most popular radiation model is the network radiation model developed by Sun et al. (1976). After implementing the correlations of all the heat transfer processes, the first-order differential equations of the steam quality and droplet size are created according to the conservations of energy and momentum. Droplet velocity in PDO region is solved either from first-order differential equations based on force analysis (Varone, 1990; Plummer et al., 1974) or from slip-ratio correlations (Yu, 2019). Then the vapor temperature and wall temperature profile can be calculated step by step. The mechanistic models are mostly one-dimensional. The parameters with two-dimensional(2D) and three-dimensional(3D) distributions such as void fraction, droplet size, velocity, etc. are all calculated using surface averages. The complexity of droplet behavior makes one-dimensional mechanistic models unable to predict droplet-vapor heat transfer accurately. The influence of droplet evaporation on vapor convection in a one-dimensional model has also not been properly considered in previous work. To investigate the multi-dimensional characteristics of droplet behaviors and its effect on the vapor phase, computational fluid dynamics (CFD) has been used to simulate thermal-hydraulic behavior in the PDO region. There are two numerical approaches usually used in CFD models: the Euler-Euler method and the Euler-Lagrange method. Euler-Euler method builds continuity equations both for vapor and droplets (Lin et al., 1989; Li and Anglart, 2015) while the Euler-Lagrange method builds continuity equations for the vapor phase and builds the motion equation for the droplets (Keizo et al., 2005; Torfeh and Kouhikamali, 2015). In CFD models, it is necessary to solve the governing equations by discretizing the flow region into microelements, which requires far more computational resources than correlation-based or mechanistic models.

1.3 Objectives and Methodology of Research

Understanding heat transfer in the PDO region is essential for ensuring the thermal integrity of high-power-density heat exchange systems and maintaining nuclear reactor safety. Previous investigations of PDO heat transfer have employed experimental studies, predictive models, and computational fluid dynamics (CFD) approaches. Despite decades of research, accurately modeling PDO heat transfer remains challenging due to the complex

behavior of droplets and the limited availability of detailed interfacial heat transfer models. In particular, existing correlations for droplet size and velocity lack sufficient experimental validation, and experimental data on droplet parameters under PDO conditions remain scarce.

This research is therefore motivated by the following needs:

- To improve the mechanistic understanding of droplet dynamics—including lateral transport, deposition, and evaporation—under PDO conditions.
- To generate experimental data on droplet size and velocity in the PDO region for the validation and enhancement of submodels describing droplet behavior.
- To integrate CFD-based and experimental insights into a reliable, mechanistic PDO heat transfer model capable of predicting wall temperature across a range of thermal-hydraulic conditions.

To address these objectives, a combined numerical and experimental methodology is adopted, as illustrated in Figure 1.3:

- *CFD simulation of droplet behavior in the PDO region:* A discrete particle model (DPM) implemented in ANSYS Fluent is employed to simulate droplet dynamics in the PDO region. The radial distribution of droplet mass flux, evaporation rates, and deposition behavior are analyzed under various boundary conditions. The simulations enable visualization of droplet transport phenomena and allow quantification of the effects of evaporation on droplet deposition and entrainment. Additionally, the impact of droplet evaporation on the vapor temperature profile is investigated. These results contribute directly to the development of the improved PDO model.
- *Visual experimental investigation of droplet behavior:* High-speed visualization experiments are conducted through optical access windows to capture droplet motion under PDO conditions. Post-processing of the recorded images enables the extraction of key parameters, including droplet size, velocity, and spatial distribution. The experimental data are used to evaluate existing correlations for droplet size and velocity. The validated or newly developed correlations are then incorporated into the PDO heat transfer model.
- *Development of an improved PDO heat transfer model:* A physics-based mechanistic model is developed, incorporating enhanced interfacial heat transfer treatment and experimentally validated correlations for droplet size and velocity. This model aims to improve both the accuracy and the physical interpretability of wall temperature predictions under PDO conditions.

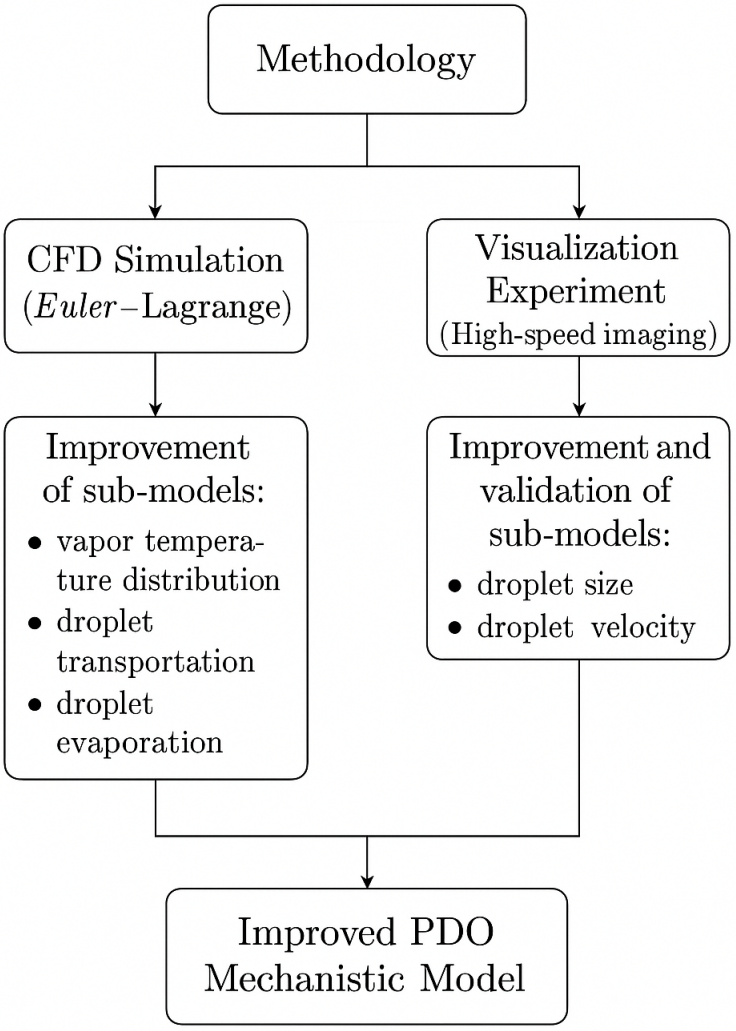

Figure 1.3: The structure of objective and methodology

2. Scientific and Technical Status

Previous investigations on PDO heat transfer can be roughly divided into experimental studies, prediction models, and numerical simulations. From the experimental work, the wall temperature is measured and found to continuously increase in the PDO region in some cases. However, a decreasing trend of wall temperature in the PDO region was also found under high mass flux conditions (Bennett et al., 1968). The experimental data have provided valuable insights into the heat transfer mechanisms in PDO regions. Through parameter analysis of the experiment data, the wall temperature trend is found to be related to fluid properties, fluid mass flux, wall heat flux, and operation pressure. To determine the relationship between wall temperature and these parameters, and thus to predict the peak temperature of the heating surface, numerous predictive models for PDO heat transfer have been developed. Among them, the correlative models assume that the PDO heat transfer is similar to the single-phase convection. The heat transfer coefficient is fitted with the obtained experimental data. Besides, the mechanistic model attempts to model the actual heat transfer paths that existed in the PDO region. Correlations developed for individual heat transfer paths are used. CFD simulations are also employed to simulate PDO heat transfer and obtain the three-dimensional distribution of thermodynamic parameters.

2.1 Experimental Work

Bennett et al. (1968) performed experiments in the PDO region using a tube with an inner diameter of 12.6 mm at a pressure of 7 MPa, corresponding to the typical operating pressure of a boiling water reactor (BWR). From the experiment, the wall temperature was measured and it showed a sharp increase at the onset of dryout. In the experimental work of Becker et al. (1983), dryout and PDO experiments were conducted in a 14.9 mm diameter tube with a 7 m heated length, utilizing water as the working fluid. Becker's experiments covered a wide range of pressures, with reduced pressure ranging from 0.1 to 0.99. The sharp increase in wall temperature under high pressure is less significant compared with the case under lower pressure. It is known that fluid properties change dramatically from subcritical to supercritical pressure conditions. Understanding heat transfer characteristics under very high pressure is important for the design and safety analysis of supercritical power systems, such as supercritical water reactors (Wu et al., 2022) and supercritical carbon dioxide system(Song, 2021). Bishop et al. (1965), Swenson et al. (1962), Herkenrath et al. (1967) conducted experiments with water under high pressure up to the reduced

pressure of 0.97. To reduce the difficulties of conducting experiments with water at very high pressures, experimental research on PDO heat transfer at high pressure was often performed using refrigerants(Nishikawa et al., 1983; Mawatari and Mori, 2016; Rensch et al., 2024), since refrigerants exhibit similar thermodynamic behavior during boiling as water but have relatively low latent heat and critical pressure.

In addition to measuring and analyzing wall temperature, some experiments conducted in the PDO region also focused on characterizing droplet parameters to better understand droplet behavior in dispersed flow regime. For instance, Kendall and Rohsenow (1978) carried out experiments to investigate the heat transfer between the wall and dispersed droplets in the PDO region. By maintaining the target wall at a specified temperature and recording the changes in heat input before and after droplet impact, the amount of heat transferred during wall-droplet interaction was quantified. The experimental observations revealed that at low wall superheat, droplets attached and evaporated on the wall surface, whereas at high superheat, droplets tended to rebound. Analysis of the processed data indicated that the heat transfer efficiency between droplets and the wall depended highly on the wall superheat. As shown in Figure 2.1, the heat transfer efficiency is high at low wall superheat but drops sharply beyond a critical superheat threshold, approaching nearly zero.

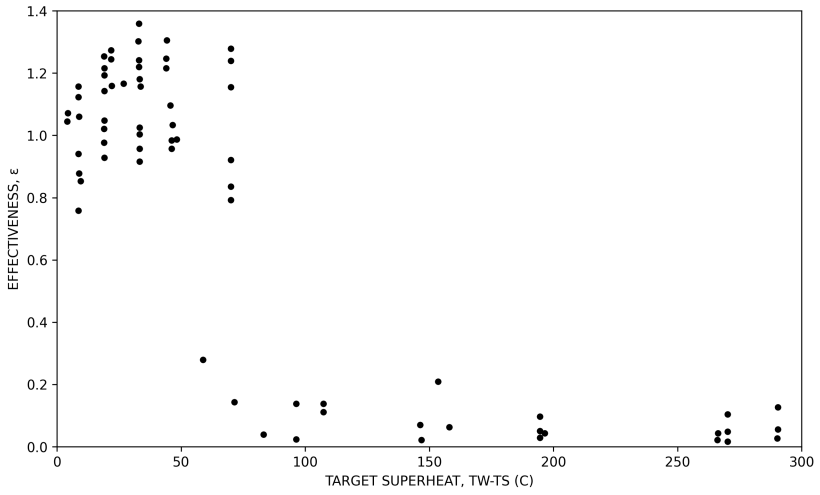

Figure 2.1: Drop heat transfer effectiveness in different wall superheat (Kendall and Rohsenow, 1978)

Cumo et al. (1974) conducted a photographic study on droplet behavior in the PDO region using Freon 12 as the working fluid. A visual test section was installed at the end of the heating tube. When subcooled Freon entered the inlet and was heated, dispersed flow was generated within the heating section by adjusting the supplied heat flux. Through the visual test section, droplet size and spatial distribution could be observed and recorded photographically. The experiment was performed at a vapor mass flux of approximately 900 kg/(m^2·s) and a pressure range of 0.3 to 1.0 MPa. Analysis of the extracted droplet parameters from the images revealed that, with increasing pressure, the droplet size distribution shifted toward smaller diameters. The observed distributions exhibited a Maxwellian shape and were fitted using a gamma distribution function.

Ueda and Kim (1982) conducted dryout experiments to determine the heat flux at which dryout occurred at the end of the test section. Freon 113 was used as the working fluid in a

uniformly heated, vertically upward flow tube. A glass plate coated with magnesium oxide was placed at the tube outlet. After adjusting the heating power to reach dryout at the end of the test section, droplets exiting the tube were collected on the coated glass plate. This experiment was carried out under mass fluxes ranging from 220 to 890 kg/(m^2·s) at a constant pressure of 0.3 MPa. By measuring the size of the craters formed by droplet impacts and converting these to actual droplet diameters, droplet size and distribution were obtained. The measured arithmetic mean diameter was found to decrease with increasing vapor velocity.

2.2 Prediction Model

In this section, theoretical investigations of PDO heat transfer are reviewed from two perspectives: empirical correlations and mechanistic models. Empirical correlations typically treat the entire PDO heat transfer as a convective process between the vapor and the wall. In contrast, mechanistic models aim to decompose the PDO heat transfer into several constituent mechanisms, including wall–vapor convective heat transfer, vapor–droplet interfacial heat transfer, wall–droplet contact heat transfer, and radiation heat transfer.

2.2.1 Empirical Correlations

From the convection heat transfer Equation (2.1), when the wall heat flux $q_w^{''}$ is known, the wall temperature T_w can be calculated after obtaining the heat transfer coefficient h_{wv} and vapor temperature T_v.

$$T_w = T_v + \frac{q_w^{''}}{h_{wv}} \tag{2.1}$$

Based on the treatment of vapor temperature, empirical correlations can be categorized into equilibrium and non-equilibrium correlations. In equilibrium correlations, the vapor is assumed to remain at the saturation temperature until the equilibrium steam quality x_e exceeds 1, and the primary objective is to determine the heat transfer coefficient. In non-equilibrium correlations, the vapor is superheated after the occurrence of dryout. Then the key task becomes the determination of the degree of vapor superheating.

2.2.1.1 Equilibrium Correlations

In equilibrium correlations, by assuming the vapor temperature is at the saturation temperature, the wall temperature can be predicted by obtaining the heat transfer coefficient h_{wv}. The well-known Dittus-Boelter correlation (Dittus and Boelter, 1930), which works well in pure vapor forced convection, is selected and modified to fit the two-phase flow heat transfer in the PDO region. Dougall (1963) substituted the homogeneous two-phase velocity into the Dittus–Boelter correlation and obtained the Dougall–Rohsenow correlation. Liesch et al. (1975) modified the Dougall-Rohsenow correlation by including a temperature ratio of wall and vapor temperature. A correction factor was introduced by Miropolskiy (1963) in Equation (2.6) and later incorporated into Groeneveld's correlations.

Dittus-Boelter correlation

$$h_{wv} = 0.023 \frac{k_v}{D_t} Re_v^{0.8} Pr_v^{0.4} \tag{2.2}$$

$$Re_v = \frac{G_v D_t}{\mu_v} \qquad Pr_v = \frac{c_{p,v}\mu_v}{k_v} \tag{2.3}$$

Dougall-Rohsenow correlation

$$h_{wv} = 0.023 \frac{k_v}{D_t} \left[\frac{\rho_v D_t}{\mu_v} \left(\frac{\dot{V}_l + \dot{V}_v}{A_T} \right) \right]^{0.8} Pr_v^{0.4} \tag{2.4}$$

Modified Dougall-Rohsenow correlation

$$h_{wv} = 0.023 \frac{k_v}{D_t} Pr_v^{0.4} \left[Re_v \left(x_e + (1 - x_e) \frac{\rho_v}{\rho_l} \right) \right]^{0.8} \left(\frac{T_v}{T_w} \right)^{0.5} \tag{2.5}$$

Miropolskiy Y factor

$$Y = 1 - 0.1 \left(\frac{\rho_l}{\rho_v} - 1 \right)^{0.4} (1 - x_e)^{0.4} \tag{2.6}$$

Groeneveld correlation

$$h_{wv} = 0.00327 \frac{k_v}{D_t} (Pr_{vw})^{1.32} \left[Re_v \left(x_e + (1 - x_e) \frac{\rho_v}{\rho_l} \right) \right]^{0.901} Y^{-1.5} \tag{2.7}$$

The term $Re_v \left(x_e + (1 - x_e) \rho_v / \rho_l \right)$ in Equation (2.7) represents the two-phase Reynolds number, Re_{TP}, which is correlated with the equilibrium steam quality and fluid densities. In the above correlations, parameters with the subscript v are evaluated at the bulk vapor temperature, which corresponds to the saturation temperature. Parameters with the subscript vw are evaluated at the wall temperature. Here, Pr_v and Re_v denote the Prandtl number and Reynolds number of the vapor phase, respectively. $\dot{V}_l$ and $\dot{V}_v$ represent the volumetric flow rates of the liquid and vapor phases. A_f and D_t are the inner flow area and inner diameter of the tube, respectively. $C_{p,v}$, ρ_v, k_v, and μ_v denote the specific heat, density, thermal conductivity, and dynamic viscosity of the vapor at the bulk temperature. ρ_l is the liquid density, typically evaluated at the saturation temperature T_s. G represents the mass flux. x_e is calculated by:

$$x_e = \frac{h - h'}{h_{lg}} \tag{2.8}$$

where h is the enthalpy at a defined position. h' is the enthalpy of liquid phase at saturation temperature. h_{lg} is the latent heat.

Correlations for predicting the heat transfer coefficient under very high pressure have also been developed based on high-pressure experimental databases. For example, Bishop et al. (1965) and Swenson et al. (1962) conducted experiments under high pressure and modified the constant variables in the Dittus-Boelter correlation with the experimental data. Recently, Song (2021) included several factors to account for variations in properties and dimensionless numbers. Based on regression analysis of a large set of high-pressure experimental data, Song's correlation considers mixture properties, the non-equilibrium factor, and the effect of wall temperature. The assessment of the correlation shows good agreement with a wide range of experimental data (Becker et al., 1983; Köckert et al., 2021).

Song correlation

$$h_{wv} = \frac{k_v Nu}{D_t} \tag{2.9}$$

$$Nu = F_1 \cdot F_2 \cdot F_3 \left(0.023 Re_{TP}^{0.8} Pr_w^{0.4} \right) \tag{2.10}$$

with,

$$F_1 = 8.346 \times 10^{-03} Re_{TP}^{0.319} \tag{2.11a}$$

$$F_2 = max \left(0.795 Pr_w^{-1.752}, 0.809 Pr_w^{1.287} \right) \tag{2.11b}$$

$$F_3 = min \left[0.715 \left(1 - x_e \right)^{-0.678}, 1.0 \right] \tag{2.11c}$$

In Song's correlation, the two-phase Reynolds number Re_{TP} is evaluated with viscosity and expressed as:

$$Re_{TP} = \frac{GD_t}{\mu_v}\left[x_e + \frac{\mu_v}{\mu_l}(1 - x_e)\right] \tag{2.12}$$

2.2.1.2 Non-equilibrium Correlations

In thermal non-equilibrium correlations, vapor superheating is assumed to exist throughout the entire PDO region. EEmpirical or semi-empirical correlations have been developed to predict the actual vapor temperature or steam quality. The non-equilibrium correlations focus on solving the actual vapor temperature T_{va} as well as the actual steam quality x_a.

Groeneveld and Delorme (1976) developed a non-equilibrium correlation that includes a calculation procedure to determine the actual steam quality, x_a. However, due to experimental limitations, x_a cannot be directly measured but inferred from experimental data. With the inferred x_a , the dimensionless parameters were analyzed and a correlation for the thermal non-equilibrium was fitted as:

$$\frac{h_{va} - h_l}{h_{lg}} = \exp[-\tan\Psi]\exp[-(3\alpha_{hom})^{-4}] \tag{2.13}$$

$$\Psi = a_1 Pr^{a_2}(Re_{hom})^{a_3}\left(\frac{q''_w D_t C_{p,ve}}{k_{ve}h_{lg}}\right)^{a_4}\sum_{i=0}^{i=2} b_i\,(x_e)^i \tag{2.14}$$

$$(\Psi < 0 \Rightarrow \Psi = 0; \qquad \Psi > \pi/2 \Rightarrow \Psi = \pi/2)$$

The subscript ve represents that the thermal properties are evaluated at equilibrium vapor temperature. The Re_{hom} and α_{hom} are the Reynold number and void fraction under homogeneous conditions:

$$Re_{hom} = \frac{GD_t x_a}{\mu_{ve}\alpha_{hom}} \qquad \alpha_{hom} = \frac{x_a}{x_a + \frac{\rho_v}{\rho_l}(1 - x_a)} \tag{2.15}$$

where

$$\begin{aligned} &a_1 = 0.13864, && a_2 = 0.2031, && \\ &a_3 = 0.20006, && a_4 = -0.09232, && \\ &b_0 = 1.3072, && b_1 = -1.0833, && b_2 = 0.8455. \end{aligned}$$

The x_a and T_{va} then can be known after obtaining h_{va} from Equation (2.13). The modified wall-vapor convective heat transfer correlation of Hadaller and Banerjee (1969) for two-phase flow performs best during the assessment, which is recommended for further analysis.

$$h_{wv} = 0.008348\frac{k_{vf}}{D_t}\left[\frac{GD_t}{\mu_{vf}}\left(x_a + (1 - x_a)\frac{\rho_v}{\rho_l}\right)\right]^{0.8774}(Pr_{vf})^{0.6112} \tag{2.16}$$

Here the subscript vf means the properties are evaluated with film vapor temperature T_{vf}, where

$$T_{vf} \simeq \frac{(T_w + T_b)}{2} \tag{2.17}$$

After assessing with 1852 data points, the root mean square (RMS) of predicted wall temperature is 6.9%. Compared with the Dougall-Rohsenow and equilibrium Groeneveld correlation, the prediction accuracy has been improved a lot. In the model of Groeneveld and Delorme (1976), the derived actual steam quality used for correlation fitting is evaluated by the empirical correlation which brings a large degree of empiricism.

In Chen et al. (1979)'s work, an analogy between momentum transfer and heat transfer was established. Based on this analogy, a wall–vapor heat transfer model was derived, allowing the actual steam quality to be inferred from experimental data:

$$h_{wv} = G_v C_{p,vf} Pr_{vf}^{-2/3} \frac{f_F}{2} \tag{2.18}$$

the G_v is the vapor mass flux, f_F is the friction factor which is evaluated by Beattie (1973)'s correlation. It is known that thermal non-equilibrium drives the heat transfer from vapor to droplets. This amount of heat determines the actual steam quality. Therefore, Chen analyzed the vapor–droplet heat transfer mechanism using the interfacial heat transfer correlation of Forslund and Rohsenow (1966) and obtained the ratio of actual to equilibrium steam quality through dimensional parameter analysis:

$$q_{vd} = \frac{3\pi}{2} (1-\alpha) \frac{{D_t}^2}{d} \frac{2k_v}{d} \left(1 + 0.276 {Re_d}^{0.5} {Pr_v}^{0.3}\right) (T_v - T_d) \tag{2.19}$$

$$\frac{x_a}{x_e} \simeq f_3 \left[\frac{T_v - T_d}{T_w - T_v}\right] \left[\frac{1 + 0.276 {Re_d}^{0.5} {Pr_v}^{0.3}}{f Re_v {Pr_v}^{1/3}}\right] \left[\frac{6(1-\alpha){D_t}^2}{d^2}\right] \tag{2.20}$$

d is droplet diameter. T_d is the droplet temperature, which is normally calculated with saturated temperature T_s. Re_d is the droplet Reynolds number and is defined as below,

$$Re_d = \frac{\rho_v (U_v - U_d) d}{\mu_v} \tag{2.21}$$

The three bracketed terms in Equation (2.20) indicate that the ratio x_a/x_e depends on the dimensionless temperature difference, the dimensionless heat transfer coefficient, and the dimensionless heat transfer area. Regression analysis of these three parameters against the inferred actual steam quality shows that x_a/x_e is proportional only to the dimensionless temperature difference, with the proportionality slope varying under different pressures.

$$\frac{x_a}{x_e} = 1 - B(P) T_d \tag{2.22}$$

$$B(P) = \frac{0.26}{1.15 - (P/P_c)^{0.65}} \tag{2.23}$$

P and P_c are the working pressure and the critical pressure. The correlation for $B(P)$ was obtained from regression analysis of water experiment data in the reduced pressure range of (0.01,0.89). Chen's model predicted the convection heat flux of 2854 data points with a 14.9% derivation. Several researchers have assessed this model with different experimental databases. It was found that the model exhibits a larger standard deviation when applied under very low mass flux conditions (Annunziato et al., 1983). Yu (2019) and Köckert et al. (2024) also assessed Chen's model and found it performs poorly with R-134a experimental data.

Köhler and Hein (1986) developed a correlation for vapor temperature by analyzing the interfacial heat transfer as Chen et al. (1979) did. Köhler derived a vapor superheated correlation based on the heat balance in the PDO flow region.

$$T_{v,max} = T_s + \frac{h_{lg}}{2C_{p,v}} \left[\sqrt{1 + \frac{4C_{p,v} q''_w}{h_{lg}(h_{vd} A_d)}} - 1\right] \tag{2.24}$$

The $T_{v,max}$ is the maximum vapor temperature that can be reached. h_{vd} is the heat transfer coefficient of vapor to the droplet. A_d is the heat transfer area. $(h_{vd} A_d)$ represents the amount of heat transferred from vapor to droplets. Correlations were fitted by:

For $G/La \leq 1767 \times 10^3$,

$$(h_{vd}A_d) = 1.473 \times 10^{-7} \left(G/La\right)^{1.33} \tag{2.25a}$$

and $G/La > 1767 \times 10^3$,

$$(h_{vd}A_d) = 3.078 \times 10^{-24} \left(G/La\right)^{4} \tag{2.25b}$$

$$La = \sqrt{\frac{\delta}{g\left(\rho_l - \rho_g\right)}} \tag{2.25c}$$

In Köhler and Hein (1986), the PDO region in a horizontal tube was divided into two subregions: a thermal equilibrium developing region and a thermal non-equilibrium developed region. The calculated maximum vapor superheat $T_{v,\max}$, as defined by Equation (2.24), was used as the boundary between these two regions. The corresponding steam quality at this split point, denoted as $x_{\min}$, was determined based on the value of $T_{v,\max}$. From the dryout point to $x_{\min}$, the actual vapor temperature T_{va} was assumed to increase linearly from the saturation temperature to $T_{v,\max}$, during which no droplet evaporation was considered to occur. In the developed region, the vapor temperature was assumed constant, and droplet evaporation proceeded until the steam quality reached a limiting value $x_{\lim}$. Beyond this point, the wall temperature was held constant until all droplets were fully evaporated.

The correlation of x_{lim} was fitted by water experimental data and found that it only related to the pressure change:

$$x_{lim} = 0.7 + 0.002 \cdot P \tag{2.26}$$

The correlation proposed by Köhler and Hein (1986) was subsequently improved by Kastounis (1987), who introduced a density ratio term to extend its applicability to working fluids such as nitrogen, water, and Freon-12. The improved correlation was later evaluated in Shah (2017) across a comprehensive set of experimental conditions. However, its performance was found to be unsatisfactory for the broader dataset. Based on the comparison results, Shah (2017) recommended the correlation developed by Shah and Siddiqui (2000) for predicting the actual steam quality, which demonstrated superior accuracy. This correlation incorporates two dimensionless parameters: the boiling number (Bo) and the Froude number (Fr).

$$Bo = \frac{q''_w}{Gh_{lg}} \qquad Fr_L = \frac{G^2}{{\rho_l}^2 g D_t} \tag{2.27}$$

For the cases with $Bo \geq 5 \times 10^{-4}$,

If $x_e \geq 0.4$:

$$x_a = \left(-0.0347 + 0.9335x_e - 0.2875{x_e}^2 + 0.035{x_e}^3\right) {Fr_L}^{0.064} \tag{2.28}$$

If $x_e < 0.4$, the value of x_a is obtained by linear interpolation between x_a at $x_e = 0.4$, calculated using Equation (2.28), and $x_{a,\text{int}}$ from Equation (2.29).

$$x_{a,int} = x_{e,int} = 0.19{Fr_L}^{0.16} \tag{2.29}$$

For the case with $Bo < 5 \times 10^{-4}$,

$$\left(x_e - x_a\right) = \left(x_e - x_a\right)_o \frac{Bo}{5 \times 10^{-4}} \tag{2.30}$$

where the $(x_e - x_a)_o$ is the value of $(x_e - x_a)$ when $Bo \geq 5 \times 10^{-4}$.

The above methods all use local parameters to substitute into explicit thermal non-equilibrium correlations. Yoder and Rohsenow (1983) proposed an implicit correlation for calculating the actual steam quality based on the droplet diameter gradient along the heating length.

$$\frac{dd}{dz} = -2\frac{h_{vd}(T_v - T_s)}{U_d \rho_d h_{lg}} \tag{2.31}$$

Assuming that the droplet number rate is constant and substituting the energy and mass conservation:

$$K\frac{x_a^{3/4} x_e}{(1-x_a)^{7/12}}\frac{\mathrm{d}x_a}{\mathrm{d}x_e} = x_e - x_a \tag{2.32}$$

with:

$$\begin{aligned} K = 0.58 \left(\frac{d_{do}}{D_*}\right)^{1.25} \frac{1}{(1-x_{do})^{5/12}} \left(\frac{\rho_d}{\rho_v}\frac{q''_w}{G h_{lg}}\right)^{0.75} \left(\frac{GD_*}{\mu_v}\right)^{0.5} \left(Pr_v^{2/3}\right) \\ \cdot \left[\frac{\rho_v}{\rho_d}\frac{1-x_{do}}{x_{do}} + \frac{1}{1+3.65\sqrt{\frac{\rho_d}{\rho_v}\frac{q''_w}{G h_{lg}}\frac{d_{do}}{D_*}\frac{1}{x_{do}}}}\right]^{0.5} \end{aligned} \tag{2.33}$$

D_* is heated equivalent diameter. ρ_d is the density of droplet and evaluated at the saturated temperature. The x_{do} and d_{do} are the steam quality and droplet diameter at the dryout point, which was calculated by the correlations from Yoder (1980). A Runge-Kutta solution scheme was used here to get the value of K and x_a. Yoder's model is a history-dependent and step-wise model. The correlation could successfully predict the wall temperature profile in the PDO region in different dryout steam quality and pressure cases from literature data (Bennett et al., 1968; Forslund and Rohsenow, 1966; Yoder and Rohsenow, 1983). However it did not get a good agreement when assessed with the Freon-12 data from Cumo et al. (1972), low-pressure water data from Nijhawan et al. (1980) and Freon data from Koizumi et al. (1979).

Similar as Yoder's model, Nishikawa et al. (1986) developed a first-order implicit equation to calculate the x_a for high pressure conditions.

$$\frac{\mathrm{d}x_a}{\mathrm{d}x_e} = \frac{1}{BoK_n}\left(\frac{x_e}{x_a} - 1\right) \tag{2.34}$$

where K_n represents the non-equilibrium degree obtained by the experimental data fitting:

$$K_n = 4260 \left(\frac{GD_t}{\mu_v}\right)^{0.52} \left(\frac{G^2 D_t}{\sigma \rho_v}\right)^{-0.73} Pr_v^{0.3} \left(\frac{\rho_v}{\rho_d}\right)^{0.3} x_a^n (1-x_a)^{-0.2} \left(\frac{x_e}{x_a} - 1\right)^{0.83} \tag{2.35}$$

$$n = 2.0 \exp\left[-1.3\left(\frac{G\mu_v}{\sigma\rho_v}\right)\left(\frac{\rho_d}{\rho_v} - 1\right)^{1.7}\right] - 1 \tag{2.36}$$

σ is the droplet surface tension. A correlation for convective heat transfer for superheated vapor is developed and modified based on the experimental data under high pressure.

$$h_{wv} = 0.0048\frac{k_v}{D_t}\left[\frac{GD_t}{\mu_v}\left(x_a + (1-x_a)\frac{\rho_v}{\rho_d}\right)\right]^{0.92} Pr_v^{0.4}\left[1 + \frac{2}{(z/D_t)^{1.1}}\right] \tag{2.37}$$

The prediction results of Nishikawa's model show good agreement with their Freon experimental data obtained at high pressure. The model also performs well when evaluated

against the Freon data from Groeneveld (1972) and Schnitter (1982), which were conducted at relatively low pressure. But the work of Köckert et al. (2024) showed that Nishikawa's model doesn't predict the heat transfer coefficient well in R-134a experimental data under low and middle pressures.

2.2.2 Mechanistic Model

The basic idea of the mechanistic model is to identify the individual heat transfer processes occurring in the PDO region and simulate each separately. Instead of applying a single correlation for the convective heat transfer coefficient, several submodels are employed to describe these distinct processes. As mentioned earlier, six heat transfer paths exist among the wall, vapor, and droplets. The two most critical processes are heat transfer from the wall to the vapor and from the superheated vapor to the droplets. The direct heat transfer path from the wall to the droplets is sometimes neglected, as the high wall temperature tends to prevent direct contact between the wall and the droplets. The heat transfer equations for the three processes can be expressed as:

$$q''_{wv} = h_{wv}\left(T_w - T_{va}\right) \tag{2.38}$$

$$q''_{vd} = h_{vd}\left(T_{va} - T_s\right) n_d \pi d^2 \frac{D_t}{4} \tag{2.39}$$

$$q''_{wd} = n_{dep} Q_{sd} \tag{2.40}$$

q''_{wv}, q''_{wd}, q''_{vd} are the heat transfer per unit wall area between wall-vapor, wall-droplet and vapor-droplet. h_{wv} is the heat transfer coefficient between wall and vapor in the mechanistic model. q''_{vd} is calculated with the interfacial heat transfer coefficient h_{vd} and droplet surface area $n_d \pi d^2$. n_d is droplet volume density. Through step-wise integration of q''_{vd} and q''_{wv}, the actual steam quality and vapor temperature can be obtained. Compared with applying a single thermal non-equilibrium correlation, the mechanistic model estimates the amount of droplet evaporation, thereby extending its applicability to a wider range of pressures and flow conditions. In the two-step model, the wall-droplets q''_{wd} is assumed to be zero. q''_{wv} equals to the wall total heat flux q''_w. For example, Bennett et al. (1968),Laverty and Rohsenow (1964), and Saha (1980) developed two-step models that neglected both droplet–wall contact heat transfer and radiation heat transfer. It was also suggested that in the short distance beyond dryout, the wall temperature is not extremely high, allowing partial droplet deposition to occur (Cheng et al., 2018). Therefore the q''_{wd} is included in three-step models (Forslund and Rohsenow, 1968). The Q_{sd} is the heat transferred from the wall to the single droplet during the collision. n_{dep} is the droplet number per area and second contacting with the heated wall.

$$q''_{wv} = q''_w - q''_{wd} \tag{2.41}$$

In both the two-step and three-step models, the calculation procedure starts from the dryout point, establishes gradient equations based on correlations for the individual processes, and solves them by stepwise integration. The gradient on droplet diameter is based on the assumption that the droplet size decreases while the droplet number keeps constant. Here is the calculation of gradient of key parameters:

Droplet diameter gradient

$$\frac{dd}{dz} = -\frac{2q''_{vd}}{h_{lg}\rho_d U_d} - \frac{4d\, q''_{wd}}{3(1-x_a)h_{lg}D_t G} \tag{2.42}$$

Actual steam quality and vapor temperature gradient

$$\frac{dx_a}{dz} = \frac{-3(1-x_{do})d^2}{{d_{do}}^3}\frac{dd}{dz} \tag{2.43}$$

$$\frac{dT_v}{dz} = \frac{h_{lg}\frac{dx_e}{dz} - [h_{lg} + C_{p,v}(T_{va} - T_s)]\frac{dx_a}{dz}}{x_a C_{p,v}} \tag{2.44}$$

Considering that the radiation heat transfer could be important in some cases, several researchers also included the radiation model in their models(Guo and Mishima, 2002; Meholic, 2011).

From the above overview, it is evident that in mechanistic models the convective heat transfer coefficient, interfacial heat transfer coefficient, wall–droplet heat transfer model, droplet size, and droplet velocity are the key parameters governing the model's applicability and predictive accuracy. Considerable efforts have been devoted to refining the correlations associated with these sub-processes. In the following section, the models and correlations adopted for these key parameters in previous mechanistic approaches are reviewed.

2.2.2.1 Heat Transfer Between Vapor and Droplet

The correlations of interfacial heat transfer coefficient h_{vd} used in the PDO heat transfer mechanistic model are mostly derived from the experiments of single droplet evaporation in superheated gas. Frossling (1938) conducted several experiments to investigate the evaporation of single stationary droplets in superheated gas. Experimental results revealed that the water droplet surface area reduction rate is proportional to the square root of Reynolds number. Ranz et al. (1952) developed a set of dimensionless partial differential equations to theoretically analysis the interfacial mass and heat transfer mechanism. Although a general solution is difficult to obtain, through dimensional analysis, the mass transfer Nusselt number is found to be related to the Reynolds number Re and Schmidt number Sc. Substituting the special boundary condition of $Re = 0$ into the governing equations, the natural evaporation Nusselt number of droplets in stationary gas as 2.0 can be obtained. Therefore, the basic format of interfacial mass transfer Nusselt number Nu_{im} can be written as:

$$Nu_{im} = 2.0 + K_1 Sc^m Re^n \tag{2.45}$$

Through the analogy of mass transfer and heat transfer, the interfacial heat transfer Nusselt number Nu_{ih} can be expressed as:

$$Nu_{ih} = 2.0 + K_2 Pr^p Re^q \tag{2.46}$$

Through fitting the Frossling experimental data (Frossling, 1938), it can be obtained that $p = 1/3$ and $q = 1/2$. Since the droplets are stationary in these experiments, the Re here actually is the relative Reynold number Re_d. With further experiments being conducted under the Re_d numbers range of 0 to 200 and air temperature up to 220℃, the value of K_2 was determined to be 0.6. The widely used Ranz correlation(Ranz et al., 1952) is written as:

$$Nu_{vd} = \frac{h_{vd}d}{k_v} = 2.0 + 0.6{Pr_v}^{0.33}{Re_d}^{0.5} \tag{2.47}$$

The form of Equation (2.45) is widely accepted as a fundamental model for droplet evaporation in gas flows. Most subsequent studies adopt this form as a basis for empirical fitting, aiming to improve predictive accuracy and extend the applicability of the K_2 parameter. For instance, Forslund and Rohsenow (1968) employed a value of $K_2 = 0.55$, based on the earlier work of Baumeister et al. (1965), while Saha (1980) reported a value of $K_2 = 0.459$.

Lee and Ryley (1968) conducted evaporation experiments on water droplets exposed to superheated steam. The droplets, with diameters ranging from 230 to 1130 μm, were suspended on glass fibers of 50 μm diameter, and their size reduction was measured optically. In Lee's experiments, the droplet Reynolds number (Re_d) ranged from 64 to 250,

the steam pressure varied from 1 to 2 bar, and the degree of superheat spanned from 2°C to 34°C. Based on the experimental data, the value of K_2 was fitted as 0.74. Owing to its development under water–steam conditions, Lee's correlation has been widely adopted in PDO mechanistic models (Guo and Mishima, 2002; Keizo et al., 2006; Meholic, 2011). However, since the correlation was derived from data with $Re_d < 250$, its applicability may be limited for higher Reynolds numbers.

To address this limitation, Hughmark (1967) incorporated data from Friend and Metzner (1958) and Griffith (1960), and developed a set of correlations applicable to various ranges of Re_d and Pr.

If $Re_d < 450$ and $0 \leq Pr_v < 250$,

$$Nu = 2 + 0.6 Re_d^{0.5} Pr_v^{0.33} \tag{2.48a}$$

If $Re_d < 450$ and $Pr_v > 250$,

$$Nu = 2 + 0.4 Re_d^{0.5} Pr_v^{0.42} \tag{2.48b}$$

If $450 < Re_d < 10000$ and $Pr_v < 250$,

$$Nu = 2 + 0.4 Re_d^{0.5} Pr_v^{0.42} \tag{2.48c}$$

If $450 < Re_d < 10000$ and $Pr_v > 250$,

$$Nu = 2 + 0.175 Re_d^{0.62} Pr_v^{0.42} \tag{2.48d}$$

Experimental investigations and theoretical analyses of droplet and vapor heat transfer mechanisms have revealed that, during droplet evaporation in superheated vapor, the newly generated vapor accumulates near the droplet surface, thickening the local boundary layer. This phenomenon influences both the local flow field and the vapor concentration in the interfacial region. The vapor produced by droplet evaporation is initially at saturation temperature, which is lower than that of the surrounding superheated vapor. Consequently, this saturated vapor must absorb heat to reach thermal equilibrium with its environment, thereby modifying the vapor temperature distribution and thermophysical properties near the droplet interface. To characterize the reduction in heat and mass transfer caused by this effect, a dimensionless parameter B, known as the blowing correction factor or mass transfer number, is introduced. The influence of B has been incorporated into several empirical correlations, including those proposed by Yuen and Chen (1978) and Downingm (1966).

$$B = \frac{C_{p,v}(T_v - T_d)}{h_{lg}} \tag{2.49}$$

Yuen and Chen (1978) conducted experiment in higher Re_d number to 2000 and high gas temperature. The Ranz correlation (Ranz et al., 1952) was selected as the basic format and fitted the blowing factor with the experimental data:

$$Nu_f\,(1 + B) = 2 + 0.6 Re_d^{0.5} Pr_v^{0.33} \tag{2.50}$$

In addition to the blowing effect, radiation heat transfer may also significantly influence droplet evaporation under high-temperature conditions. To account for this, the blowing factor B is often modified to include the contribution of radiation.

In the work of Renksizbulut and Yuen (1983), the form of B was improved to account the effect of radiation heat transfer in high temperature environment:

$$B_f = \frac{C_{p,v}(T_v - T_d)}{h_{lg}} \left(1 + \frac{q_r}{q_c}\right) \tag{2.51}$$

where the q_r and q_c are the heat transfer due to radiation and convection. In the work of Kim and Ban (2000), the blowing factor B_f was also used and Schmidt number Sc was inserted to Yuen's correlation(Yuen and Chen, 1978) to include the effect of coupling effect of mass transfer and energy transfer. After fitting the experimental data of Renksizbulut and Yuen (1983) and Lee and Ryley (1968) et al, the exponent value of Sc and the constant were determined:

$$Nu_f \left(1 + B_f\right)^{0.7} = 2.0 + 0.53 {Sc_f}^{-0.2} {Pr_v}^{0.33} {Re_d}^{0.5} \tag{2.52}$$

Besides introducing the blowing factor, Kuznetsov et al. (2020) conducted experiments under high gas temperature and larger Re_d range. A temperature ratio was included in their correlation:

$$Nu_f = 2.0 + 0.6 {Pr_v}^{0.33} {Re_d}^{0.5} \left(1 - T_s/T_a\right)^{-T_s/T_b} \tag{2.53}$$

2.2.2.2 Heat Transfer Between Wall and Vapor

The calculation of wall-to-vapor convective heat transfer often employs the same empirical correlations as those introduced in the correlative studies presented in section 2.2.1. For example, Saha (1980) employed the correlation from Heineman (1960), which was developed for superheated steam-wall convection. Cheng et al. (2018) substituted two-phase mixture properties into the Dittus-Boelter correlation(Dittus and Boelter, 1930). The mixture temperature is evaluated by:

$$T_{TP} = \alpha T_v + (1 - \alpha) T_s \tag{2.54}$$

There are also some modified Dittus-Boelter correlations for two-phase flow accounting entrance effect and property variations effect. For example, the Forslund and Rohsenow (1966)'s correlation was developed based on nitrogen experimental data. Yu (2019) included the factor of viscosity ratio to improve the Forslund correlation to work also for water and R134 fluids.

Forslund
$$h_{wv,fdev} = 0.035 \frac{k_{vb}}{D_t} Re_{vb}^{0.743} Pr_{vb}^{0.4} \tag{2.55a}$$

Yu
$$h_{wv,fdev} = 0.03675 \frac{k_{vb}}{D_t} Re_{vb}^{0.743} Pr_{vb}^{0.4} \left(\frac{\mu_{vb}}{\mu_{vw}}\right)^{0.1} \tag{2.55b}$$

Besides, the existence of droplets in the PDO region brings further differences to the convection heat transfer. Therefore, Varone (1990) developed a correlation for convective heat transfer between wall and vapor to account for the effects of the droplet evaporation, the fluid property variations over the tube cross-section, and the entrance length effect from Sozer et al. (1984):

$$Nu_{wv} = \phi_h Nu_{wv,0} \tag{2.56}$$

$$Nu_{wv,0} = 0.0168 Re_{vw}^{0.841} Pr_{vw}^{0.4} \tag{2.57}$$

$$\phi_h = \phi_p \phi_t \phi_e \left(\frac{{\rho_v}^*}{\rho_{vb}}\right)^m \tag{2.58}$$

where the vapor properties with subscript vw are evaluated at wall temperature. The correlations for ϕ_p, ϕ_t, and ϕ_e were eventually empirically correlated. The ${\rho_v}^*$ is the vapor density in the property correction factor.

2.2.2.3 Heat Transfer Between Wall and Droplet

The heat transfer between the wall and droplets in the PDO region is typically calculated using Equation (2.40), where the product of the droplet deposition rate and the heat transferred by a single droplet. Based on the contact heat transfer coefficient for a single droplet on flat plates developed by Baumeister et al. (1965), Forslund and Rohsenow (1968) proposed a corresponding correlation in their mechanistic model for PDO heat transfer. A constant value of 0.2 is given as the correction factor. This simplification was later refined by Bajorek and Young (2000), who replaced the constant with empirical correlations expressed as functions of the Reynolds number.

According to the experimental investigations conducted by Kendall and Rohsenow (1978), the wall-droplet heat transfer efficiency is relatively high at low wall superheat, but decreases sharply once a certain threshold is exceeded as shown in Figure 2.1. This behavior led to the classification of wall-droplet interactions into two regimes: *wet impact* and *dry impact*. Wet impact occurs at low wall superheat, where droplets are able to spread and evaporate upon contact, facilitating effective heat transfer. In contrast, dry impact dominates at high wall superheat, where droplets are unable to wet the surface and are instead rebounded into the flow. Since wall temperatures in the PDO region typically fall within the dry impact regime, the associated heat transfer is often minimal. Consequently, some models neglect this mechanism altogether, while others attempt to capture the physics of dry impact more accurately.

Kendall and Rohsenow (1978) modeled dry impact by representing droplets as truncated spheres and right circular cylinders:

$$q''_{wd} = (1-\alpha)\,\rho_d u^*_D h_{lg} \epsilon \tag{2.59}$$

$$\varepsilon = 2.6 \left(\frac{\rho_v}{\rho_d}\right)^{\frac{1}{2}} \left(\frac{\bar{R}}{d}\right)^{\frac{1}{8}} \left[\frac{\beta_2 k_v (T_w - T_s)}{h_{lg}(\rho_v \sigma d)^{\frac{1}{2}}}\right]^{\frac{1}{2}} \left[1.5 \frac{\mu_v h_{lg}}{\beta_2 k_v (T_w - T_s) + 0.225}\right]^{-\frac{1}{4}} \tag{2.60}$$

u^*_D is the dimensionless droplet deposition rate. β_2 is a coefficient accounting for the effect of superheat on the vapor temperature profile. $\bar{R}$ is average droplet extension radius. This model led to a predictive model for heat transfer effectiveness that showed good agreement with experimental results. Kendall's dry impact model was also implemented in the PDO model of Varone (1990), Yoder (1980) and Yu (2019).

Guo and Mishima (2002) modeled the dry collision process between droplets and walls and derived a simpler droplet contact model. This model was adopted by Meholic (2011) and Keizo et al. (2006) into their mechanistic models.

$$q''_{wd} = (T_w - T_s) \left[\frac{18 {k_v}^3 {t_R}^3 \rho_v h_{lg} \dot{m}^5_D}{d^5 {\rho_d}^4 \mu_v (1-\alpha)\,(T_w - T_s)}\right]^{1/4} \tag{2.61}$$

where t_R is the contact time and calculated with $t_R = \pi\sqrt{\rho_d d^3/(16\sigma)}$. $\dot{m}^5_D$ is the droplet deposition mass flux.

Iloeje et al. (1989) developed models separately of dry and wet impact processes. The dry impact process is considered not touching the wall but transferring heat from droplets with the vapor in the thermal boundary layer.

Different from the above situation where wet and dry impacts are discussed separately, Cheng et al. (2018) considered the contact heat transfer efficiency (the ratio of the heat transfer between the droplet and the wall to its own latent heat) as a complementary error function with the superheat of the wall:

$$q''_{wd} = h_{lg} \cdot \dot{m}_D \cdot f_{EV} \tag{2.62}$$

$$f_{EV} = 1 - \frac{1}{2}\left[1 + erf\left(\frac{T_w - T_{LF}}{0.1 \cdot \sqrt{2} \cdot (T_{LF} - T_s)}\right)\right] \tag{2.63}$$

The T_{LF} is the Leidenfrost temperature (taken as 100°C superheating here). 10% of the superheat degree is used as the standard deviation. When the wall temperature T_w far exceeds the T_{LF}, the heat transfer efficiency between the droplet and the wall is 0. When the wall temperature gradually decreases, the heat transfer efficiency gradually increases until the T_w is lower than the T_{LF}, the droplets are considered to be able to wet the wall and completely evaporate on the wall when they impact on the wall.

2.2.2.4 Models for Droplet Parameters

(A) Droplet Size and Distribution Model

In the mechanistic model, the droplet size at the dryout point should be known as part of the initial calculation procedure. For one-dimensional mechanistic models or for simplifying calculations, the average droplet size is often employed. Various mean diameters, such as volume mean diameter d_{vm}, sauter mean diameter d_{32}, and arithmetic mean diameter d_{10} are commonly used based on different calculation methods. In the actual conditions, the droplets are not in one uniform size but have a size distribution at the dryout point. Therefore, the study of droplet size is usually conducted together with the study of droplet distribution. Previous investigations into droplet size models in dispersed flow can be broadly categorized into two groups: One group involves correlating droplet size and distribution based on experimental data. The other group posits that droplets are generated in the period of annular flow, suggesting that size models developed for annular flow may be applicable to the dryout point.

Cumo et al. (1974) conducted a photographic experiment with Freon 12 as the working fluid. The experimental data of droplet size and distribution were obtained from the visual test section. The experiment data extracting from the images showed that the average droplet size is smaller at high pressure conditions. The correlations for droplet size distribution and most probable diameter are fitted as:

$$n\,(d) = \frac{d}{{d_*}^2} e^{-d/d_*} \tag{2.64}$$

The d_* here is the most probable diameter, which is correlated as:

$$d_* = 123.1 \frac{\mu_d}{G x_e} (1 - \pi)^{0.31} \tag{2.65}$$

With known droplet distribution, the linear mean diameter d_{10} was postulated with the most probable diameter: $d_{10} = 2d_*$. The value of x_e is larger than 1 in most cases showed in Cumo's work, which means that the observing points mostly fallen in the PDO region. But the distance between the observing point and the dryout point is unknown from experimental data.

Ueda and Kim (1982) conducted dryout experiments and got the droplet size and distribution at the dryout point. From the experiment data it was found that the droplet size is smaller in higher vapor velocity. After combined with data obtained by air-water system(Ueda, 1979), the mean droplet size is fitted as:

$$\frac{d_{10}}{D_t} = 6.1 \times 10^{-3} \left[\frac{\sigma}{\mu_g U_v} \times \left(\frac{\rho_v}{\rho_d}\right)^{1.25}\right]^{0.5} \tag{2.66}$$

U_v is the vapor axial velocity. The gamma distribution was also found well fitted the measured droplet size distribution:

$$\frac{\Delta n}{N} = 42.7 \left(\frac{d}{d_{10}}\right)^3 exp\left(-4\frac{d}{d_{10}}\right) \frac{\Delta d}{d_{10}} \tag{2.67}$$

The Δn is the number of droplets having size between $(d - \Delta d/2)$ and $(d + \Delta d/2)$. N is the total number of droplets obtained in current conditions, which equals to 600. The experiments is conducted with a mass flux range from 218 to 887 kg/(m^2·s). Ueda and Kim (1982) compared the current results with those from previous adiabatic annular flow experiments and found that the mean droplet diameter showed no significant difference between adiabatic and heated boundary conditions. These data were also utilized by Schnitter (1982), who included 30 experimental data points from the literature and developed a correlation for the mean droplet diameter:

$$\frac{d_{10}}{D_t} = 683.5 \cdot \frac{\mu_g}{U_g}\rho_g \cdot (\frac{\sigma}{U_g\,\rho_d})^{0.4} \cdot (\frac{1 - x_{do}}{x_{do}})^{0.25} \cdot (\frac{\rho_d}{\rho_g})^{0.325}(\frac{\mu_g}{\mu_d})^{0.1} \tag{2.68}$$

It is worth noting that in PDO heat transfer models, after substituting the droplet size at the dryout point, the droplet size within the PDO region is iteratively updated based on the heat transfer rate. For simplicity, most models assume that the total number of droplets remains constant, with only their size varying. In contrast, Schnitter's model accounted for droplet splitting and introduced an empirical correlation for the change in droplet number, employing a critical Weber number We_{cr}.

However, due to the scarcity of experimental data on droplet sizes in dispersed flow, these models were developed using very limited datasets without mechanistic justification, which constrains their applicability and accuracy. Consequently, substantial research has been directed toward understanding the mechanisms governing droplet size evolution from annular flow.

Some studies suggest that once droplets are entrained into the vapor core, the shear stress between the droplets and the vapor increases with vapor acceleration. When the droplet Weber number exceeds We_{cr}, droplets undergo breakup into smaller fragments, implying that droplet size cannot grow beyond a certain limit under given flow conditions. Based on the free-stream Weber number for droplet breakup, We_{cr} is employed to determine the maximum stable droplet size:

$$We_{cr} = \frac{\rho_v(U_v - U_d)^2 d_{max}}{\sigma} \tag{2.69}$$

d_{max} is the maximum droplet size in the vapor flow. Groeneveld (1972) took the value of 6.5 as the We_{cr}. In the PDO region, if the droplet weber number gets larger than the We_{cr}, the droplet will break-up. The new droplet size after break up is assumed as same as the critical droplet size. Forslund and Rohsenow (1966) calculated the droplet size at the dryout point with We_{cr} equal to 7.5. The droplet break-up was also included in their model. It was assumed that the droplet size after a break-up would be $1/3\sqrt{2}$ times of the initial size as the setting in Hynek (1969b)'s model.

Besides the free-stream Weber number, several researchers have suggested that droplet size is primarily determined by the generation process. Tatterson et al. (1977) considered the Kelvin–Helmholtz instability as the primary mechanism governing droplet formation. When high-velocity vapor flows over the agitated surface of a low-velocity liquid film, the pressure at the wave crest is lower than that in the trough. The pressure difference acts as the suction force on the crest and torn the crest. The surface tension of the torn crest resists the suction force until the pressure difference becomes large enough to detach part of the liquid from the crest. The detached liquid is then entrained into the main flow in the form of droplets. Based on this mechanism, Tatterson performed force balance analysis on the wave crest and derived the droplet size model for annular flow:

$$\frac{d_{10}}{D_t} = 2.4 \times 10^{-3}(\frac{2\sigma}{\rho_g {U_g}^2 f_s D_t})^{1/2} \tag{2.70}$$

The upper limit log-normal distribution was selected by Tatterson as the droplet distribution according to the work of Lopes and Dukler (1985) and Evans et al. (1983). Tatterson's size correlation was implemented in the mechanistic model of Mastanaiah and Ganic (1981).

In the work of Kataoka et al. (1983), the type of roll wave shearing off was considered as the main droplet entrainment and sizing mechanism. The force balance equation between the interfacial drag force and surface tension force was established. Factors then were correlated with experimental data. A correlation for volume mean diameter was developed as:

$$d_{vm} = 0.028 \frac{\sigma}{\rho_g {U_g}^2} {Re_d}^{-1/6} {Re_g}^{2/3} (\frac{\rho_g}{\rho_d})^{-1/3} (\frac{\mu_g}{\mu_d})^{2/3} \tag{2.71}$$

Kataoka's correlation was used in the model of Guo and Mishima (2002).

Yoder (1980) considered both the droplet formation mechanism and sizing during the development history. Several droplet sizing sequences prior to the dryout point were analyzed. Tatterson's correlation(Tatterson et al., 1977) was selected to represent the sizing process based on the Helmholtz instability mechanism. A value of 0.65 was chosen for We_{cr} to represent both film-slip droplet formation and Weber-number-induced breakup. By combining the three droplet sizing mechanisms, the droplet size at the dryout point can be determined from the cumulative mass distribution spanning from the droplet generation position to the dryout point.

$$\frac{d_c}{D_t} = \frac{\rho_v \sigma}{G^2 D_t} \frac{We_c}{(S_{do}-1)^2 \left(\frac{\rho_v}{\rho_d} + \left(\frac{1}{S_{do}} - \frac{\rho_v}{\rho_d}\right) x_{do}\right)^2} \tag{2.72}$$

$$S_{do} = \frac{1 + \sqrt{1 - \left(1 - \frac{4}{3}\frac{\rho_d \rho_v g \left(1-\frac{\rho_v}{\rho_d}\right)}{G^2 C_D} d_c \left(\frac{\alpha_{do}}{x_{do}}\right)^2\right)\left(1 - \frac{16}{3}\frac{q''_w}{G i_{v-d} C_D}\frac{d_c}{D_T}\frac{\rho_v}{\rho_d}\frac{1}{x_{do}}\right)}}{1 - \frac{4}{3}\frac{\rho_d \rho_v g \left(1-\frac{\rho_v}{\rho_d}\right)}{G^2 C_D} d_c \left(\frac{\alpha_{do}}{x_{do}}\right)^2} \tag{2.73}$$

$$\frac{d_{do}}{D_t} = \frac{1}{x_{do} - 0.1}\left(\frac{d_c}{D_t}(x_A - 0.1) + \left(\frac{\rho_d}{\rho_v}\right)^2 \frac{We_c}{(S_{lf}-1)^2}\frac{\rho_v \sigma}{G^2 D_T}\frac{1}{(\frac{\rho_d}{\rho_v}\frac{1}{S_{lf}} - 1)} \cdot \left[\frac{1}{1 + x_A(\frac{\rho_d}{\rho_v}\frac{1}{S_{lf}} - 1)} - \frac{1}{1 + x_{do}(\frac{\rho_d}{\rho_v}\frac{1}{S_{lf}} - 1)}\right]\right) \tag{2.74}$$

where

$$x_A = \frac{\left[\frac{S_{do}-1}{S_{lf}-1}\right]\left[\frac{\rho_v}{\rho_{lf}} + \left(\frac{1}{S_{do}} - \frac{\rho_v}{\rho_{lf}}\right) x_{do}\right] - \frac{\rho_v}{\rho_{lf}}}{\frac{1}{S_{lf}} - \frac{\rho_v}{\rho_{lf}}} \tag{2.75}$$

$$S_{lf} \equiv \frac{U_v}{U_{lf}} = \left(\frac{\rho_{lf}}{\rho_v}\right)^{0.205} \left(\frac{G D_T}{\mu_{lf}}\right)^{-0.016} \tag{2.76}$$

where the x_{do}, S_{do} and d_{do} are steam quality, slip ratio and droplet size at dryout point. The slip ratio S_{lf} is calculated by Ahmad (1970). Yoder's model was implemented in the PDO model of Yu (2019) and Varone (1990).

Droplet Velocity Model

The droplet velocity is the key parameter to calculate the void fraction α and droplet Reynolds number Re_d. At first, the flow at the dryout point was assumed a homogeneous flow. For example, Forslund and Rohsenow (1968), Hynek (1969b), and Moose and Ganić (1982) assumed at the dryout point the droplet velocity has the same velocity as the vapor, which means the slip ratio equals to 1.0. Mastanaiah and Ganic (1981) selected the slip ratio at dryout point S_{do} as 1.1 for the initialization of droplet velocity. Then the void fraction can be calculated with:

$$\alpha = \frac{1}{\frac{1-x}{x}\frac{\rho_g}{\rho_d}S + 1} \tag{2.77}$$

The droplet velocity downstream of dryout is not considered homogeneous and is usually calculated by the force balance acting on the droplet. The drag force and gravity force are the most popular forces considered in the literature. Taking Hynek's calculation method of increment of droplet velocity as an example(Hynek, 1969a):

$$\frac{dU_d}{dz} = \frac{3C_D\rho_g(U_v - U_d)^2}{4d\rho_d U_d} - (1 - \frac{\rho_v}{\rho_d})\frac{g}{U_d} \tag{2.78}$$

Since simply take S_{do} as 1.0 or 1.1 lack scientific meanings, Groeneveld (1972) adopted the slip ratio correlation (Ahmad, 1970) for annular flow and took the average value between this correlation and the 1.0 from the homogeneous model, which is shown to give the best results when applied in the PDO heat transfer model:

$$S_{do} = 1 + \frac{1}{2}\left[(\frac{\rho_d}{\rho_g})^{0.205} \cdot (\frac{GD_t}{\mu})^{-0.016} - 1\right] \tag{2.79}$$

Plummer et al. (1974) used Groeneveld's dryout slip ratio correlation and derived slip ratio correlation for downstream of dryout through analogy with equilibrium quality:

$$(\frac{1-S}{1-S_{do}}) = \left[1 - \frac{k(x_e - x_{do})}{1 - x_{do}}\right]^{A/k^B} \tag{2.80a}$$

$$k = C_1 log_e\left[G\sqrt{\frac{D_t}{\rho_g\sigma}}(1 - x_{do})^5\right] + C_2 \tag{2.80b}$$

The C_1 and C_2 are obtained through regression analysis. This slip ratio correlation was used for the droplet velocity calculation in the downstream flow in Ganic (1976)'s dispersed flow heat transfer model.

Yoder (1980) derived a new slip ratio correlation in the PDO region by integral droplet velocity gradient equation Equation(2.78) and rewritten as:

$$S = 1 + 2.31\left[\frac{\rho_d}{\rho_g}\frac{1}{x_a}\frac{q''_w}{Gh_{lg}C_D}\frac{d}{D_t}\right]^{1/2} \tag{2.81}$$

Saha (1980) used a droplet drift velocity V_{ij} to calculate the relative velocity and void fraction:

$$V_{ij} \approx -1.41\left[\frac{g\sigma(\rho_d - \rho_g)}{{\rho_g}^2}\right]^{0.25} \tag{2.82a}$$

$$(1 - \alpha) = \frac{1 - x_a}{1 + \frac{x_a(\rho_d - \rho_g)}{\rho_g} + \frac{\rho_d V_{ij}}{G}} \tag{2.82b}$$

Droplet Deposition Model

When the droplets are dispersed in the turbulent flow, they have a tendency to deposit on the wall due to the effect of vapor fluctuating velocity. From the Equation (2.40), the n_{dep} is calculated as:

$$n_{dep} = \frac{\dot{m}_{dep}}{\rho_d \frac{\pi d^3}{6}} \tag{2.83}$$

$$\dot{m}_{dep} = k_d C \tag{2.84}$$

where $\dot{m}_{dep}$ is droplet deposition mass flux and k_d is droplet deposition velocity. C is droplet concentration. The correlations used for droplet deposition in previous PDO models were normally developed from solid particle in gas flow. From the summary of McCoy and Hanratty (1977), it can be found that smaller particles deposit under the action of brownian force while the deposition of larger particles is a turbulence-controlled process. McCoy summarized the experimental data and proposed correlation of particle deposition rate with dimensionless particle relaxation time τ^+, which is calculated by:

$$\tau^+ = \frac{d^2 \rho_g \rho_p u^{*2}}{18 \mu_g^2} \tag{2.85}$$

where the ρ_p and d are the particle density and diameter. u^* is the dimensionless gas velocity. When the value τ^+ is small, the particle deposition rate is correlated by the Schmidt number Sh, which represents the molecular diffusion process. As the value of τ^+ increases, the deposition rate is proportional to the τ^{+2}. At approximately τ^+>22.9, the deposition rate seems to keep constant or slightly decrease as the increase of τ^+.

Theoretical investigations have aimed to analyze the mechanisms of particle transport and to develop a general model for predicting particle deposition, rather than relying solely on empirical data fitting. Friedlander and Johnstone (1957) identified the inertial effect of particles in turbulent eddies as the dominant transport mechanism. Experimental data indicated that the deposition rate is linearly proportional to the Reynolds number. Consequently, Friedlander assumed that mass transport is analogous to momentum transport in turbulent flow. Accordingly, a mass transport equation was established by analogy with momentum transfer in turbulent flow:

$$\tau_s = (\mu + \rho \epsilon_g) \frac{dU}{dy} \tag{2.86}$$

$$N = (D_v + \epsilon_g) \frac{dC}{dy} \tag{2.87}$$

C is the particle concentration. y is the radial distance to the wall. By neglecting the item of molecular diffusivity D_v and assuming that the eddy diffusivities of particles ϵ_p and gas ϵ_g are the same, the particle deposition rate k_d could be obtained:

$$\begin{aligned}
&For\, S^+ < 5: && \frac{k_d}{u^*} = \frac{f_s/2}{1 + \sqrt{f_s/2(\frac{1525}{S^{+2}} - 50.6)}} \\
&For\, 5 < S^+ < 30: && \frac{k_d}{u^*} = \frac{f_s/2}{1 + \sqrt{f_s/2}[5ln(\frac{5.04}{S^+/5 - 0.959}) - 13.73]} \\
&For\, S^+ > 30: && \frac{k_d}{u^*} = \sqrt{f_s/2}
\end{aligned} \tag{2.88}$$

where S^+ is the reduced stopping distance that a particle with a given initial velocity can travel through stagnant gas, as defined by Friedlander and Johnstone (1957).

Similar work have been conducted by Ganić and Mastanaiah (1981), Issapour and Lee (1990), and Yang and Lee (1991). These studies aimed to solve the diffusion Equation (2.87), with a key difference being that they applied eddy diffusivity correlations for the turbulent core rather than for the sublayer. To account for the lag between large particles and fluctuations in the gas phase, Ganić and Mastanaiah (1981) introduced a correction factor based on the ratio of particle eddy diffusivity to gas-phase eddy diffusivity. In contrast, Yang and Lee (1991) proposed a correction based on the ratio of droplet velocity to transverse vapor velocity. The correlation from Yang and Lee (1991) is provided below as an example:

$$\frac{k_d}{u^*} = \frac{1.224\,\eta_b}{1.33 + 2.44\,\eta_b\,ln\left[\frac{1+2(1-30/Re\sqrt{f_s/2})^2}{1-(1-30/Re\sqrt{f_s/2})^2}\right]} \tag{2.89}$$

η_b is the ratio of droplet velocity to fluid fluctuation velocity.

In addition to employing the analogy between mass and momentum transfer, Sugawara (1990) developed a droplet deposition correlation based on the analogy between mass and heat transfer. The mass transfer Schmidt number (Sc) and the heat transfer Nusselt number (Nu) were used to establish this analogy, and a correlation was subsequently fitted:

$$\frac{k_d}{U_g} = f(C){Re_g}^{-0.2}Sc^{-2/3} \tag{2.90}$$

$$f(C) = 9.0 \times 10^{-3}(\frac{C}{\rho_g})^{-0.5} \tag{2.91}$$

2.2.2.5 Radiation Model

In most cases, the heat transferred via radiation accounts for only a small fraction of the total heat transfer in the PDO region. Plummer et al. (1974), Forslund and Rohsenow (1968), Iloeje et al. (1989), Shah (2017), Moose and Ganić (1982), Yoder and Rohsenow (1983), and Varone (1990) all completely neglected the contribution of radiation heat transfer. However, radiation can become significant when the wall temperature is sufficiently high. Accordingly, Ganic (1976) considered radiation heat exchange between the wall and droplets. Later, Ganić and Rohsenow (1977) extended this analysis by including radiation heat exchange between the high-temperature wall and both the steam and liquid droplets, while still neglecting radiation between the superheated steam and droplets. The radiation heat flux is calculated as:

$$q''_{rad} = F_{wd}\sigma_b({T_w}^4 - {T_s}^4) + F_{wv}\sigma_b({T_w}^4 - {T_{v,s}}^4) \tag{2.92}$$

Here, F_{wd} and F_{wv} are the graybody factors, evaluated using the geometry factor and the method proposed by Sun et al. (1976). Guo and Mishima (2002) and Meholic (2011) also implemented Sun's network radiation model in their mechanistic models, including all radiation transfer paths. This network radiation model describes radiation heat transfer between the wall, vapor, and droplets in a manner analogous to an electrical network with three nodes, where thermal resistance corresponds to electrical resistance. σ_b denotes the Stefan–Boltzmann constant. Radiation heat exchange between the vapor and droplets (vd) is also considered, and the corresponding graybody factors F_{wd}, F_{wv}, and F_{vd} are calculated as:

$$F_{ij} = \frac{1}{R_i + R_j + \frac{R_i R_j}{R_k}} \tag{2.93}$$

$$
\begin{aligned}
R_v &= (1-\varepsilon_v)/[\varepsilon_v(1-\varepsilon_v\varepsilon_d)] \\
R_d &= (1-\varepsilon_d)/[\varepsilon_d(1-\varepsilon_v\varepsilon_d)] \\
R_w &= 1/(1-\varepsilon_v\varepsilon_d) + (1-\varepsilon_w)/\varepsilon_w
\end{aligned} \tag{2.94}
$$

where the $\varepsilon_{i,j,k}$ is the body emissivity.
There is another radiation model called two-flux model, which is proposed by Chan and Grolmes (1975) and used in Andreani and Yadigaroglu (1997)'s model. Meholic (2011) reviewed and compared the two-flux model with the Sun's network model. It was found that the Sun's network model is more suitable for modeling the radiation heat transfer in dispersed flow.

2.3 Numerical Approach

Parameters such as droplet size, droplet velocity, and void fraction exhibit complex multi-dimensional distributions that are difficult to capture in one-dimensional models. With advances in computational science, numerical approaches have increasingly been employed to simulate PDO heat transfer. By numerically solving two-dimensional or three-dimensional governing equations, the trajectories of droplets and their interactions with the wall and vapor flow can be simulated in detail, providing a more comprehensive understanding of the underlying physical processes.

It should be noted that in numerical models, the heat transfer coefficients between droplets and vapor, as well as the collision models between droplets and the wall, still rely on empirical correlations, similar to those used in mechanistic models. Typically, these models assume that heat from the wall is first transferred to the adjacent vapor layer via conduction and subsequently transported through the vapor core by convection. In some simplified numerical models, heat transfer between the wall and vapor, along with turbulent transport, is treated using empirical or semi-empirical correlations.

For example, Lin et al. (1989) developed a two-dimensional model by solving the continuity, momentum, and energy equations for both vapor and droplet phases in the PDO region. Mass, momentum, and heat exchanges between the phases are incorporated into the source terms of the differential equations. The wall-to-droplet heat transfer rate, q''_{wd}, is calculated using the correlations of Kendall and Rohsenow (1978), while the heat transfer between vapor and droplets is computed using the correlation of Yuen and Chen (1978). In addition, radiation heat transfer and wall-droplet contact mechanisms are also considered. At the wall boundary, the heat flux is distributed as:

$$
(k_g + k_r)\frac{\partial T_g}{\partial r} + q''_{wd} = q''_w \tag{2.95}
$$

r is the radial distance to the centerline of the tube. k_g is the gas thermal conductivity. k_r is the equivalent thermal conductivity of thermal radiation.

The turbulent thermal conductivity k_{tur} is used for the radial distribution of vapor temperature, which is calculated with turbulent Prandtl number Pr_{tur} and eddy viscosity are calculated with the μ_t from Malhotra and Kang (1984):

$$
\begin{aligned}
k_{tur} &= C_{pv}\frac{\mu_t}{Pr_{tur}} \\
Pr_{tur} &= \frac{1}{0.91 + 0.13{Pr_v}^{0.545}}
\end{aligned} \tag{2.96}
$$

Lin et al. (1989) used zero-function turbulence model of Cebeci and Bradshaw (1984) to express the μ_t :

$$
\mu_t = \rho_v \left\{ l\left[1 - exp(-\frac{y}{A})\right]\right\}^2 \cdot \left|\frac{\partial u_v}{\partial r}\right| \tag{2.97a}
$$

$$A = 26 \left(\frac{\mu_v}{\rho_v}\right) \left(\frac{\tau_w}{\rho_w}\right)^{1/2} \tag{2.97b}$$

$$l = R \cdot \left[0.14 - 0.08(1 - \frac{y}{R})^2 - 0.06(1 - \frac{y}{R})^4\right] \tag{2.97c}$$

R is the radius of the tube, which equals to $D_t/2$. τ_w is the wall shear stress. l is the mixing length. The calculation results were assessed with Bennett et al. (1968)'s experiment data and agreed well.

From the review of Lin et al. (1989), CFD simulations involve solving sets of discrete governing equations that cannot be feasibly calculated manually and thus require computer-based solutions. Self-programmed CFD models, such as those developed by Lin et al. (1989) and Andreani and Yadigaroglu (1989), allow greater flexibility but require substantial development time and expertise, often accompanied by additional simplifications—for example, simplified turbulence models in Lin et al. (1989). Due to these challenges, commercial CFD software has become increasingly popular because of its user-friendliness and comprehensive built-in functionalities (Li and Anglart, 2015; Torfeh and Kouhikamali, 2015). Software such as ANSYS Fluent offers multiple sub-models but allows only limited modifications. Incorporating extra forces on droplets or modeling droplet breakup can significantly increase computational costs. Recently, open-source CFD platforms like OpenFOAM have been adopted for PDO heat transfer predictions due to their flexibility. For instance, Anglart et al. (2018) extended the twoPhaseEulerFoam solver in OpenFOAM to implement Lagrangian particle tracking (LPT), enabling simultaneous tracking of droplet trajectories and bidirectional coupling with the vapor phase.

From the method dealing with the droplet phase, the approaches used for the PDO heat transfer simulation can be divided into the Euler–Euler approach and the Euler–Lagrangian approach. The aforementioned model by Lin et al. (1989), in which the droplet phase is treated as a continuous field with its own set of conservation equations, is an example of the Euler–Euler method. The method used in Andreani and Yadigaroglu (1989) for PDO heat transfer is the Euler-Lagrangian approach, which treats the vapor phase as a continuous medium solved on an Eulerian grid while droplets are tracked individually in Lagrangian coordinates by solving their equations of motion. The change of droplet mass, temperature, and velocity is collected as the source term to account for the heat, momentum, and mass exchange between phases.

In the following subsections, previous numerical studies are reviewed and categorized according to these two modeling frameworks.

2.3.1 Euler–Euler Approach

Zhong et al. (2019) selected the mixture two-phase model in ANSYS Fluent to study the flow and heat transfer characteristics of mist flow in a wire-wrapped rod bundle. A phase change model of liquid droplets is carried out through the coupling of a user-defined function (UDF) to ANSYS Fluent. The Discrete Ordinates (DO) Radiation Model is also included in their simulation. The results showed the temperature and velocity distribution of horizontal cross-sections.

The Euler–Euler approach can not only simulate PDO heat transfer but also predict the wall boiling and dryout occurrence. For example, Lin et al. (2022) conducted a 2D numerical simulation by coupling the Eulerian model with the wall boiling model to investigate the critical heat flux (CHF) and post-CHF in the vertical pipe. Similarly, Li and Anglart (2016) built an integrated model based on a three-field description of droplets, gas, and liquid film for annular flow, which incorporates both the pre- and PDO regions. Shi et al. (2016a) and Shi et al. (2016b) introduced a 3D Eulerian two-phase model and predicted

the occurrence of dryout and temperature profile in the post-dryout region in a straight-pipe once-through steam generator. Besides the prediction of CHF, their results found the existence of superheated steam in the PDO region, resulting in a deviation from the thermodynamic equilibrium between the vapor and liquid. It was found that the thermal non-equilibrium effect dominates in the whole PDO region and does not disappear until all droplets are evaporated. In the simulation work of Shi et al. (2016b), the Yuen and Chen (1978) correlation is selected for calculating vapor-droplet heat transfer. The droplet size change due to evaporation uses the model of Yao and Morel (2004). The standard turbulent k-ϵ model was used for both the vapor and droplet phases.

2.3.2 Euler–Lagrangian Approach

Compared with the Eulerian method, the Lagrangian method is more suitable for tracking droplet trajectories in dispersed flow.

Andreani and Yadigaroglu (1989) developed a 2D Eulerian and 3D Lagrangian model for simulating the heat transfer and droplet trajectories in dispersed flow. The vapor phase was simulated using a 2D Eulerian mesh, while the droplets were tracked in 3D Lagrangian coordinates. In this self-coded model, various forces acting on the droplets and droplet dynamics could be more easily incorporated. Andreani and Yadigaroglu (1989) considered drag force, lift force, thrust force, and turbulent force. Aerodynamic breakup and wall-impact breakup were also included. The correlation of Beard and Pruppacher (1971) was used to calculate the interfacial heat transfer coefficient.

Compared with the Euler–Euler method, the Lagrangian method in commercial software achieves better convergence and higher computational efficiency. The droplet trajectories and distributions are also clearer and easier to obtain. Kumari et al. (2010) studied air–water droplet mist flow inside a square heat sink using the DPM method in ANSYS Fluent. The discrete phase was simulated using the Lagrangian approach, coupled with the continuous phase through interaction terms in the transport equations. The droplet–air heat transfer was calculated using the correlation of Ranz et al. (1952). Their simulations showed significantly higher heat transfer coefficients in mist flows compared to those in air flows, indicating the potential of mist flow for enhanced thermal management applications.

Torfeh and Kouhikamali (2015) investigated thermal non-equilibrium in mist flow in a vertical tube using ANSYS Fluent. The simulation included drag force, virtual mass force, lift force, and thermophoretic force. They performed separate simulations assuming complete thermal equilibrium and complete thermal non-equilibrium. By analyzing the wall temperature and heat transfer coefficients, they found that under total thermodynamic equilibrium, the heat transfer rate to entrained droplets was too fast, which did not reflect the actual situation, thus proving the existence of thermal non-equilibrium. In the total thermal non-equilibrium case, the droplets were almost ignored, and the vapor temperature downstream of the dryout point was calculated based on the assumption that all added heat went into superheating the vapor. The results showed that the heat transfer rate from the vapor phase to entrained droplets was too slow. The simulation also revealed that PDO heat transfer tended toward total thermal non-equilibrium at low vapor velocities or with larger droplet sizes.

Anglart et al. (2018) developed a mechanistic CFD model in OpenFOAM to predict PDO heat transfer in annular flow. In the PDO region, the vapor phase was solved using a RANS-based Eulerian approach, while droplets were tracked individually through a Lagrangian particle tracking method with two-way coupling. The total wall heat flux was partitioned into vapor convection, wall-droplet direct contact, and thermal radiation. In addition to gravity, the droplets are considered to move under drag force and lift force. Simulation results showed good agreement with experiments in terms of wall temperature

rise and dryout location. While the contribution of wall-droplet and radiation heat transfer was generally small (<2% and 3–4%, respectively), their inclusion improved accuracy, particularly under low heat flux conditions. The model was also applied to a BWR subchannel, successfully capturing asymmetric dry patch formation, highlighting the benefit of CFD for three-dimensional PDO heat transfer analysis.

2.4 Summary

In this chapter, previous PDO heat transfer experiments, prediction models, and numerical simulations have been thoroughly reviewed. The experiments on PDO have a limited amount of data on droplet parameters, such as droplet size, distribution, and velocity, which are still lacking experimental investigation.

Equilibrium correlative models assume the vapor is at saturated temperature and focus on determining the wall-vapor heat transfer coefficient under PDO conditions. In contrast, thermal non-equilibrium correlations aim to solve the actual vapor temperature and then apply superheated vapor convection correlations. These correlations are often limited by the range of their underlying databases, prompting extensive research into developing reliable models to predict the physical processes accurately.

Mechanistic models use sub-models to simulate individual processes in PDO heat transfer, potentially including up to six heat transfer paths. Some studies ignored wall-droplet contact heat transfer and radiation due to their relatively small contributions to the total heat transfer. The two primary heat transfer processes—wall to vapor and vapor to droplets—are considered the most critical. Specifically, vapor-to-droplet interfacial heat transfer is crucial for determining thermal non-equilibrium. During interfacial heat transfer, droplet concentration and size distribution greatly influence the heat transfer rate. A review of existing droplet size and velocity models reveals a persistent lack of valid models for predicting droplet size and velocity at the dryout point.

With advancements in computer science, several CFD models and commercial software can now simulate PDO heat transfer in 2D or 3D. These simulations can accurately depict droplet distribution and behaviors such as droplet deposition and break-up. Nevertheless, CFD simulations require significant computational resources and time, and they also depend on the accuracy of correlation selection for initial droplet conditions, droplet-wall contact models, and single-droplet interfacial heat transfer coefficients.

3. CFD Simulation on Droplet Behaviors in PDO region

In the PDO region, liquid is entrained in the vapor flow as discrete droplets. Heat is transferred from the wall to the vapor, leading to an increase in vapor superheating. The droplets entrained in the vapor flow absorb heat from the superheated vapor, which slows down the process of vapor superheating and thus affects the wall temperature in the PDO region. The droplets also tend to move toward the wall, deposit on it, and transfer heat directly from the wall, further contributing to droplet evaporation and wall cooling. Therefore, in the PDO region, droplets play a significant role in slowing down the increase in wall temperature. Accurate prediction of droplet parameters is crucial for the predictive capability of PDO mechanistic models. Parameters such as droplet size, distribution, and velocity are essential for calculating interfacial convective heat transfer. Moreover, droplet deposition behavior is important when calculating wall-droplet heat transfer, which requires the droplet deposition velocity to account for the droplet deposition flux. However, the empirical correlations used to determine these droplet parameters are typically derived from studies on air-droplet flow or annular flow over unheated surfaces (Meholic, 2011; Iloeje et al., 1989). Research on droplet parameters in dispersed flow over heated surfaces, particularly considering droplet evaporation, remains very limited. Experimentally, studying the dynamic characteristics of evaporating droplets is especially challenging. Nevertheless, CFD provides a valuable tool for gaining a deeper understanding of droplet behavior in the PDO region.

This chapter explores droplet behaviors in the PDO region using CFD techniques, beginning with an introduction to the Discrete Phase Model (DPM method) in ANSYS Fluent, which is employed in the current simulations. The DPM method not only tracks the dynamic behaviors of droplets effectively but also exhibits good convergence and fast computational performance when tracking a large number of droplets. This method is validated in this chapter using experimental data from the literature. After method validation, a test section for simulating droplet behaviors in the PDO region is built, and boundary conditions are specified based on Becker's water experiments (Becker et al., 1983). The calculation results present the vapor temperature profile and droplet behaviors in the PDO region separately. Vapor temperature profiles under three pressures, three droplet sizes, and two mass fluxes are displayed and analyzed. The behaviors of droplets—including dynamics, evaporation, and deposition—are thoroughly examined under the reference conditions. Droplet dynamic behaviors, including size, spatial distribution, and velocity profiles,

are presented. Evaporation behaviors are visualized through contour plots and quantitatively analyzed via the radial distributions of evaporation rate density. Detailed analysis of droplet deposition includes single-droplet trajectories, as well as the statistical distribution and average radial velocity of droplets. Moreover, to quantitatively capture the effect of droplet size and evaporation on lateral movement, three new parameters representing overall movement behavior—droplet deposition mass flux, droplet deposition velocity, and droplet entrainment velocity—are introduced and derived from the CFD results. Additional simulations are conducted with an inactive droplet evaporation model to assess the impact of droplet evaporation on droplet deposition and entrainment.

3.1 Model Description

The present simulation is conducted using ANSYS Fluent 2021, which offers a comprehensive range of multiphase modeling approaches. Among them, the DPM is employed to investigate droplet behavior in the PDO region. In this method, the continuous vapor phase is solved on an Eulerian mesh, while droplets are tracked individually in Lagrangian coordinates. As droplets pass through vapor control volumes, they exchange momentum, mass, and energy with the surrounding vapor. This approach enables detailed tracking of droplet trajectories and facilitates the extraction of key droplet parameters such as size and velocity. A notable advantage of the DPM is that the computational mesh can be relatively coarse compared to the droplet size, since the droplets are tracked separately. In addition, only the conservation equations for the continuous phase and the droplet motion equations need to be solved, with interfacial interactions represented through source terms. Consequently, the DPM offers significantly higher computational efficiency compared to other multiphase methods, such as the Volume of Fluid (VOF) and Eulerian–Eulerian approaches.

However, the DPM assumes negligible droplet–droplet interactions and does not account for the physical volume occupied by droplets within the mesh, making it suitable only for dilute dispersed flows. In the present study, cases with the vapor volume fraction is above 90% are selected, justifying the assumption of negligible droplet interactions. Therefore, the application of the DPM in this simulation is both appropriate and advantageous.

Considering its efficiency, numerical robustness, and applicability to high steam quality conditions, the DPM is selected for the three-dimensional simulation of heat transfer in the PDO flow region. During the simulation, the vapor flow is treated as the continuous phase and is solved on Eulerian meshes. The k-ϵ turbulence model is used to calculate turbulence parameters of the vapor flow. Enhanced wall treatment (ANSYS Fluent) is applied to introduce a two-layer near-wall model, allowing more accurate prediction of vapor flow and droplet behavior near the wall. Vapor properties, such as density and heat capacity, are specified as functions of temperature and pressure.

3.1.1 Discrete Phase Model

In the present simulation, the unsteady particle treatment based on DPM is employed (ANSYS Fluent). Droplets are tracked in Lagrangian coordinates and are subject to gravitational and drag forces. The droplet and vapor phases are two-way coupled: superheated vapor transfers heat to the droplets, and the droplets absorb heat and evaporate into the vapor. This heat exchange modifies the vapor temperature profile, and the resulting increase in vapor quantity subsequently affects the flow velocity. The change in droplet momentum also serves as a momentum source in the continuous phase.

The droplet trajectory in Lagrangian coordinates is controlled by :

$$m_d \frac{d\vec{u}_d}{dt} = m_d \frac{\vec{u}_v - \vec{u}_d}{\tau_r} + m_d \frac{\vec{g}(\rho_d - \rho_v)}{\rho_d} + \vec{F} \tag{3.1}$$

where m_d is the droplet mass, $\vec{u}_d$ is the droplet velocity, $\vec{u}_v$ is the vapor velocity. $\vec{F}$ is the additional force, which is not considered in this simulation. The first item on the right-hand side is the drag force, and the τ_r is the droplet relaxation time. It is calculated by:

$$\tau_r = \frac{\rho_d d^2}{18\mu_v} \frac{24}{C_D Re_d} \tag{3.2}$$

The Re_d is calculated with:

$$Re_d = \frac{\rho_v d \left|\vec{u}_v - \vec{u}_d\right|}{\mu_v} \tag{3.3}$$

Where d is the droplet diameter. C_D is the drag coefficient, calculated with the spherical drag law:

$$C_D = a_1 + \frac{a_2}{Re_d} + \frac{a_3}{Re_d^2} \tag{3.4}$$

The a_1, a_2, a_3 are constants given by Morsi and Alexander (1972).

The dispersion of particles due to turbulence in the continuous phase is predicted using the stochastic tracking model. In this model, the vapor transient velocity in Equation (3.1) is calculated by Equations (3.5) and (3.6) to include the effect of instantaneous turbulent velocity fluctuations on the particle trajectories. Taking the velocity component in u direction as an example:

$$u_v = \bar{u} + u^{'} \tag{3.5a}$$

$$u^{'} = \zeta \sqrt{\bar{u^{'2}}} \tag{3.5b}$$

Where $u^{'}$ is the vapor fluctuation velocity. ζ is a normally distributed random number. $\sqrt{\bar{u^{'2}}}$ is the RMS of velocity fluctuation, which is considered isotropic and determined by the turbulent kinetic energy:

$$\sqrt{\bar{u^{'2}}} = \sqrt{\bar{v^{'2}}} = \sqrt{\bar{w^{'2}}} = \sqrt{2k/3} \tag{3.6}$$

with known the droplet velocity, the droplet trajectory is predicted by:

$$\frac{dx}{dt} = u_d \tag{3.7}$$

The new position of the droplet x^{n+1} is computed by a trapezoidal discretization of old position x^n and droplet velocity at old position u_d^n and new position u_d^{n+1}:

$$x_d^{n+1} = x_d^n + \frac{1}{2}\Delta t(u_d^n + u_d^{n+1}) \tag{3.8}$$

3.1.2 Interfacial Energy, Mass and Momentum Exchange

As the trajectory of a droplet is computed, the heat, mass, and momentum gained or lost by the droplet stream are calculated. These quantities are then incorporated into subsequent calculations for the continuous phase. Thus, the effect of the droplet trajectories on the vapor flow is also included. This two-way coupling is achieved by alternately solving the discrete and continuous phase equations until the solutions for both phases converge. Figure 3.1 shows the interactions between phases when one droplet passes an Eulerian mesh. After the exchange of mass, energy, and momentum, the parameters of droplets, like velocity, size, and trajectory as well as the parameters of vapor will change.

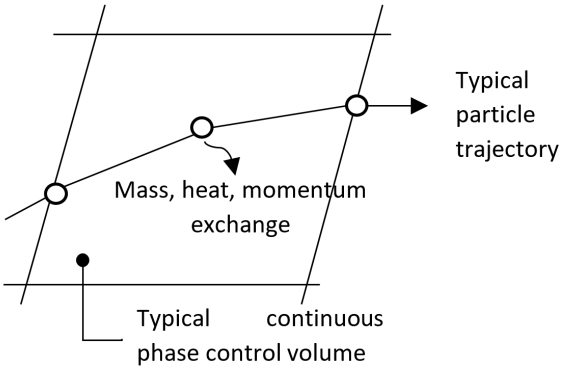

Figure 3.1: Schematic of interfacial interaction (ANSYS Fluent)

3.1.2.1 Interfacial Momentum, Heat and Mass Exchange

When the droplets pass through the control volume of the vapor phase, the droplets can be accelerated or decelerated under the effect of drag force between phases. During this process, there is momentum transfer between the continuous phase and the discrete phase. The CFD model examines the change in momentum of every droplet and sums all the momentum change to the momentum source of the momentum equation of the continuous phase. The heat transfer between droplet and vapor in ANSYS Fluent (2021) is calculated by:

$$Nu_{vd} = \left(2 + 0.6Re_d^{1/2}Pr^{1/3}\right) ln\left[1 + \frac{c_{pv}(T_v - T_d)}{h_{lg}}\right] \tag{3.9}$$

The mass and heat transfer from the droplets to the vapor phase are calculated by counting the mass and energy change of all the droplets as they pass through one control volume. The calculated mass and heat exchange is represented as the source term in the continuity and energy equation of the continuous phase.

3.1.3 Droplet Wall Interaction Model

When a droplet moves to the boundary cell, it has a possibility to impinge on the wall. During the impingement, the droplet deforms into a cylinder (ANSYS Fluent) and remains in direct contact with the heated wall for a short period of time (contact time) before rebounding. During this time, heat is exchanged between the droplet and the wall. After heat and momentum are transferred, the droplets are reflected back to the flow. The heat transfer from the wall to the droplet is calculated as following equations in ANSYS Fluent:

$$m_d c_{p,d} T_d = \int_0^{t_d} \frac{k_l A_{\text{cont}}}{H_{wd}} (T_w - T_d)\, dt \tag{3.10}$$

Where the k_l is droplet thermal conductivity. H_{wd} is the distance between deformed droplet center to the heated wall. The A_{cont} in this equation is the base area of the deformed droplet and is calculated by:

$$A_{cont} = \pi D_{max}^2/8 \tag{3.11a}$$

$$D_{max} = 0.61 D_0 We^{0.38} \tag{3.11b}$$

where the D_0 is the droplet size before the impaction. The contact time t_d between droplet and wall is calculated by (Akao et al., 1980; Birkhold, 2007):

$$t_d = 0.4 * \frac{\pi}{4}\sqrt{\frac{\rho_d D_0^3}{\sigma}} \tag{3.12}$$

3.2 Model Validation

The experimental work of Guo and Leung (2005) is selected for model validation. They conducted an air/droplet mixing two-phase flow experimental work in a test facility which has a length of 177.8 mm and a diameter in 22.2 mm. The experiment was conducted with Reynolds number of air flow ranging from 10,000 to 35,000, wall superheat up to 300°C, and droplet mass fraction ranging from 1 to 6 percent, which is quite similar to the PDO conditions. Experiments with both pure air injection and air-droplet mixture injection were performed to study the effect of droplets on the wall temperature profile. During the experiment, the wall temperature is measured. In present simulation, the geometry was built according to the experiment test section. The mesh sensitivity studies were carried out and the results are displayed in Figure 3.2. The mesh structure with 0.52 million meshes was finalized. Based on the simulation of single-phase cases, the k-ϵ turbulence model is selected among several turbulent models available in ANSYS Fluent. Figure 3.3 shows simulation results with the selected mesh structure and k-ϵ turbulence model under various heat fluxes. The simulated wall temperature of single-phase in three different wall heat fluxes shows a good agreement with the experimental measured wall temperature.

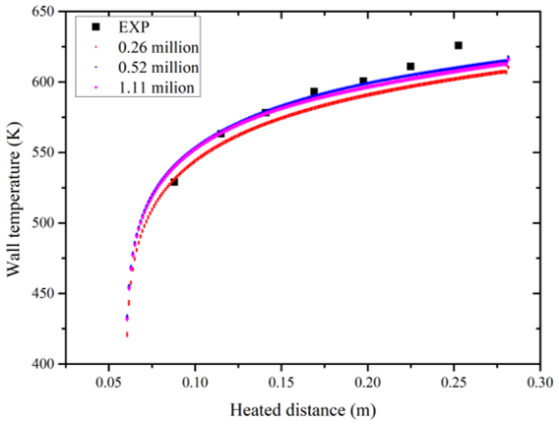

Figure 3.2: Mesh sensitivity analysis

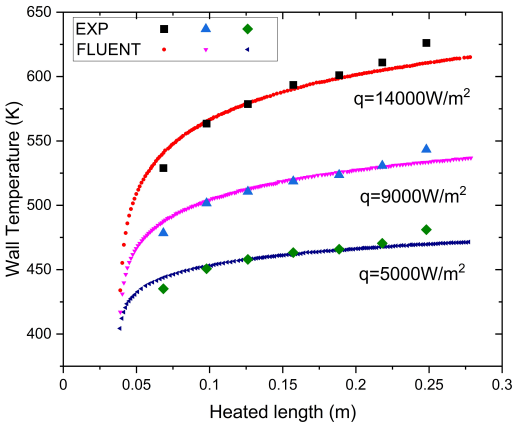

Figure 3.3: Single phase validation (Xia et al., 2024)

To validate the DPM method, the case with droplet injection is simulated according to the experimental boundary condition, which is listed in Table 3.1. In the experiment, the droplets have size distribution, whereas in the calculation, an average droplet diameter is taken to simplify the calculation.

Table 3.1: Boundary conditions of validation case

	Pressure	Inlet Vapor Temperature	Inlet Vapor Velocity	Heat Flux	Initial Droplet Diameter
	[MPa]	[K]	[m/s]	[kW/m^2]	[mm]
Case	0.1	388.15	15	14	0.01

Figure 3.4 compares the calculated wall temperature with the measured values. It can be seen that the overall agreement with the experimental results is good, which shows that the selected DPM model works well for dispersed flow calculations.

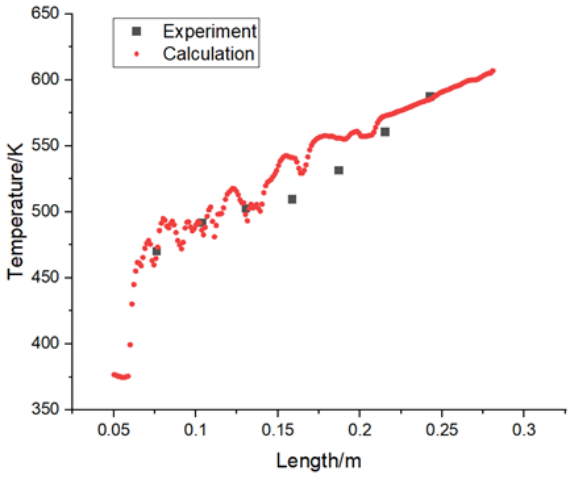

Figure 3.4: Comparison of experiment and predicted wall temperature in two-phase calculation (Xia et al., 2024)

3.3 Geometry and Boundaries

For the investigation of droplet behavior in the PDO region, a 1 m long tube with a 14.9 mm diameter is taken, followed the experiment test section of Becker et al. (1983), and is shown in Figure 3.5. Three mesh structures with different numbers of meshes are generated and single-phase calculations are conducted. Fluid flows upwards along the Z direction. The calculated wall temperature with three different mesh numbers is displayed in Figure 3.6(a). As seen, the effect of mesh number has a negligible effect on the predicted wall temperature in case that the mesh number is larger than 930,000. Therefore, from the mesh sensitivity analysis, the mesh with 930,000 is taken to conduct further simulation. Since the enhanced wall treatment is implemented in this simulation, the value of y^+ in the first layer mesh is examined and displayed in Figure 3.6(b). It can be seen that the y^+ value of all the cells in the first layer is lower than 1, which means the mesh is fine enough and meets the requirement of application of the enhanced wall treatment.

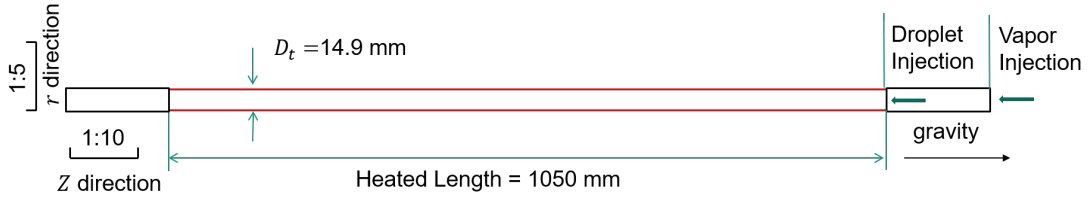

Figure 3.5: Geometry

In the calculation, the inlet boundary condition for the vapor phase is specified as a mass flow inlet, corresponding to the product of the steam quality at the dryout point and the total mass flow rate. The inlet mass flow rate of droplets is held constant; however, their initial diameters are varied to investigate the effects of droplet size on droplet behavior and wall temperature. An experimental case from Becker et al. (1983) is adopted as the reference condition. The boundary conditions for the selected cases are summarized in Table 3.2. At the dryout point, the steam quality is very high, and the droplet volume fraction is below 1%, which satisfies the applicability requirements of the DPM method. Three initial droplet diameters d_{p0} —0.05 mm, 0.1 mm, and 0.2 mm—are selected to assess the influence of initial droplet size.

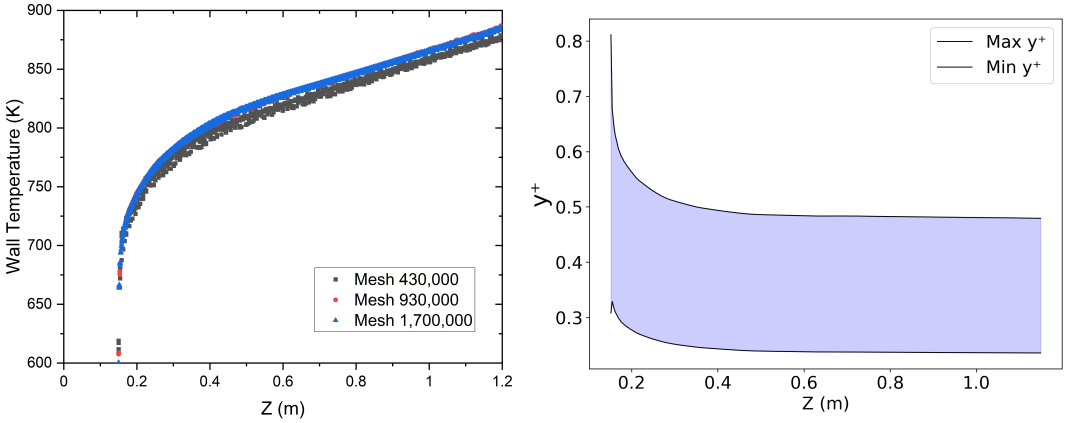

(a) Mesh sensitivity analysis

(b) The y^+ value of the first layer mesh

Figure 3.6: Mesh information

Table 3.2: Boundary conditions of reference case

	Pressure	Mass Flux	Heat Flux	Dryout Quality	Initial Droplet Diameter
	[MPa]	[kg/(m²·s)]	[kW/m²]	[—]	[mm]
Reference Case 1	7.0	500	466	0.883	0.1
Reference Case 2	7.0	500	466	0.883	0.2
Reference Case 3	7.0	500	466	0.883	0.05

3.4 Results Analysis

In this section, the predicted wall temperatures for the three reference cases are presented and compared with experimental data. The influences of droplet size, pressure, and mass flux on the vapor temperature profile are analyzed. The dynamic and evaporation behaviors of droplets are thoroughly investigated based on the reference cases. Additional simulations with constant wall temperatures and without droplet evaporation are performed to further explore droplet deposition behavior and the impact of evaporation on deposition.

3.4.1 Wall Temperature

The wall temperature measured in Becker's experiment and the predicted wall temperature by the current calculation are compared in Figure 3.7. The predicted wall temperatures with three initial droplet sizes encompass the profile of the measured wall temperatures from the experiment. This agreement further demonstrates the reliability of the current CFD model for simulating PDO heat transfer. It is also observed that injecting smaller droplets results in lower predicted wall temperatures. Additionally, the cross-sectional average vapor temperature for each case is presented. Initially, the average vapor temperature equals the saturation temperature, represented by the blue dashed line, but the degree of superheating increases along the test section. By the end of the section, the vapor is superheated by approximately 60°C. The case with smaller initial droplets yields a lower wall temperature and slower vapor temperature increase, while larger initial droplets result in higher wall and vapor temperatures. This indicates that smaller droplets provide more effective wall cooling in the PDO region.

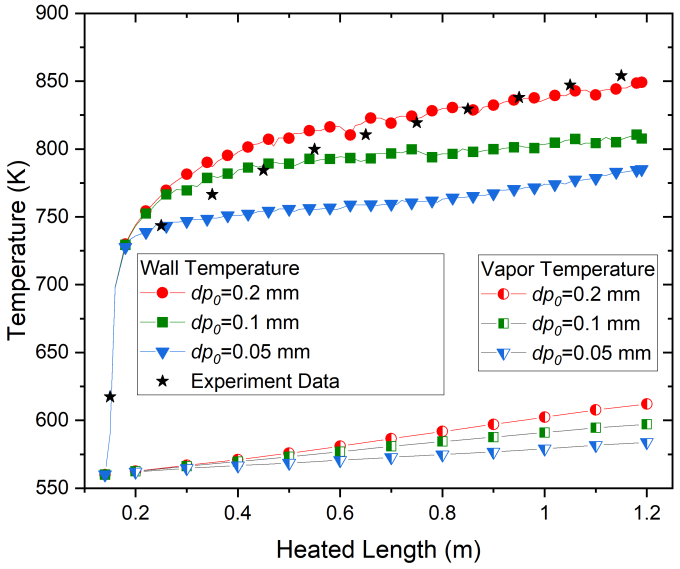

Figure 3.7: Droplet and vapor temperature distribution along heated length

3.4.2 Vapor Behaviors

The radial profiles of vapor temperature and vapor velocity for both the single-vapor case and the vapor-droplet mixture case are compared in Figure 3.8. It is observed that the vapor velocity decreases from the tube center toward the wall, while the vapor temperature increases with radial distance from the center. The light blue curve in the Figure 3.8(b) represents the saturation temperature. The vapor is highly superheated especially those close to the wall. Compared to the single-vapor case, the presence of droplets in

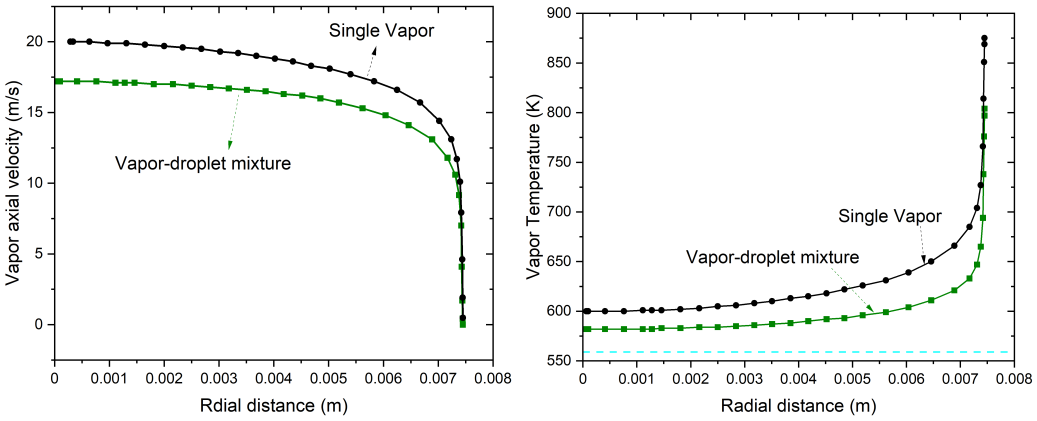

(a) Radial profiles of vapor velocity

(b) Radial profiles of vapor temperature

Figure 3.8: Comparison of radial distributions of vapor parameters in cases of single-phase and vapor-droplet mixture

the vapor-droplet mixture leads to lower vapor temperatures and velocities. Although droplet evaporation can increase steam quality and potentially enhance vapor velocity, the accompanying reduction in vapor temperature dominates, resulting in an overall decrease in vapor velocity in the presence of droplets evaporation.

To display the droplet effect on the vapor profiles, the dimensionless vapor temperature T^+ and dimensionless vapor velocity u^+ are calculated according to Equation (3.13). The dimensionless velocity u^* is determined by the wall shear stress τ_w with fluid properties

at the wall temperature, while the bulk vapor velocity is denoted as u_{vb}. For y^+ and T^+ calculations at various radial positions, vapor properties are referenced to the local vapor temperature T_v.

$$u^* = \sqrt{\frac{\tau_w}{\rho_{vw}}} \tag{3.13a}$$

$$u^+ = \frac{u_{vb}}{u^*} \tag{3.13b}$$

$$y^+ = y \cdot \frac{u^* \rho_v}{\mu_v} \tag{3.13c}$$

$$T^+ = \frac{(T_w - T_v)\, \rho_v c_{p,v} u^*}{q''_w} \tag{3.13d}$$

Figure 3.9 presents the non-dimensional temperature profile T^+ and velocity profile u^+ as a function of the wall-normal coordinate y^+ for both single-phase flow and vapor-droplet mixtures with varying initial droplet diameters. In Figure 3.9(a), it can be seen that the presence of droplets modifies the near-wall thermal behavior significantly. Notably, the case with the smallest droplet size ($d_{p0} = 0.05\,\text{mm}$) yields the highest T^+ values in the near-wall region ($y^+ < 300$). As shown earlier in Figure 3.7 this case also corresponds to a lowest wall temperature. Therefore, the increase in T^+ indicates a pronounced reduction in the local vapor temperature near the wall. This is attributed to the rapid evaporation of fine droplets, which absorb large amount of heat from the surrounding vapor during phase change, thereby steepening the temperature gradient. Consequently, the elevated T^+ reflects enhanced convective heat transfer driven by the high efficiency droplet evaporation. In contrast, larger droplets exhibit a more moderate influence on the thermal boundary layer, with their T^+ profiles approaching that of the single-phase case. On the other hand, the existence of droplets show less effects on u^+ profiles as shown in Figure 3.9(b), though significant differences persist between the curves due to the combined influence of evaporative cooling and enhanced vapor mass flux.

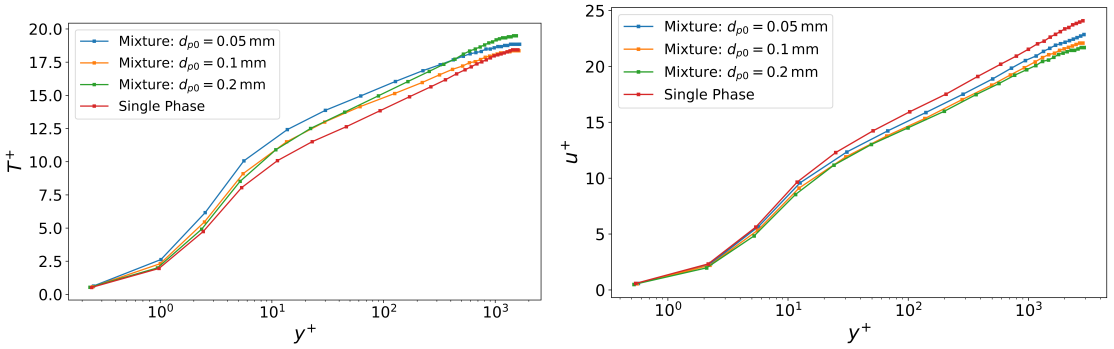

(a) Vapor temperature

(b) Vapor axial velocity

Figure 3.9: Dimensionless vapor temperature and vapor profile in the radial direction of reference cases

To examine the impact of droplet evaporation on vapor temperature profiles under varying boundary conditions, the cases listed in Table 3.3 are simulated, and the resulting T^+ profiles are shown in Figure 3.10.

Figure 3.10(a) shows the T^+ profiles for both low mass flux (Reference Case 2 in Table 3.2) and high mass flux (Case 3 in Table 3.3) with the initial droplet size of 0.2 mm. For the lower mass flux case, the T^+ profiles of the vapor-droplet mixture and the single-phase vapor are similar, as discussed previously. In the higher mass flux case, although

the relative difference becomes more pronounced, the slope of the T^+ profile remains comparable. This suggests that increasing mass flux has only a limited increase effect of droplet evaporation on the T^+ profile.

Figure 3.10(b) shows the T^+ profiles for vapor-droplet mixtures and single-phase vapor under varying pressure conditions (Reference Case 2 and Case 4 in Table 3.3), with a same initial droplet size of $d_{p0} = 0.2\,\text{mm}$. As pressure increases from 7 MPa to 12 MPa, the T^+ profile for the mixture becomes increasingly flatter, especially in the near-wall region. This indicates a slower increase in vapor temperature away from the wall, suggesting that droplet-induced evaporative cooling becomes more effective at higher pressures. Furthermore, the slope difference between the mixture and single-phase T^+ profiles becomes more pronounced with increasing pressure. This behavior implies that droplet evaporation has a stronger influence on the thermal boundary layer at elevated pressures, particularly near the wall.

Table 3.3: Boundary conditions of cases with different mass fluxes and pressures

	Pressure	Mass flux	Heat flux	Dryout Quality	Initial Droplet Diameter
	[MPa]	[kg/(m²·s)]	[kW/m²]	[—]	[mm]
Reference Case 2	7.0	500	466	0.884	0.2
Case 3	7.0	1000	604	0.705	0.2
Case 4	12.0	500	317	0.677	0.2

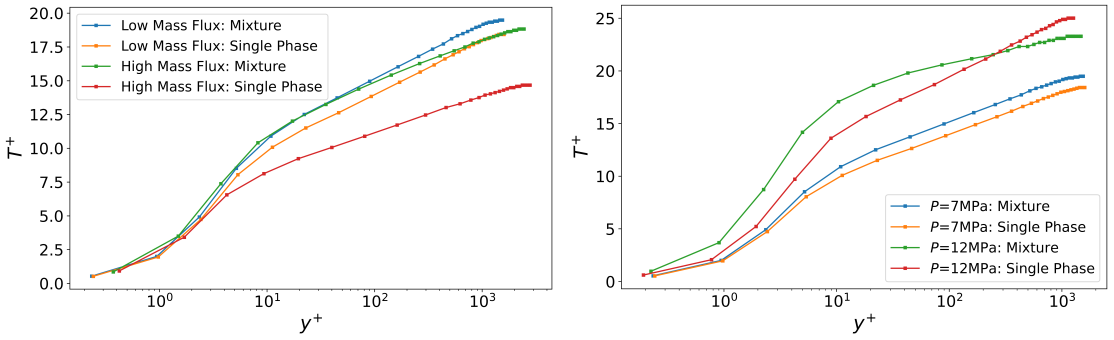

(a) vapor temperature profile under different mass flues

(b) Vapor temperature profile under different pressures

Figure 3.10: Dimensionless vapor temperature profile in radial direction of other cases

The enhanced modification on T^+ at high pressure can be attributed to a combination of factors, including longer droplet residence time in the vapor flow and a higher droplet volume fraction, both of which promote sustained heat absorption through phase change. As a result, the near-wall vapor is more effectively cooled, leading to a reduced local vapor temperature and a flatter T^+ gradient.

3.4.3 Droplet Dynamic Behaviors

In this section, the dynamic behavior of droplets—including size, spatial distribution, velocity, and mass concentration—is systematically analyzed based on the reference cases presented in Table 3.2. Building on this analysis, the evaporation characteristics of droplets

in the PDO region are examined in detail. A qualitative assessment is first conducted using contour plots of evaporation rate density, followed by a quantitative comparison of its radial distribution for various droplet sizes. Furthermore, the total evaporation of droplets in the entire flow region and on the wall surface is collected to investigate the proportion of droplet evaporation on the wall. The analysis of droplet evaporation highlights that droplet radial transport plays a critical role, not only in wall-droplet heat transfer but also in influencing the radial distribution of droplets, which in turn affects interfacial heat transfer. Therefore, the droplet deposition behaviors are investigated through the droplet moving trajectory, droplet radial velocity, and droplet overall lateral movement with different initial droplet sizes in detail. The radial velocities of the droplets are displayed in histogram form to statistically represent their radial movements. The overall lateral movements are quantitatively assessed based on three derived deposition parameters, net deposition mass flux, deposition velocity and entrainment velocity. In addition, the effects of droplet evaporation on the droplet deposition behavior under various wall temperatures are investigated based on these three parameters.

3.4.3.1 Dynamics of Droplets

In the process of heat exchange between droplets and superheated vapor, the droplet size and mass concentration primarily determine the available interfacial area for heat transfer. Droplet velocity directly influences the interfacial heat transfer efficiency. Additionally, due to the radial variation in vapor temperature, droplets at different radial positions experience significantly different thermal environments, leading to spatially varying evaporation characteristics. Therefore, this section presents the droplet size, spatial distribution, velocity, and mass concentration profiles to characterize droplet dynamics in the PDO region.

(A) Droplet size and location distribution

Prior to dryout, a liquid film exists on the wall, and droplets are subsequently entrained into the central vapor core, initially distributed within a radial range of 7 mm. Due to turbulence-induced transverse motion, the initially uniform droplet distribution becomes increasingly nonuniform along the axial direction. Simultaneously, droplet size evolves as the increase in heated length due to evaporation in the superheated vapor.

To enable statistical analysis of droplet characteristics, a 10-cm-thick slice from 1.05 m to 1.15 m in z direction is selected as the target zone. Figure 3.11 presents two complementary visualizations for the case with an initial droplet diameter of $d_{p0} = 0.2$ mm: the spatial distribution of droplets within the target zone and the radial profile of their mean size and variability to provide both qualitative and quantitative insights into the spatial organization and size variation of droplets under this condition.

Figure 3.11(a) shows the spatial distribution of droplets in this region for the case with an initial droplet diameter of $d_{p0} = 0.2$ mm. In this case, the relatively smaller total number of droplets facilitates clearer visualization. The droplets appear more densely clustered near the tube center and close to the wall. The color indicates droplet diameter, with lighter colors representing larger droplets. It is evident that droplets in the central region tend to be larger than those near the wall.

To further quantify the radial variation in droplet size, the mean droplet diameter is computed and plotted in Figure 3.11(b). Error bars represent the RMS deviation, indicating size dispersion at each radial position. The results show a clear trend: from the center toward the wall, the average droplet size decreases, while the size variability increases. Notably, in the near-wall region, although the mean droplet size is the smallest, large droplets are still present, as reflected in the high RMS values. This suggests strong local inhomogeneity in droplet evaporation and transport behavior.

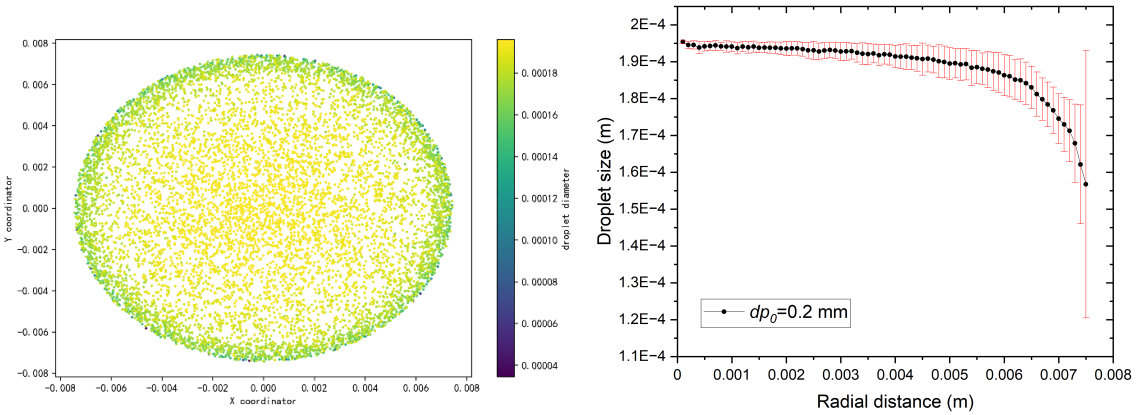

(a) Droplet scatter plot

(b) Droplet average size and error bar

Figure 3.11: Droplet scatter plot and radial distribution of droplet average size of $d_{p0} = 0.2\,\text{mm}$ in the target zone

(B) Droplet Velocity

According to Equation (3.3), the droplet Reynolds number used in the interfacial Nusselt number correlation is directly proportional to the velocity difference between the droplet and the surrounding vapor. A higher interfacial velocity leads to increased drag force and enhanced interfacial heat transfer. With the aid of CFD simulation, both the droplet velocity and the detailed velocity distribution can be quantitatively analyzed. Figure 3.12 presents the radial distribution of axial velocities within the selected analysis zone. The vapor axial velocities of individual mesh cells are indicated by red dots. From the figure, the radial profiles of droplet velocity, vapor velocity, and their difference are clearly illustrated. It is observed that the vapor axial velocity decreases with increasing radial distance from

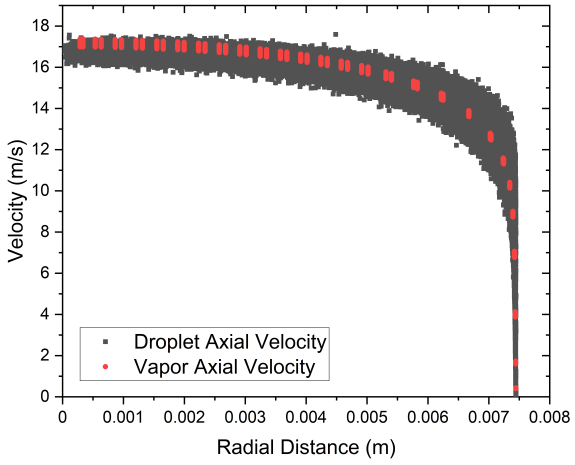

Figure 3.12: Plot of droplet and vapor axial velocity of case $d_{p0} = 0.1mm$ in the target zone

the centerline. Droplets exhibit a similar trend, as they are predominantly carried by the vapor flow. However, the spatial variation in droplet velocity is significantly larger than that of the vapor. In the central region, vapor typically travels faster than the majority of droplets. Conversely, near the wall, an increasing number of droplets exceed the local vapor velocity. Moreover, the dispersion in droplet axial velocity becomes more pronounced near the wall. Notably, some droplets in the near-wall region retain high axial velocities comparable to those found at the center, suggesting strong momentum and heat exchange

in the wall vicinity.

To get a clear droplet velocity distribution and the relative interfacial velocity, the target zone is divided into several sections along the radial direction and the average values are calculated for each section.

$$u_{vz} = \frac{\sum_{i=0}^{n} \rho_{v,i} u_{vz,i} V_{mesh,i}}{\sum_{i=0}^{n} \rho_{v,i} V_{mesh,i}} \tag{3.14a}$$

$$u_{dz} = \frac{\sum_{j=0}^{m} m_{d,j} u_{dz,j}}{\sum_{j=0}^{m} m_{d,j}} \tag{3.14b}$$

Here n and i in the Equation (3.14) refer to the total amount of mesh in this section and the ith mesh. m and j refer to the total amount of droplets number exist in this section and the jth droplet.

Figure 3.13 presents the calculated average axial velocities of droplets and vapor for two different initial droplet sizes. Due to the drag force, the droplets generally follow the vapor flow, exhibiting a similar velocity profile. However, in regions of high vapor velocity—particularly near the tube centerline—the droplet velocity slightly lags behind that of the vapor. As high-velocity droplets migrate from the center toward the wall, they experience deceleration due to the reduced vapor velocity in the near-wall region. Notably, the decrease in droplet velocity tends to lag behind the corresponding reduction in vapor velocity. As a result, droplets can retain relatively high velocities even in the vicinity of the wall, leading to an increased interfacial velocity. In the near-wall region, this interfacial velocity can reach values up to 5 m/s. When comparing cases with different initial droplet

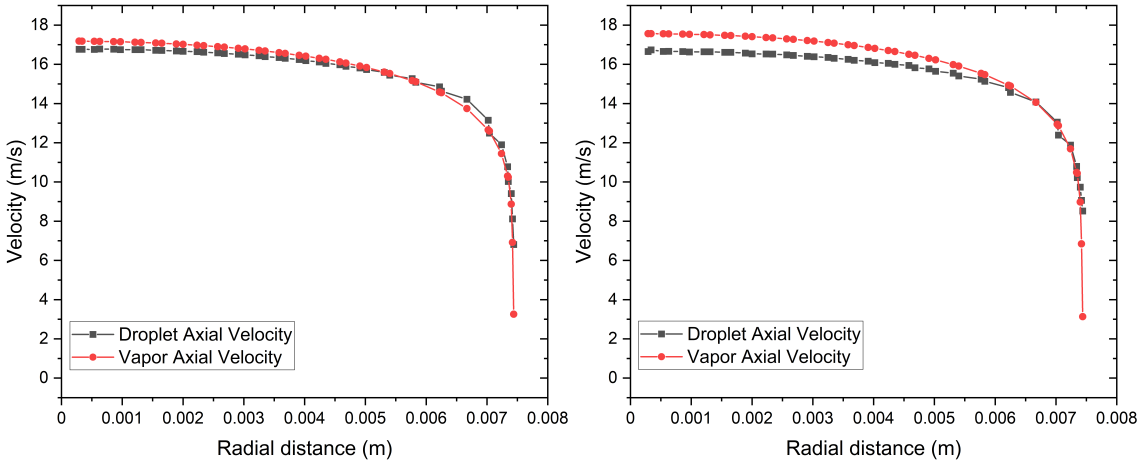

(a) d_{p0}=0.1 mm (b) d_{p0}=0.2 mm

Figure 3.13: Radial distribution of average axial vapor and droplet velocity

sizes, it is evident that the interfacial velocity is higher for larger droplets. This can be attributed to the greater inertia of larger droplets, which makes them less responsive to changes of surrounding vapor. This trend is consistent with the experimental observations reported by Lee and Almenas (1982), as shown in Figure 3.14. In Lee's study, the horizontal axis denotes the normalized radial position from the centerline to the wall, while the vertical axis represents the droplet velocity relative to the centerline vapor velocity. Similar to the present simulation, Lee's experimental results also demonstrate an increase in interfacial velocity with increasing radial distance to the tube center. And the interfacial velocity is also found larger in cases with larger droplet size. This agreement further

proves the validation of current CFD simulation. The absolute magnitude of interfacial velocity reported by Lee is significantly higher. This discrepancy is primarily due to the use of glass particles and air in Lee's experiments where the density ratio between phases approximately 50 times greater than that of the droplet–vapor system.

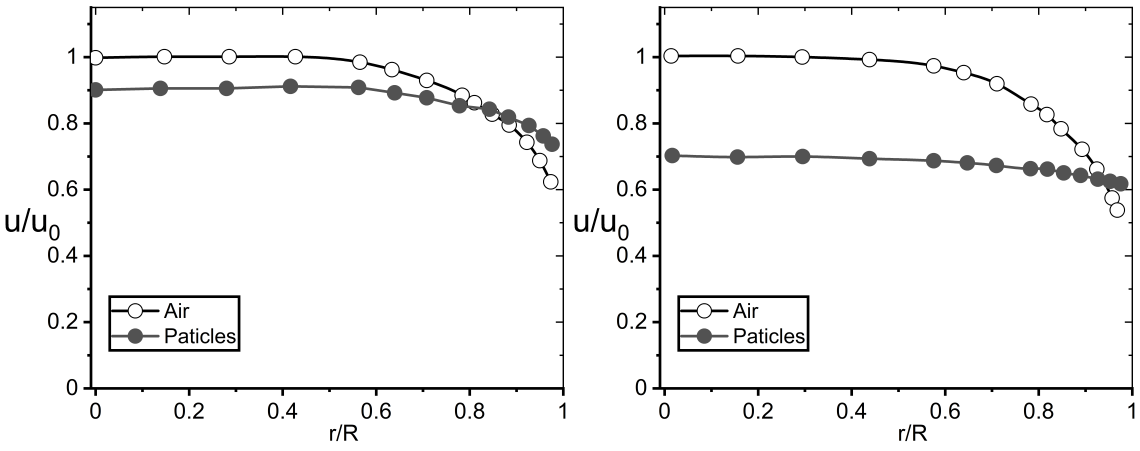

(a) d_{p0}=0.1 mm (b) d_{p0}=0.2 mm

Figure 3.14: Radial distribution of average axial vapor and droplet velocity from Lee and Almenas (1982)

(C) Droplet Mass Concentration

Considering the importance of droplet concentration in the interfacial heat transfer, the radial distributions of droplet mass flux in the target zone with three initial droplet sizes are plotted in Figure 3.15. Although the droplets are injected uniformly into the flow region, they later distribute in a W-shaped pattern. In the central region, the droplets exhibit a relatively high mass concentration, which decreases with increasing radial distance until it reaches a near-wall position. At this point, a sharp increase in mass concentration is observed, followed by a rapid decrease within the close wall region. Consequently, the droplet mass concentration distribution curve exhibits two peaks and one valley across the channel cross-section. This W-shaped distribution pattern is observed across all three cases. In the case with the largest initial droplet size, the droplet mass concentration along the radial distance remains consistently higher due to weak evaporation. Notably, the peak

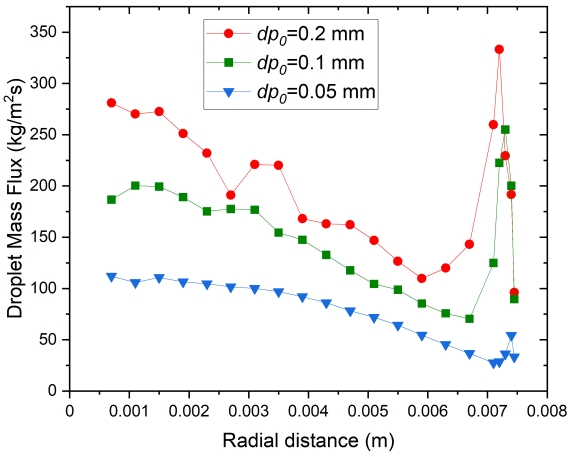

Figure 3.15: Radial distribution of droplet mass concentration with different initial droplet size in the target zone

mass concentration near the wall for droplets with d_{p0}=0.05 mm is smaller compared to the peak value in the central region, whereas in the other two cases, the near-wall peak is higher. This is caused by the intense evaporation happens in the near wall region.

3.4.3.2 Droplet Evaporation Behaviors

In superheated vapor flows, droplets absorb heat and gradually evaporate into the surrounding vapor, thereby increasing the overall vapor mass flow rate while simultaneously moderating the growth of vapor superheat. Droplet evaporation also alters the radial vapor temperature distribution, which in turn affects the convective heat transfer coefficient at the wall. In mechanistic modeling, one of the main challenges in predicting local steam quality and vapor temperature lies in the uncertainties associated with droplet evaporation behavior.

This section presents a detailed investigation of droplet evaporation characteristics in superheated vapor, based on CFD simulation results. The local evaporation rate is extracted at the mesh level. Since the mesh size varies between the near-wall and core regions, a normalized parameter—evaporation rate density—is introduced, defined as the evaporation rate per unit volume of each control volume. This enables a consistent comparison of evaporation intensity across the channel cross-section.

Figure 3.16 illustrates the spatial distribution of evaporation rate density in the target region for cases with initial droplet diameters of $d_{p0} = 0.1$ mm and $d_{p0} = 0.2$ mm. The near-wall region clearly exhibits much stronger evaporation than the core, especially for $d_{p0} = 0.1$ mm. A distinct high-evaporation layer forms adjacent to the heated surface, with intensity increasing toward the wall. Although evaporation intensity is generally lower in the $d_{p0} = 0.2$ mm case, a pronounced radial disparity remains, with evaporation concentrated near the wall. These findings highlight the strong dependence of evaporation dynamics on initial droplet size and radial location in superheated vapor flows.

To better illustrate the radial distribution of droplet evaporation, the mesh layer at a height of 1.1 m is extracted and divided into 20 annular sections. Figure 3.17(a) presents the evaporation rate density of each section, defined as the total mass source within the section divided by its volume. As shown, the evaporation rate density rises sharply from the tube center toward the wall, with the maximum difference exceeding an order of magnitude. Within 1 mm of the wall, the average evaporation rate density is about twice that of the entire cross-section and three times higher than that of the central region. This pronounced near-wall evaporation explains the smaller droplet sizes observed in Figure 3.11, as well as the sharp decrease in droplet mass concentration in the near-wall zone. When comparing cases with different initial droplet sizes, the evaporation rate density remains similar in the central region but diverges significantly near the wall, with local differences reaching a factor of two.

The vapor temperature distribution at the same axial location is shown in Figure 3.17(b). For larger initial droplet sizes, the vapor temperature at a given radial location is consistently higher. Together with Figures 3.15 and 3.17(b), it is evident that the case with $d_{p0} = 0.05$ mm yields the lowest droplet mass concentration and the lowest average vapor temperature, yet exhibits the highest evaporation rate density. This indicates that the initial droplet size at the dryout point plays a decisive role in determining interfacial heat transfer efficiency and the resulting wall temperature distribution in the PDO region.

The total droplet evaporation rates over the entire heated section are summarized in Table 3.4. As the initial droplet size decreases, the overall evaporation rate increases. However, the difference among cases is smaller than that in initial droplet surface area, which directly governs interfacial heat transfer. For instance, halving the droplet diameter

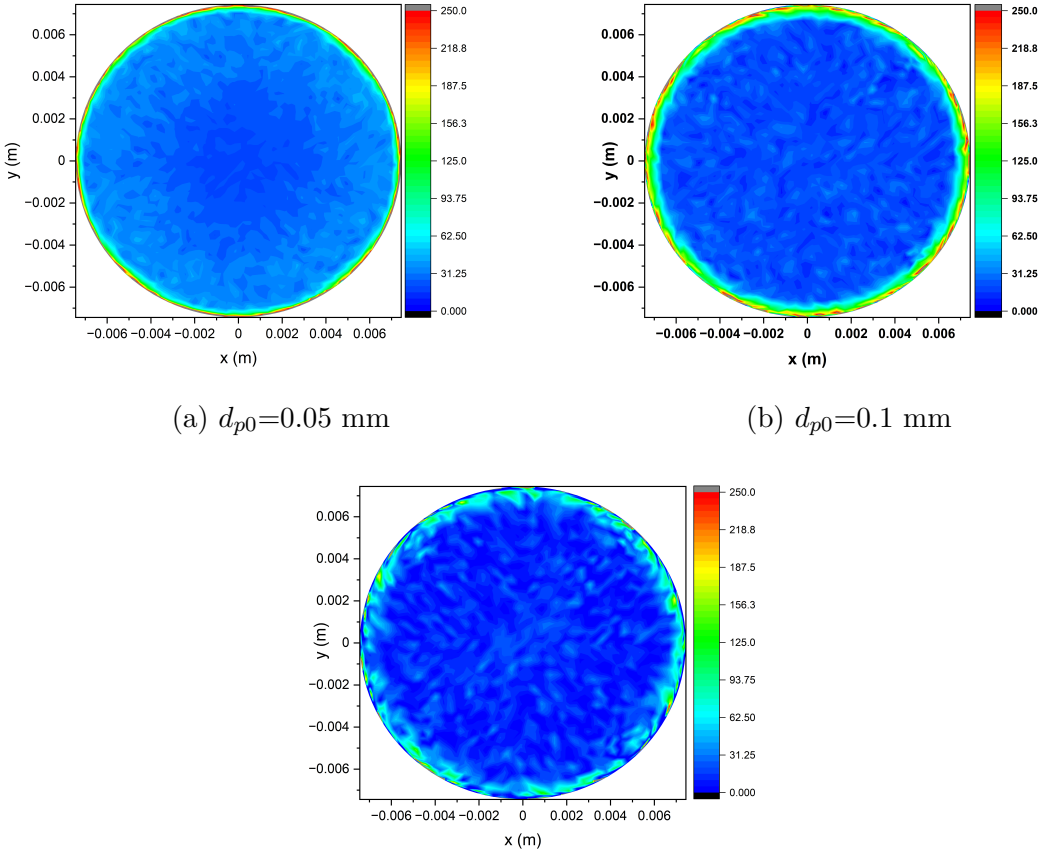

(a) d_{p0}=0.05 mm

(b) d_{p0}=0.1 mm

(c) d_{p0}=0.2 mm

Figure 3.16: Contour of evaporation rate density in the target zone

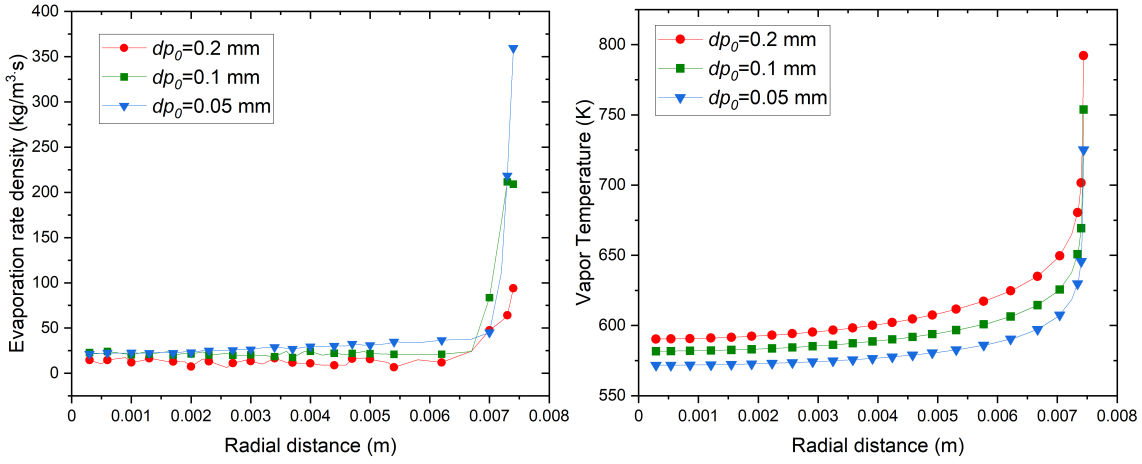

(a) Evaporation rate density profile

(b) Vapor temperature profile

Figure 3.17: Radial distribution of evaporation rate density and vapor temperature

doubles the total interfacial area at the inlet (for equal droplet mass flow rates), but the overall evaporation rate does not increase by the same factor. According to interfacial heat transfer models, larger droplets yield higher vapor temperatures because of their lower evaporation rates. Overall, the difference in interfacial area due to droplet size exerts the dominant influence on evaporation.

Table 3.4 also lists the evaporation rate from wall-adjacent cells, showing that less than 2% of total droplet evaporation occurs directly on the wall in the PDO region. Moreover, for larger droplets, the wall temperature is higher and the ratio of wall evaporation to total evaporation is lower.

Table 3.4: Droplet evaporation rate on the wall

	Overall evaporation rate [kg/s]	Evaporation rate on wall [kg/s]	Ratio [%]
$d_{p0} = 0.05\,\text{mm}$	7.95×10^{-3}	9.30×10^{-5}	1.1698
$d_{p0} = 0.1\,\text{mm}$	5.19×10^{-3}	3.76×10^{-5}	0.7245
$d_{p0} = 0.2\,\text{mm}$	2.53×10^{-3}	1.56×10^{-5}	0.6166

This observation supports the hypothesis that the high evaporation rate in the near-wall region in Figure 3.11(a) occurs within the vapor layer adjacent to the wall, where superheating is significant. To confirm this, the evaporation rates of all mesh cells within 1 mm of the wall are summed and compared with the total evaporation rate. As shown in Table 3.5, approximately 50% of the droplet evaporation takes place within this 1 mm-thick near-wall region, which accounts for only 25% of the cross-sectional area. This implies that the evaporation efficiency in the near-wall region is approximately three times that in the central region.

This analysis highlights a stark contrast between droplet evaporation behaviors in the center and near-wall regions. However, most mechanistic models for PDO interfacial heat transfer rely on cross-sectionally averaged quantities, such as mean vapor temperature and uniform droplet concentration. The present CFD results suggest that interfacial heat transfer in the PDO region should be modeled separately for the central and near-wall zones, accounting for their distinct vapor temperature distributions and droplet evaporation rates.

Table 3.5: Droplet evaporation rate in the near-wall region

	Overall evaporation rate [kg/s]	Near-wall evaporation rate [kg/s]	Ratio [%]
$d_{p0} = 0.05\,\text{mm}$	7.95×10^{-3}	3.73×10^{-3}	46.87
$d_{p0} = 0.1\,\text{mm}$	5.19×10^{-3}	3.01×10^{-3}	57.82
$d_{p0} = 0.2\,\text{mm}$	2.53×10^{-3}	1.39×10^{-3}	54.94

3.4.3.3 Droplet Deposition Behaviors

It is well established that particles suspended in gas flows tend to migrate toward and deposit on the wall. Numerous correlations for particle deposition rates have been developed based on non-heated experiments (Lee and Almenas, 1982; Liu and Ilori, 1974). In contrast, limited research has addressed droplet deposition on heated walls. The presence of droplet evaporation near heated walls introduces additional complexity that can significantly affect deposition behavior. Furthermore, in previous mechanistic models, droplet deposition was typically considered only in the context of wall–droplet heat transfer, where the deposition rate was calculated to estimate the number of droplets undergoing direct thermal contact with the wall. However, as indicated in Table 3.4 and Table 3.5, the actual evaporation occurring on the wall surface is minimal compared with that in the adjacent near-wall vapor layer.

In the central region, where the vapor temperature is relatively low, the evaporation rate is limited, as shown in Section 3.4.3.2. In contrast, the near-wall region exhibits significantly higher vapor temperatures, resulting in elevated evaporation rates. As droplets near the wall evaporate, their loss is continuously offset by transverse droplet transport from the central region, thereby sustaining high evaporation rates. This dynamic highlights the importance of transverse droplet motion in influencing interfacial heat transfer efficiency.

Therefore, this section focuses on a detailed analysis of droplet deposition behavior in the PDO region. First, a statistical characterization of droplet transverse motion in superheated turbulent vapor flow is conducted. Subsequently, three deposition parameters are defined and applied to quantitatively assess the radial migration of droplets from the central to the near-wall region, as well as the influence of evaporation on the overall deposition process.

(A) Droplet Trajectories

From Equation (3.1), the lateral movement of droplets in the vapor flow is governed by the drag force, which depends on the velocity difference between the instantaneous vapor velocity and the droplet velocity. According to the stochastic dispersion method, the instantaneous vapor velocity is represented as the sum of the mean velocity and the fluctuation velocity (Equation (3.5)). In the radial direction, the time-averaged velocity is very small compared with the fluctuation velocity. Thus, droplet transverse motion in the vapor flow is primarily controlled by the fluctuation velocity.

In Figure 3.18, the trajectories of 4 droplets with initial diameter d_{p0}=0.2 mm are shown. Their trajectories are tracked over 25 time steps, with a time step length of 0.001 s.

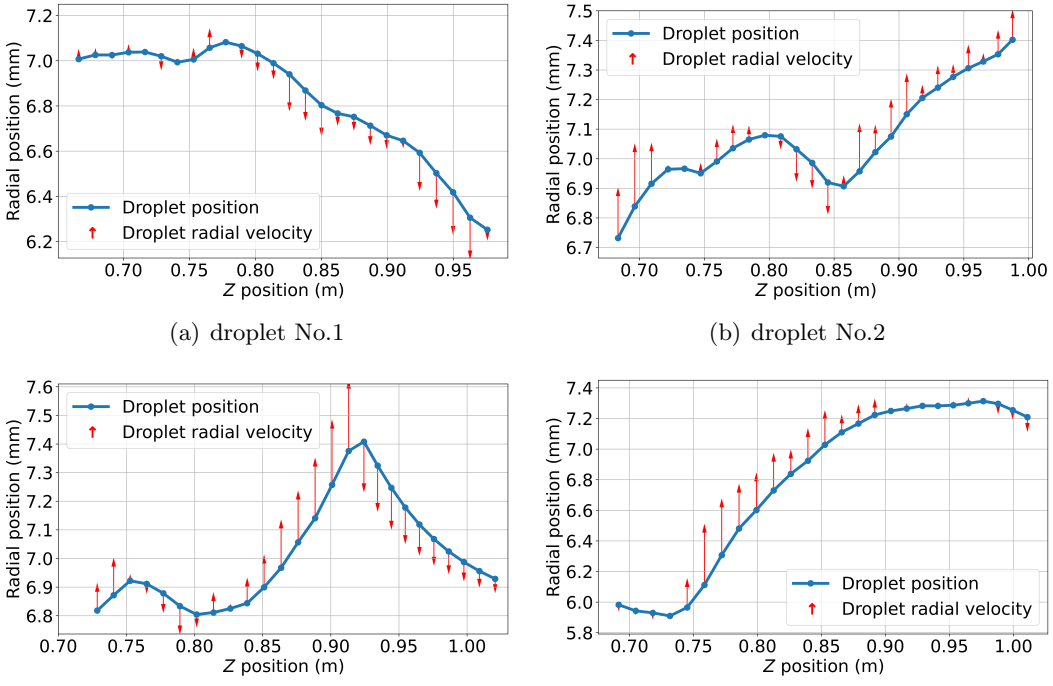

(a) droplet No.1

(b) droplet No.2

(c) droplet No.3

(d) droplet No.4

Figure 3.18: Examples of droplet trajectory in the near wall region with case of d_{p0}=0.2 mm (Xia and Cheng, 2025b)

The horizontal axis represents the droplet position in the z-direction, while the vertical axis represents the radial position of the droplet relative to the center of the tube. The

red arrow indicates the radial velocity of the droplet at that position. The arrow length corresponds to the magnitude of the radial velocity, and its direction indicates the velocity direction. When the arrow points toward decreasing radial position, the radial velocity is negative, and the droplet moves toward the heated wall.

Figure 3.18(a) shows the trajectory of a droplet leaving the near-wall region. During the lateral movement, the droplet also moves axially from a height of 0.65 m to 1.0 m. Initially, the droplet fluctuates in the near-wall region, where its radial velocity is so small that the arrow is nearly invisible. As it moves away from the wall, its radial velocity increases. The rising velocity enhances the interfacial drag force, which subsequently reduces the droplet velocity as it approaches a radial distance of 6.6 mm. Thereafter, the droplet accelerates again due to the fluctuation velocity and moves toward the tube center at relatively high speed.

The droplet trajectory in Figure 3.18(b) illustrates a droplet moving toward the wall along a more tortuous path. Initially, the droplet attempts to approach the wall but experiences deceleration and is temporarily redirected in the opposite direction. Subsequently, it passes the control volumes with fluctuation velocity toward the wall, allowing it to resume movement in that direction. After several time steps of gradual approach, the droplet is likely to reach the wall in subsequent steps.

Figure 3.18(c) shows the trajectory of a droplet that reaches and impacts the wall. The droplet initially fluctuates at the edge of the near-wall region, then accelerates toward the wall and finally touches it at high velocity. The wall impaction rebounds the droplet back into the flow, changing its velocity direction. After reflection, the droplet moves toward the main flow with decreasing velocity.

In contrast, Figure 3.18(d) shows a droplet attempting to approach the wall but continuously decelerating. Its velocity becomes nearly imperceptible as it nears the wall. The droplet fluctuates in the near-wall region until the last three time steps. It acquires a small negative radial velocity but remains in the near-wall region. Comparison between droplets No. 3 and No. 4 reveals that droplets exhibit different behaviors when moving toward the wall: some accelerate and reach the wall, bouncing back, while others decelerate and fluctuate near the wall without reaching it.

These trajectories suggest that droplets experience random drag forces in both magnitude and direction due to turbulence. Only those droplets that regain sufficient radial velocity through turbulent interactions with the vapor phase can eventually reach the wall. Moreover, droplets passing through the buffer layer may be reflected back into the main flow, become trapped within the buffer layer, or continue fluctuating in the near-wall region.

(B) Droplet Radial Velocity

To statistically analyze droplet lateral movement, the distribution and average droplet radial velocity are selected as key parameters from the simulation results. The statistical method used is depicted in Figure 3.19(a). To ensure statistical significance, an area with height Δz and thickness Δr is chosen at a radial distance r_c from the center of the tube. Δr is defined as 0.1 times the distance to the wall. All droplets in this area are collected, as shown in Figure 3.19(b).

To investigate lateral movement, the droplet radial velocity is presented as a histogram, showing the radial velocity and the corresponding droplet count within a velocity range. The radial distance r_c is set to 7 mm, where vapor temperature and evaporation rate density begin to increase (Figures 3.16 and 3.17). Δz is set to 0.3 m, ensuring a sufficient number of droplets for analysis. For instance, in the case with $d_{p0} = 0.2$ mm, although the

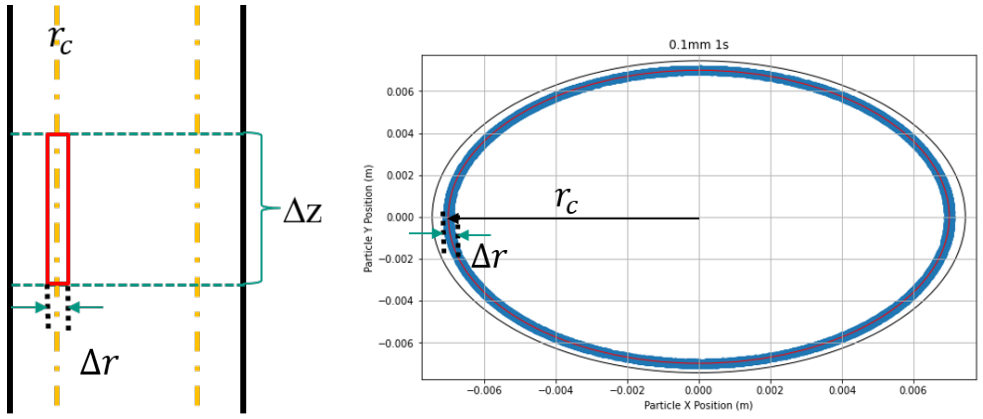

(a) Front view (b) Top view

Figure 3.19: Droplets collection method for averaging the droplet radial velocity

droplet count is lower than in other cases, approximately 6,000 droplets are still collected within this selected area.

In Figures 3.20 and Figure 3.21, the radial velocity of droplets in the case of d_{p0}=0.2 mm and d_{p0}=0.05 mm are selected to illustrate the distribution of droplet radial velocity and to examine the effect of droplet size. The width of each bin is .4.02 m/s.

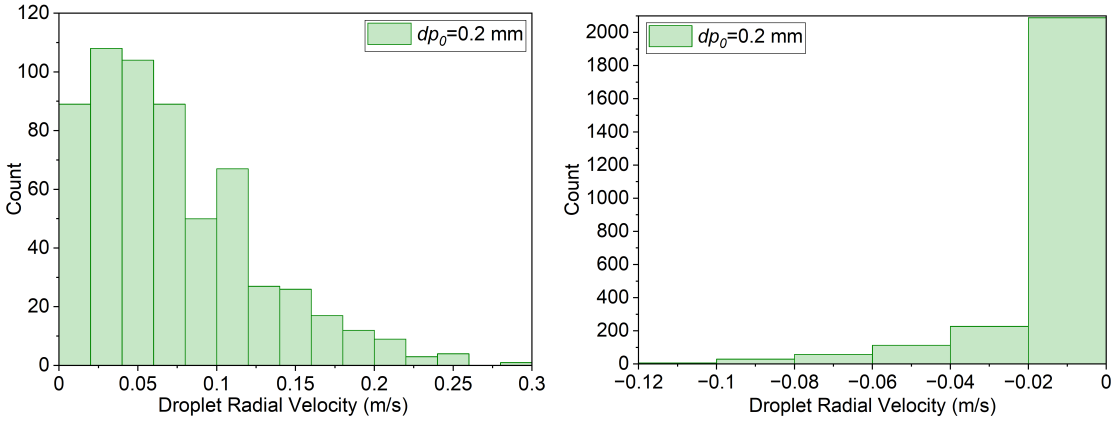

(a) Droplet with positive radial velocity (b) Droplet with negative radial velocity

Figure 3.20: Droplets radial velocity of case d_{p0}=0.2 mm (Xia and Cheng, 2025b)

As can be seen from Figure 3.20(a) and Figure 3.20(b), the distribution of droplets with positive radial velocity roughly conforms to the normal distribution in positive x-axis. However, Figure 3.20(b) reveals a high concentration of droplets with small negative radial velocities, a trend that becomes even more pronounced in Figure 3.21(b). Approximately 2,000 out of 6,000 droplets (33%) in case of d_{p0}=0.2 mm have very small negative radial velocity. In the case of d_{p0}=0.05 mm, 35,000 out of 40,000 droplets fall into this category, accounting for as high as 87.5%. These figures indicate that smaller droplet sizes are associated with a higher proportion of droplets exhibiting small negative radial velocities. Additionally, droplets with smaller initial droplet sizes display a broader range of radial velocities in both directions. Droplets with large radial velocities are relatively rare; for instance, in the case with d_{p0}=0.2 mm, only 42 droplets have radial velocities exceeding 0.4 m/s, comprising just 1.65% of all droplets with positive radial velocities. Similarly, only 5 droplets exhibit radial velocities smaller than -0.4 m/s. Comparing the number of droplets with absolute radial velocities greater than 0.1 m/s, there are 2,424 droplets in

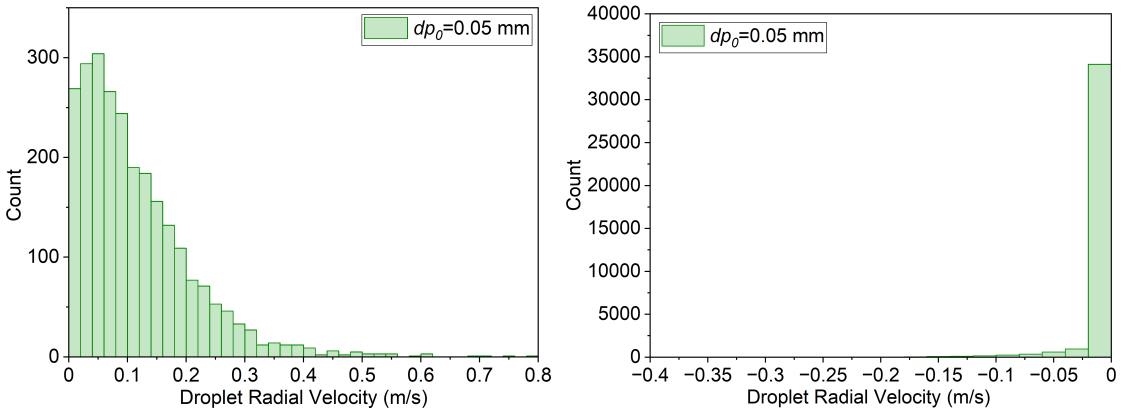

(a) Droplet with positive radial velocity (b) Droplet with negative radial velocity

Figure 3.21: Droplets radial velocity of case d_{p0}=0.05 mm

the left-hand figure and only 487 droplets in the right-hand figure. The average droplet radial velocity with a positive value is called average radial velocity in the following text. In the case with d_{p0}=0.2 mm the average radial velocity is 0.111 m/s while in the case with d_{p0}=0.05 mm it is 0.205 m/s.

From the droplet trajectory shown in Figure 3.18, the droplet radial velocity always changes as it approaches the wall. Thus, by adjusting the value of r_c, droplets are collected at varying distances from the wall to construct the radial profiles of the average droplet radial velocity toward the wall. In Figure 3.22, the x-axis is the distance from the collection region

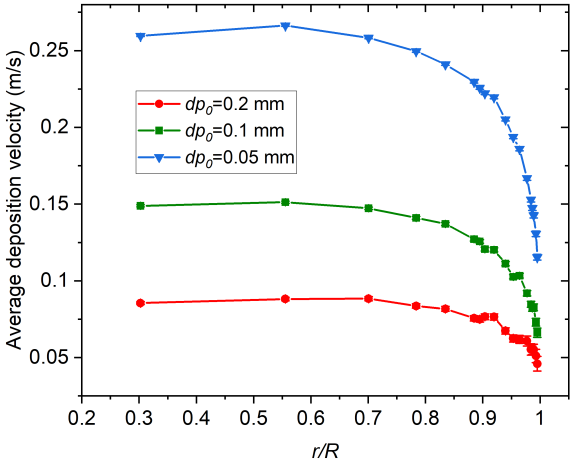

Figure 3.22: Radial distribution of droplet average radial velocity toward the wall (Xia and Cheng, 2025b)

to the tube center, r_c, divided by the tube radius R. The y-axis represents the average deposition velocity at this radial position. The error bars in the figure represent the standard error (SE) of the droplet's average deposition velocity. The deposition velocity profile exhibits a decreasing trend as the distance to the wall decreases. A significant difference in deposition velocity is observed between the central region and the near-wall region. The deposition velocity for droplets with smaller initial sizes is consistently higher than for those with larger initial sizes. Therefore, the droplet diameter has a pronounced effect on the droplet deposition velocity.

(C) Analysis with derived droplet deposition parameters

To more effectively capture the overall lateral movement of the droplets, three deposition parameters, droplet deposition mass flux, deposition velocity and entrainment velocity are derived based on the method illustrated in Figure 3.23. At time t, a region with a height

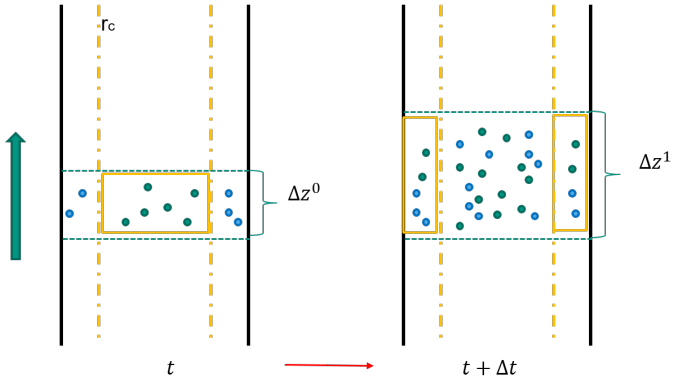

Figure 3.23: Post-processing method

of Δz^0 is selected, and the flow domain is divided into a central region and a near-wall region based on a cutoff distance r_c. For the subsequent analysis, r_c is set to 7 mm as in the previous evaporation analysis. Sensitivity analysis is also performed with different values of r_c and found that the selection of r_c value does not affect the trends of deposition parameters in the near wall region. After one time step Δt, the height of the flow domain is extended to Δz^1. The distance of Δz^1 is based on the criterion that the axial distance traveled by droplets within one time step cannot exceed the length difference $\Delta z^1 - \Delta z^0$. At time $t + \Delta t$, droplets are identified again and compared with the droplets collected at the previous time point. Droplets that were in the central region at time t and appear in the near-wall region at time $t + \Delta t$ are identified as deposition from the central region to the near-wall region. Similarly, droplets that were in the near-wall region at time t but are found in the central region at time $t + \Delta t$ are classified as entrainment from the near-wall region to the central region. The corresponding mass flux is calculated by:

$$\dot{m}_{d,c-n} = \frac{\sum_0^i m_{d,c-n}}{\Delta t * \Delta z^0 * 2r_c * \pi} \tag{3.15}$$

The droplet mass flux from the near-wall region to the central region is identified as $\dot{m}_{d,n-c}$ and calculated by:

$$\dot{m}_{d,n-c} = \frac{\sum_0^n m_{d,n-c}}{\Delta t * \Delta z^0 * 2r_c * \pi} \tag{3.16}$$

The droplet net deposition mass flux is calculated by:

$$\dot{m}_{d,net} = \frac{\sum_0^n m_{d,c-n} - \sum_0^j m_{d,n-c}}{\Delta t * \Delta z^0 * 2r_c * \pi} \tag{3.17}$$

The calculated mass fluxes of cases with different initial droplet sizes are shown in Table 3.6. It can be seen that, in contrast to the results presented in Figure 3.22—where smaller droplets exhibit higher average deposition velocities—the droplet mass flux from the central region to the near-wall region, as shown in Table 3.6 increases with droplet size. However, as the droplet mass flux from the near-wall region to the central region also increases with droplet size, the net deposition flux does not show a clear dependence on droplet size.

In cases with different initial droplet sizes, varying droplet mass concentrations are observed at same heated length due to differences in evaporation rates. Larger droplets,

Table 3.6: Droplet deposition mass flux

	$\dot{m}_{d,c-n}$ [kg/(m²·s)]	$\dot{m}_{d,n-c}$ [kg/(m²·s)]	$\dot{m}_{d,net}$ [kg/(m²·s)]
d_{p0}=0.05 mm	0.06498	0.02079	0.04419
d_{p0}=0.1 mm	0.07937	0.03149	0.04788
d_{p0}=0.2 mm	0.09328	0.04996	0.04332

with lower evaporation rates, retain higher mass concentrations, which in turn influences droplet deposition. Therefore, to eliminate the influence of droplet concentration, the derived droplet velocities for radial movement are calculated by:

$$k_{d,c\text{-}n} = \frac{\dot{m}_{d,c\text{-}n}}{C_c} \tag{3.18}$$

$$k_{d,n\text{-}c} = \frac{\dot{m}_{d,n\text{-}c}}{C_n} \tag{3.19}$$

C_c and C_n are the droplet mass concentration in the central and near-wall region of the target zone. The derived droplet lateral velocities $k_{d,c-n}$ and $k_{d,n-c}$ refer to deposition velocity and entrainment velocity in this study, representing the lateral exchange of droplets between two regions. The calculated results are displayed in Table 3.7 and show that after removing the influence of droplet concentration, the deposition velocity of droplets from the central region to the near-wall region increases as droplet size decreases, which is consistent with the observation from Figure 3.22. This comparison highlights the dependence of droplet deposition velocity on droplet size.

Table 3.7: Calculated droplet deposition velocity and entrainment velocity

	$k_{d,c\text{-}n}$ m/s	$k_{d,n\text{-}c}$ m/s
$d_{p0} = 0.05\,\text{mm}$	0.05182	0.01971
$d_{p0} = 0.1\,\text{mm}$	0.03937	0.00664
$d_{p0} = 0.2\,\text{mm}$	0.03146	0.00893

(D) Comparison with literature correlations

Previous deposition correlations typically estimate deposition velocities by calculating the rate at which particles deposit from the turbulent core to the edge of the buffer layer, corresponding to a y^+value of approximately 30. For comparison with correlations in the literature, the boundary between the central and near-wall regions is now set at $y^+ = 30$, where the value of r_c is 6×10^{-5}, as derived from the CFD-calculated wall shear stress. The deposition mass flux between the turbulent core and the buffer layer is calculated and shown in Table 3.8. The calculated deposition and entrainment mass fluxes at $y^+ = 30$ are significantly smaller than those in Table 3.6, consistent with the trend in Figure 3.22, where droplet deposition velocity decreases as particles approach the wall.

The correlations of Yang and Lee (1991), Friedlander and Johnstone (1957) and Kataoka et al. (1983) are displayed in Table 3.9. The calculated deposition velocity obtained from

Table 3.8: Droplet deposition mass flux from turbulent core to buffer layer of reference case 1

	$\dot{m}_{d,c\text{-}n}$	$\dot{m}_{d,n\text{-}c}$	$\dot{m}_{d,\text{net}}$
	[kg/(m$^2\cdot$ s)]	[kg/(m$^2\cdot$ s)]	[kg/(m$^2\cdot$ s)]
$d_{p0} = 0.1$ mm	0.05119	0.04457	0.00662

Table 3.9: Droplet deposition correlations from literature for comparison

Authors	**Correlations**
Yang and Lee	$k_d = u^* \dfrac{1.224\eta_b}{1.33 + 2.44\eta_b \ln\left(\dfrac{1+2\left(1-\frac{30}{Re}\sqrt{\frac{C_f}{2}}\right)^2}{1-\left(1-\frac{30}{Re}\sqrt{\frac{C_f}{2}}\right)^2}\right)}$
Friedlander and Johnstone	$k_d = \begin{cases} u^* \left[\dfrac{1}{\frac{1}{\sqrt{C_f/2}} + \left(\frac{1525}{0.81\tau_+^2} - 50.6\right)}\right], & \tau_+ < 5.6 \\ u^* \left[\dfrac{1}{\frac{1}{\sqrt{C_f/2}} - 13.73 + 5\ln\left(\frac{5.04}{\tau_+/5.56 - 0.959}\right)}\right], & 5.6 \le \tau_+ < 33.3 \\ u^* \sqrt{\dfrac{C_f}{2}}, & \tau_+ \ge 33.3 \end{cases}$
Kataoka et al.	$k_d = \dfrac{\mu_g}{D_t} \cdot 0.22\, Re_l^{0.75} \left(\dfrac{\mu_g}{\mu_l}\right)^{0.26}$

the simulation and literature are compared Table 3.10. It shows that the deposition velocity of correlations from literature are much larger than the CFD simulation results. Considering the droplet entrainment, the net droplet deposition mass flux is less in the CFD simulation. This comparison further proves the idea that the current droplet deposition models are not suitable for the PDO heat transfer.

Table 3.10: Comparison of deposition velocities from turbulent core to buffer layer across different models

	Current Simulation	**Yang Correlation**	**Friedlander Correlation**	**Kataoka Correlation**
Deposition Velocity (m/s)	0.02198	0.14280	0.04313	0.53519

3.4.3.4 Evaporation Effect on Droplet Deposition

In the PDO region, droplet evaporation alters the profiles of vapor temperature and velocity, which in turn influence droplet behavior, as also noted by Meholic (2011). Given the

more intense evaporation near the wall, it can be inferred that the impact of evaporation on droplet trajectories is likely more pronounced in this region. However, the effects of evaporation on droplet deposition have not been extensively investigated, and experimental studies are particularly challenging. CFD simulations, by contrast, offer valuable insights into droplet deposition behavior under evaporative conditions. This subsection will thoroughly examine and analyze the effect of droplet evaporation on the droplet movement between the central region and near-wall region.

To study the effect of evaporation on droplet deposition, the models for interfacial heat and mass transfer in the case without evaporation are modified as follows: droplets absorb heat from the superheated vapor, but will not evaporate and no mass transfer between phases takes place. Numerical simulations for both cases-with and without evaporation-are conducted under the same constant wall temperature to ensure more comparable vapor temperature profiles. Apart from the wall boundary condition, the initial conditions follow those outlined in Table 3.2. A constant wall temperature of T_w=800 K is applied, as this value closely matches the average measured wall temperature.

Figure 3.24 presents the histogram of droplet radial velocities for the case with evaporation, which aligns with the trend observed in Figure 3.22: the droplets with positive radial velocity in Figure 3.24(a) almost follow the normal distribution in positive half-axis, while a considerable number of droplets have a smaller negative radial velocity in Figure 3.24(b). Figure 3.25 shows the histogram of droplet radial velocities in the case without evaporation. The droplets with positive radial velocity in Figure 3.25(a) do not follow a Gaussian distribution, with a greater number of droplets with smaller positive radial velocity. Additionally, Figure 3.25(b) indicates a reduction in the number of droplets with small negative radial velocities compared to the case with evaporation shown in Figure 3.24(a). This comparison suggests that, in the presence of evaporation, more droplets tend to move away from the wall rather than towards it. Evaporation significantly impacts the radial velocities of the droplets, particularly by altering the direction of droplets with small positive radial velocities, thereby reducing the number of droplets moving towards the wall.

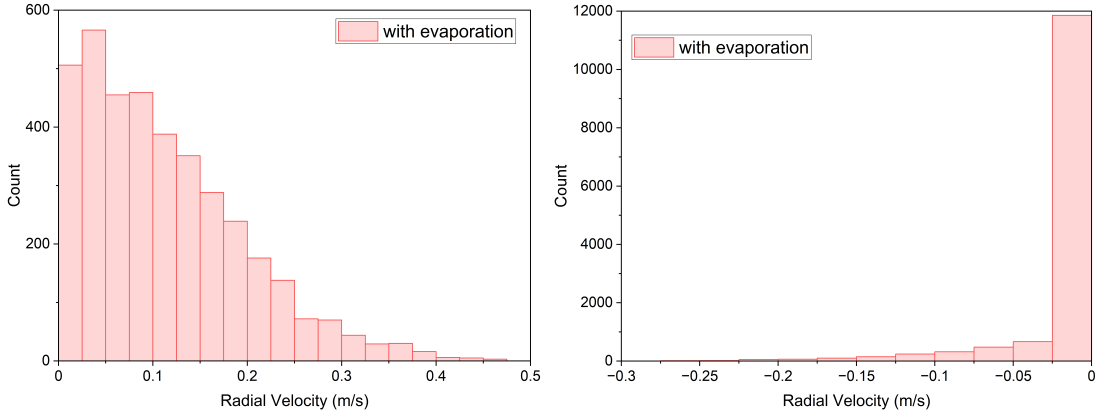

(a) Droplet with positive radial velocity

(b) Droplet with negative radial velocity

Figure 3.24: Droplets radial velocity of case $T_w = 800K$ d_{p0}=0.1 mm with evaporation (Xia and Cheng, 2025b)

The substantial increase in the number of droplets with small positive radial velocities renders the average velocity an inadequate metric for representing the statistical characteristics of droplet radial velocity in cases without evaporation. To analyze the effect of evaporation on droplet deposition behavior, the net deposition mass flux, deposition velocity, and entrainment velocity-defined in Equations (3.18) and (3.19) are presented in

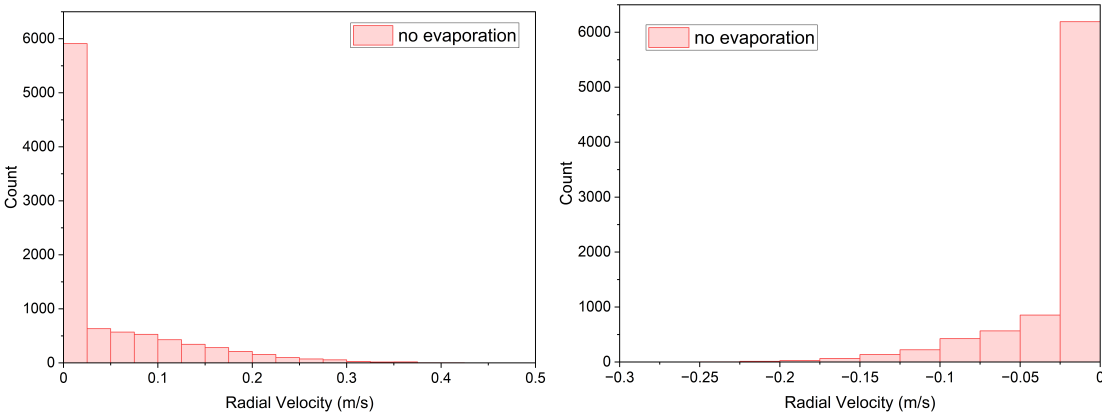

(a) Droplet with positive radial velocity (b) Droplet with negative radial velocity

Figure 3.25: Droplets radial velocity of case $T_w = 800K$ d_{p0}=0.1 mm without evaporation

Table 3.11 and Table 3.12 for a constant wall temperature of $T_w = 800$ K with varying initial droplet sizes, alongside comparison models shown in Table 3.10.

As shown in Table 3.11, under non-evaporating conditions, the net deposition mass flux $\dot{m}_{d,\text{net}}$ decreases significantly as the initial droplet diameter increases. This trend becomes less pronounced in the evaporating cases shown in Table 3.12. The data reveal that smaller droplets exhibit a higher net deposition mass flux. Specifically, $\dot{m}_{d,\text{net}}$ increases by nearly fivefold when the droplet size is reduced from 0.2 mm to 0.1 mm. However, when further reduced from 0.1 mm to 0.05 mm, the increase in deposition flux is smaller, indicating a diminishing return with decreasing size. Deposition velocity $k_{d,c\text{-}n}$ and entrainment velocity

Table 3.11: Droplet deposition parameters for $T_w = 800\,\text{K}$ without evaporation

	$\dot{m}_{d,\textbf{net}}$	$k_{d,c\text{-}n}$	$k_{d,n\text{-}c}$
	[kg/(m$^2\cdot$ s)]	[m/s]	[m/s]
$d_{p0} = 0.05$ mm	0.09497	0.06865	0.00272
$d_{p0} = 0.1$ mm	0.07600	0.04680	0.00351
$d_{p0} = 0.2$ mm	0.01691	0.02441	0.00812

Table 3.12: Droplet deposition parameters for $T_w = 800\,\text{K}$ with evaporation

	$\dot{m}_{d,\textbf{net}}$	$k_{d,c\text{-}n}$	$k_{d,n\text{-}c}$
	[kg/(m$^2\cdot$ s)]	[m/s]	[m/s]
$d_{p0} = 0.05$ mm	0.03481	0.04524	0.00267
$d_{p0} = 0.1$ mm	0.04842	0.04030	0.00721
$d_{p0} = 0.2$ mm	0.02685	0.02604	0.00925

$k_{d,n\text{-}c}$ characterize the lateral motion of droplets independent of their mass concentration. In the absence of evaporation, decreasing the droplet size approximately halves the deposition velocity. With evaporation, this size-dependent trend in deposition velocity becomes less significant. Conversely, the entrainment is enhanced in the evaporation condition. For

example, when increasing the size from 0.05 mm to 0.1 mm, the entrainment velocity under non-evaporating conditions increases slightly, whereas it increases by nearly threefold in the evaporating case. The comparisons in Table 3.11 and Table 3.12 suggest that smaller droplets favor higher deposition velocities but lower entrainment velocities. Evaporation reduces deposition velocity while enhancing entrainment velocity, highlighting the critical role of droplet size and phase change in deposition dynamics.

To prove the above conclusion, further simulations are conducted with two different wall temperatures (600 K, 1000 K) and $d_{p0} = 0.1$ mm. The three cases represent weak evaporation (600 K), medium evaporation (800 K), and strong evaporation (1000 K), respectively. Table 3.13 presents the total evaporation rate across the entire flow region for the three different wall temperatures, illustrating varying evaporation intensities. As the wall temperature increases, the total evaporation rate also rises. Specifically, increasing the wall temperature from 600 K to 800 K results in a threefold increase in the evaporation rate.

Table 3.13: Evaporation rate in flow region

	$T_w = 600$ K	$T_w = 800$ K	$T_w = 1000$ K
Total evaporation rate (kg/s)	0.001783	0.005371	0.006537

In Table 3.14, the deposition parameters under the three wall temperatures with evaporation are displayed. With the increase of wall temperature, the net deposition mass flux decreases. The deposition velocity also decreases while the entrainment velocity increases. It can be observed that higher evaporation rates lead to a lower deposition rate and a higher entrainment rate. At higher wall temperatures, droplets at the same position are smaller. Previous analysis has shown that smaller droplets typically have higher deposition velocity. However, despite high evaporation rates, these smaller droplets still demonstrate lower deposition velocity. This indicates that evaporation has a more pronounced inhibition effect on deposition. Table 3.15 gives the deposition parameters at three different

Table 3.14: Droplet deposition parameters for $d_{p0} = 0.1$ mm at different wall temperatures: with evaporation

	$\dot{m}_{d,\mathbf{net}}$ [kg/(m^2·s)]	$k_{d,c\text{-}n}$ [m/s]	$k_{d,n\text{-}c}$ [m/s]
$T_w = 600$ K	0.06083	0.04140	0.00356
$T_w = 800$ K	0.04842	0.04030	0.00721
$T_w = 1000$ K	0.03121	0.02664	0.01245

wall temperatures without evaporation. The results show that as the wall temperature increases, neither the deposition flux nor the deposition velocity exhibits significant change in cases without evaporation. Only the entrainment rate increases slightly with the rise in wall temperature, much less pronounced compared to the case with evaporation. When comparing the deposition velocities in both cases—with and without evaporation—it is clear that evaporation reduces the droplet deposition velocity while increasing the entrainment velocity. As the wall temperature rises, evaporation becomes more intense, leading to a stronger suppression effect on deposition velocity. In contrast, evaporation has a more significant effect on enhancing the entrainment velocity, even at lower wall superheating where evaporation is less significant. As evaporation intensity increases, the entrainment velocity of droplets rises by approximately 2 to 3 times compared to conditions without

Table 3.15: Droplet deposition parameters for $d_{p0} = 0.1$ mm at different wall temperatures: without evaporation

	$\dot{m}_{d,\mathbf{net}}$	$k_{d,c\text{-}n}$	$k_{d,n\text{-}c}$
	[kg/(m^2·s)]	[m/s]	[m/s]
$T_w = 600$ K	0.07045	0.04204	0.00296
$T_w = 800$ K	0.07600	0.04680	0.00351
$T_w = 1000$ K	0.05786	0.04014	0.00403

evaporation. This comparison clearly indicates that evaporation not only inhibits droplet deposition but also significantly enhances droplet movement toward the tube center. The more intense the evaporation, the more pronounced this effect on droplet deposition behavior.

Therefore, the droplet deposition model developed for unheated surfaces is not well suited for predicting droplet deposition in the PDO region. Correlations for droplet deposition that account for evaporation should be reconsidered.

3.5 Conclusion

In this chapter, the DPM in ANSYS Fluent is selected to simulate droplet behavior in the PDO region. Following model validation, a series of cases based on the experimental test section of Becker et al. (1983), with varying initial droplet sizes, are analyzed. The predicted wall temperature and interfacial velocity show good agreement with experimental data, confirming the reliability of the adopted modeling approach and underlying assumptions. Vapor temperature and velocity profiles are presented for scenarios both with and without droplets, revealing that the presence of droplets significantly influences the vapor temperature distribution. Droplet behavior—including droplet concentration distribution, evaporation, and deposition under various wall temperatures—is thoroughly investigated and analyzed. The main findings and conclusions are summarized as follows:

- With uniform droplet injection at the inlet, a W-shaped distribution of droplet mass concentration forms along the flow direction. Droplets are more densely distributed in both the tube center and the near-wall region. Moreover, droplets in the near-wall region are smaller and have a larger velocity difference relative to the local vapor phase. The smaller droplet size near the wall results from the higher evaporation rate. The radial distribution of velocity and interfacial velocity difference under different initial droplet sizes agrees well with experimental observations (Lee and Almenas, 1982).
- Comparison of droplet evaporation rates on the wall and in the mainstream indicates that direct contact heat transfer between droplets and the wall is negligibly small compared to droplet evaporation within the entire flow channel. However, droplet evaporation in the near-wall region—which accounts for about 25% of the cross-sectional area—contributes to more than half of the total droplet evaporation. Smaller droplets lead to higher evaporation rates, lower vapor temperatures, and lower wall temperatures. This emphasizes the importance of accurately capturing interfacial heat transfer to predict PDO heat transfer.
- To analyze droplet deposition behavior from the CFD results, individual droplet radial velocity distributions and overall lateral movement are examined in detail.

The distribution of droplet radial velocities shows that droplets moving toward the wall follow a normal distribution along the positive semi-axis. Comparison across cases with different droplet sizes reveals that smaller droplets exhibit higher average radial velocities toward the wall, indicating that droplet lateral movement is highly sensitive to droplet size. The droplet deposition model in the PDO region should account for droplet size effects.

- Examination of cases with and without evaporation indicates that the number of droplets with low radial velocities toward the wall is significantly reduced when evaporation is present, whereas the number of droplets with low radial velocities toward the tube center increases. By halting droplets with small positive radial velocities, evaporation reduces the overall droplet deposition mass flux from the central region to the near-wall region.
- Evaporation in the near-wall region tends to inhibit droplet movement toward the wall while promoting their return to the main flow. The higher the wall temperature or the greater the evaporation intensity, the more pronounced the effect of inhibiting deposition and promoting entrainment. This indicates that droplet lateral movement is significantly influenced by evaporation, especially under high evaporation intensity. Consequently, deposition correlations derived from unheated walls are inapplicable to PDO regions, highlighting the need for a new deposition model tailored to conditions with droplet evaporation.

4. Experimental Investigation on Droplet Behaviors in PDO Region

The numerical simulation results indicate that droplet size plays a crucial role in heat transfer efficiency, directly influencing the wall temperature distribution in the PDO region. However, existing experimental data on droplet behavior in the PDO region remain limited, which constrains the accuracy of droplet-related models. To bridge this gap, this study conducts a visualized experimental investigation to analyze droplet dynamics in the PDO region. In this chapter, the experimental setup, methodology, and measurement techniques are introduced in detail. Followed by a presentation and analysis of the results, the statistical analysis of droplet parameters, including size distribution, velocity distribution and spatial position, provides profound insights into droplet movement and dynamics in PDO region. The experimentally obtained droplet parameters are further used to evaluate and refine existing empirical correlations for average droplet size and velocity. These findings contribute to improving droplet size model and thus enhancing the prediction of heat transfer in the PDO region.

4.1 Experimental Setup

4.1.1 Experimental Loop

The experimental apparatus KIMOF was designed and constructed to study thermal hydraulics of two phase flow (Köckert et al., 2018; Rensch et al., 2024). The system is a closed-loop facility, as shown in Figure 4.1, ensuring controlled experimental conditions. R-134a is selected as the working fluid due to its relatively low operating temperature and latent heat. The major components of the experimental setup include pressurizer, main pump, preheater, electric flow heater, secondary cooling system, process valve, and test section. The pressurizer maintains the system pressure at the desired level, ensuring stable operating conditions. The main pump circulates the R-134a within the closed loop, where the fluid is initially heated by either the preheater or the electric flow heater to achieve the desired inlet temperature before entering the test section. The process valve allows fine control of the mass flow rate, measured by the Coriolis flowmeter before entering the test section, ensuring precise adjustment of experimental parameters. Within the test section, the fluid is further heated by the heating tube to reach dryout and PDO conditions.

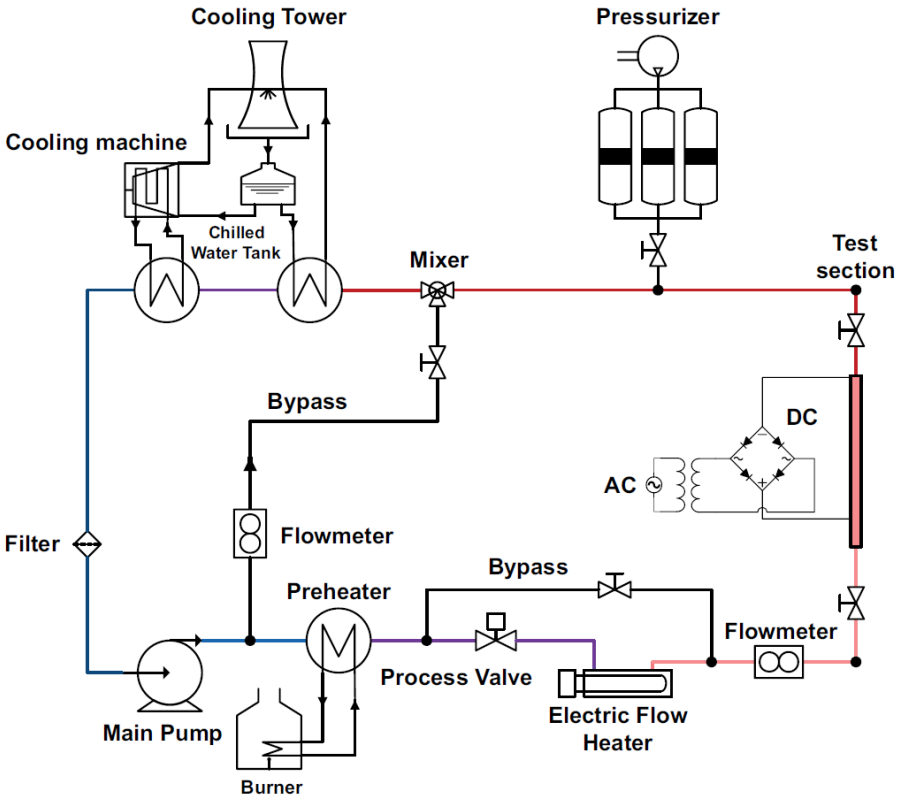

Figure 4.1: Schematic set-up of the KIMOF (Köckert et al., 2018)

4.1.2 Test Section

As shown in Figure 4.2, the test section is more than 3 m long in total. It consists 3 square flow channels and one heating tube in the center. Each square channel is around 1 m long. One piece of square channel contains 16 optical windows on parallel sides, enabling direct observation of the flow conditions inside the channel. The three square flow channels are connected with flanges, ensuring both a secure connection and precise alignment. The heating tube is positioned inside the square channel using 10 spacers to ensure proper alignment and to avoid contact between the heating tube and the inside channel wall. The Figure 4.3 displays the cross-sectional view of the test section. The heating tube in the middle has an outer diameter of 10 mm, while the square channel has an inner width of 14 mm. The blue region in Figure 4.3 is the flow area of the working fluid. To monitor the thermal conditions within the test section, in total 20 thermocouples are installed along the inner side of the heating tube at 12 levels, as shown with the orange circles in Figure 4.3. The glass windows allow the high-speed camera to capture detailed droplet dynamics under PDO conditions.

The test section is heated with a direct current (DC) supplied by a transformer. The temperature and pressure of the fluid at both the inlet and outlet of the test section are measured using a mineral-insulated type-T thermocouple and a pressure transmitter, respectively. The system pressure is controlled by the pressurizer to maintain the average pressure of the inlet and outlet pressure of the test section to a desired value. To ensure a fully developed flow at the beginning of the heated section, the distance between the inlet and the bottom current connector is set to approximately 430 mm. To minimize heat loss, the test section is insulated with two protective layers, maintaining stable thermal conditions within the test section.

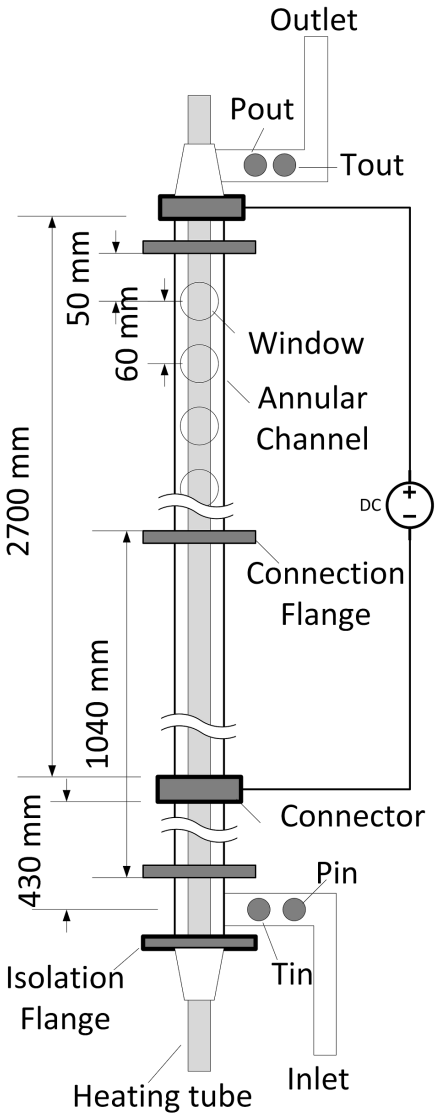

Figure 4.2: Schematic of test section

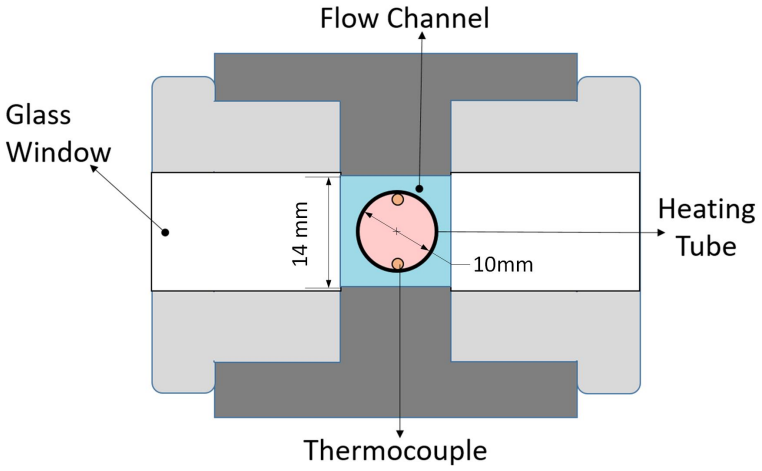

Figure 4.3: Cross-sectional view of the test section

4.1.3 Optical Instruments

A high-speed imaging system is utilized to capture droplet behavior with high temporal and spatial resolution. As shown in Figure 4.4, the measurement setup comprises an LED backlight that provides uniform illumination through the transparent glass windows. The high-speed camera, positioned directly opposite the light source, recorded the droplets flowing inside the channel. Optronis high-speed video camera plus sigma macro lens are installed together to record the droplet behaviors. The sensor operates at a resolution of 1920 × 1080 pixels. A framerate of 2487 fps is used during the experiment. It is configured to capture one image around every 0.4 micro seconds. The lighting system includes one white LED light with 12000 lumens. A glass plate is attached to the outer surface of the window on the light side. The pane of glass is Plexiglas GS white WH010 with a thickness of 3 mm, which minimizes the effect of the individual LED light sources per panel through appropriate light refraction and have more uniform light going inside the channel and camera.

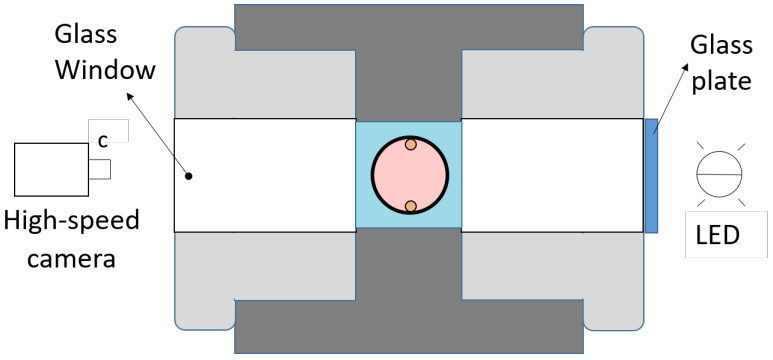

Figure 4.4: Schematic of the arrangement of optical instruments

4.2 Experimental Matrix

To investigate the effects of key thermal-hydraulic parameters on droplet behavior in the PDO region, a series of experiments are conducted under varying conditions of pressure, heat flux, and mass flux. The experimental matrix is shown in Table 4.1. The selection of these test conditions allows for the evaluation of multiple influencing factors:

- **Pressure:** The system pressure ranges from 16.2 bar to 32.5 bar, corresponding to a reduced pressure from 0.4 to 0.8. This range covers and slightly exceeds the typical operating pressures of BWRs and PWRs, as well as the pressure range encountered in some industrial heat exchangers. This broad pressure range allows for a comprehensive investigation of pressure effects on droplet behaviour.
- **Heat Flux:** The applied heat flux ranges from 20 kW/m^2 to 40 kW/m^2, enabling the investigation of thermal effects on droplet size and velocity. Within this range, a dispersed flow regime is established in the region of interest. If the heat flux is too low, excessive liquid presence can obstruct the optical window, while an overly high heat flux can lead to very high steam quality, causing droplets to become barely visible or completely evaporated.
- **Mass Flux:** Two mass flux levels, 100 kg/(m^2·s) and 150 kg/(m^2·s), are selected to investigate the influence of mass flow rate on droplet behavior. Higher mass fluxes are avoided due to limitations of the test facility: excessive liquid volume fraction at higher flow rates tends to cover the observation window, making it difficult to visualize and track droplet motion within the channel.

Table 4.1: Experiment Parameters

Case No.	Pressure (bar)	Heat Flux (kW/m^2)	T_{in} (°C)	Mass Flux (kg/(m^2·s))
1	16.2	25.0	25.18	100
2	20.3	24.0	43.14	100
3	20.3	27.0	37.74	100
4	20.3	30.0	55.37	100
5	20.3	35.0	55.02	150
6	20.3	37.5	54.91	150
7	20.3	40.0	49.39	150
8	28.4	22.5	64.67	100
9	32.5	20.0	68.60	100

4.3 Experimental Operation

4.3.1 Measurement Procedure

Each single PDO experiment is carried out at constant inlet temperature, mass flux, and pressure as steady-state experiments. This systematic approach ensures that droplet behaviors are captured under well-defined thermal-hydraulic conditions, providing high-quality experimental data for model validation and refinement. The procedures of visualized PDO experiments are shown below:

- **Pressure increase:** Increase the system pressure to the desired value.
- **Preheating and system stabilization:** The flow before the inlet is preheated to the desired inlet temperature as the system parameters are stabilized to the desired mass flux.
- **Incremental heat power:** The heat power of the heating tube is gradually increased until the topmost thermocouple in the test section detects a sudden temperature jump, indicating the occurrence of dryout.
- **Observation of droplet behaviors:** Heat flux continues to be increased until the droplets in the topmost optical window become clearly visible.
- **High-speed imaging:** The droplets inside the flow channel are recorded by the high-speed camera across the transparent window, capturing key characteristics such as droplet size, position, and velocity.

4.3.2 Droplet Measurements

The high speed camera records the flow conditions and droplet behaviors in the PDO region. By analyzing the image sequences, the motion of droplets can be well tracked and analyzed, providing valuable insights into droplet parameters and behaviors in PDO conditions. Figure 4.5 presents a sample of image acquired during the experiment. In the image, the central black region corresponds to the heating tube, while the grey areas on both sides are the illuminated region inside the flow channel. The droplets appear as scattered dark spots within the illuminated region, where their movement are recorded into a sequence of images as Figure 4.5.

As observed in Figure 4.5, the left half of the flow channel provides a clear view of the droplet distribution. Therefore, the left side under different heat fluxes are displayed together in Figure 4.6 to show the change of droplet size and number as the heat flux increases. With the same mass flux and pressure conditions, an increase in heating flux results in fewer remaining droplets within the flow channel. Additionally, the size of the droplets decreases as the heating flux increases.

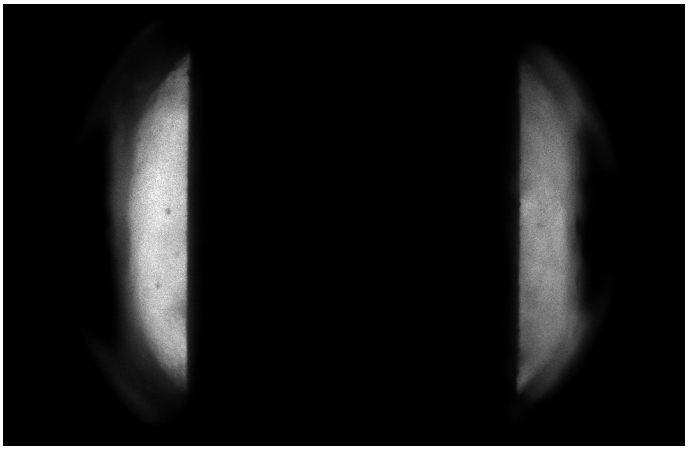

Figure 4.5: Original image captured by high-speed camera

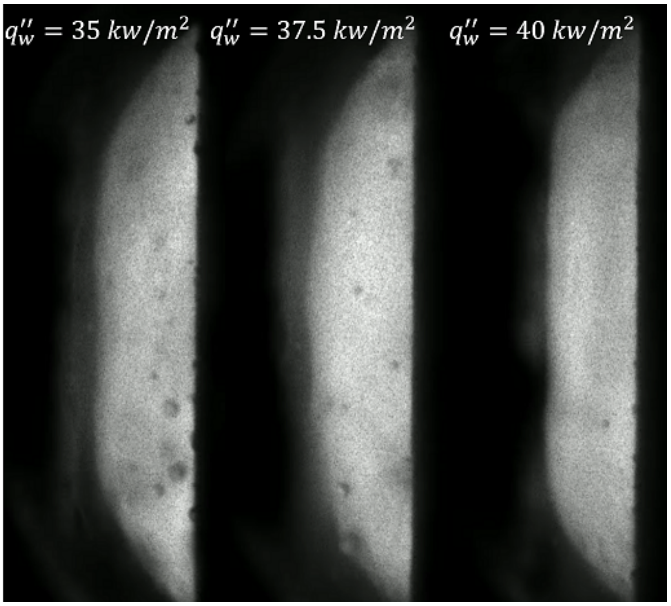

Figure 4.6: Original image of the left side of the flow channel under increasing heat fluxes

Once the image sequences of the flow channel at consecutive moments are obtained, as shown in Figure 4.7, key droplet characteristics, including droplet size, velocity, and position, can be extracted through image post-processing. These parameters are crucial for understanding droplet dynamics in the PDO region.

4.3.3 Uncertainties

In this paper, the target parameters from the experimental work are droplet size and droplet velocity. For the further analysis of droplet size and velocity, the related parameters of operation conditions are mass flux, heat flux and pressure. The mass flux, heat flux

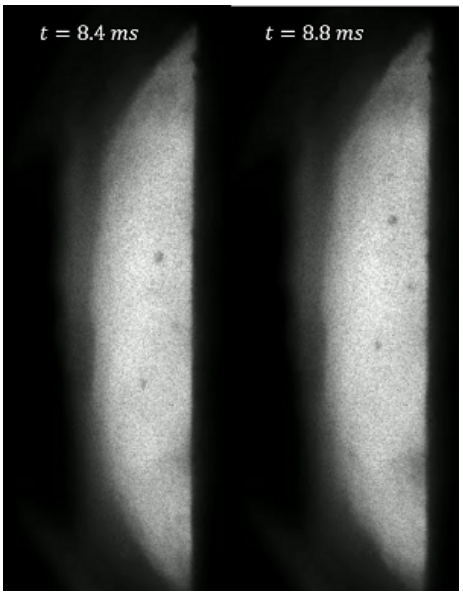

Figure 4.7: Original images of the left side of the flow channel at adjacent time instants

and pressure are measured from measurement facilities, which has certain measurement uncertainties. The droplet size is directly extract from images post-processing, which has certain uncertainties during the post processing. The droplet velocity is derived by the position difference between two time steps. Therefore, the parameters uncertainties are summarized in the Table 4.2. Among them, the uncertainties occurred during the images post-processing are only be approximately estimated. The uncertainties in droplet size and position measurements are approximately ±0.01 mm, primarily due to pixel resolution limits and image binarization thresholds. It is also noted that droplets smaller than 0.04 mm cannot be reliably captured with the current optical setup. The resolution limit of droplet detection introduces a bias in the statistical analysis of cases with smaller droplets.

Table 4.2: Measurement Uncertainties of Key Parameters

Parameter	**Mean Error (ME)**
Pressure	0.14%
Mass Flux	2.62%
Heat Flux	2.41%
Equilibrium Steam Quality	4.41%
Droplet Size	6.47%
Droplet Velocity	2.72%

The experiments were repeated after approximately two months to check the reproducibility of the obtained data. In total, 31 PDO experiments were randomly selected and repeated. Overall, the test runs showed that the experiments can be reproduced well. The droplet size and velocity ranges from the repeating experiments are almost the same.

4.4 Experimental Results

The case number 5 in Table 4.1, with a pressure of 20.3 bar, mass flux of 150 kg/(m^2·s), and heat flux of 35 kW/m^2, is taken as an example to analyze the obtained droplet parameters

in detail.

Figure 4.8 presents the histogram of droplet size distribution, illustrating the number of droplets corresponding to different size ranges. From the statistical analysis, it is observed that most droplets fall within the size range of 0.15 mm to 0.2 mm. The number of droplets with larger or smaller sizes decreases. The minimum droplet size in this case is 0.06 mm, and the maximum recorded droplet size is 0.5 mm. Additionally, 90% of the droplets fall within the range of 0.1 mm to 0.3 mm, among which 70% are between 0.15 mm and 0.25 mm.

Figure 4.9 shows the fitting of the droplet size distribution, indicating that the distribution follows both a gamma distribution and a lognormal distribution, which aligns well with previous experimental findings of Tatterson et al. (1977),Ueda and Kim (1982), and Cumo et al. (1974). This consistency validates the effectiveness of the experimental methodology and confirms the reliability of the measurement techniques used in this study.

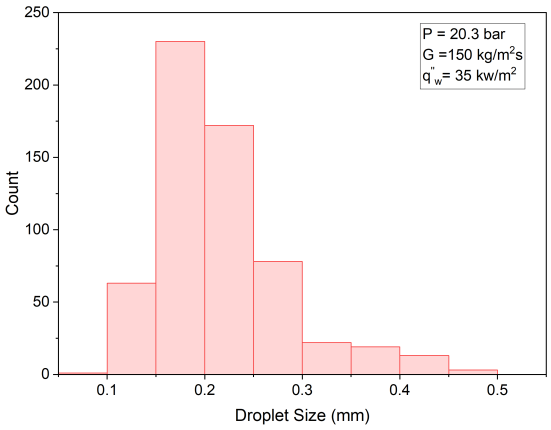

Figure 4.8: Histogram of droplet size distribution

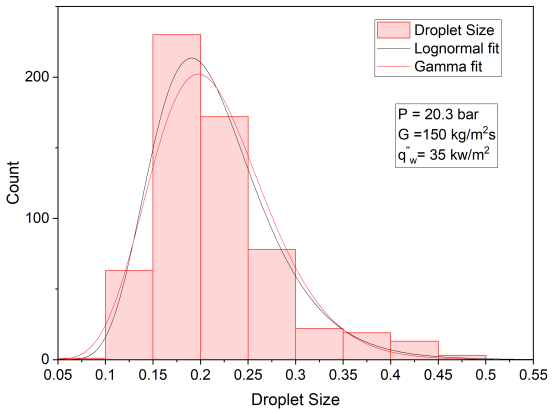

Figure 4.9: Droplet size distribution with Lognormal and Gamma Fits

Through the further analysis on the droplet size, the arithmetic mean diameter d_{10}, surface mean diameter d_{20}, volume mean diameter d_{30}, and sauter mean diameter d_{32} are calculated according to Equation (4.1)-(4.4) and displayed in Table 4.3. The surface mean diameter is crucial for determining the interfacial heat transfer area, while the d_{30} is important for estimating the droplet volume fraction. The d_{32} is particularly relevant when considering the active surface area, as it is typically larger than the arithmetic mean diameter. This difference in d_{32} and d_{10} is dependent on the droplet size distribution. In the work of Ueda and Kim (1982), the measured d_{32} is 1.57 times the measured d_{10}. In the present study, the difference between measured d_{32} and measured d_{10} is smaller. In the work of Cumo et al. Cumo et al. (1974), the d_{10} is expected to be 2 times the d_*, the most probable diameter from the droplet distribution, but it is only 1.07 times in the present work as shown in Table 4.3. This smaller difference between the characteristic sizes may be attributed to the limitation of the minimum droplet size observed in this experiment.

$$d_{10} = \frac{\sum_{i=0}^{n} d_i}{n} \tag{4.1}$$

$$d_{20} = \sqrt{\frac{\sum_{i=0}^{n} d_i^2}{n}} \tag{4.2}$$

$$d_{30} = \sqrt[3]{\frac{\sum_{i=0}^{n} d_i^3}{n}} \tag{4.3}$$

$$d_{32} = \frac{\sum_{i=0}^{n} d_i^3}{\sum_{i=0}^{n} d_i^2} \tag{4.4}$$

Table 4.3: Droplet mean diameter for Case 5

d_{32} [mm]	d_{30} [mm]	d_{20} [mm]	d_{10} [mm]	d_* [mm]
0.259	0.236	0.225	0.215	0.201

Besides droplet size, droplet velocity also plays a crucial role in the interfacial heat transfer. The distribution of the axial and radial droplet velocities are presented in Figure 4.10(a) and Figure 4.10(b), respectively. As shown in Figure 4.10(a), the axial velocity distribution exhibits a shifted normal profile, with data symmetrically distributed around the central value. A distinct peak appears in the range of 1.5–1.6 m/s, corresponding to the highest probability, while the distribution gradually tapers off on both sides. In Figure 4.10(b), the radial velocity exhibits a close standard normal distribution, but with a higher peak and shorter tail, suggesting that extreme radial velocities are less probable. The negative radial velocity indicates droplets moving away from the heated wall, whereas the positive radial velocity represents droplets moving toward the heated wall. The results show that nearly half of the droplets fall within two adjacent bins centered around zero velocity, showing that most droplets have a very small radial velocity.

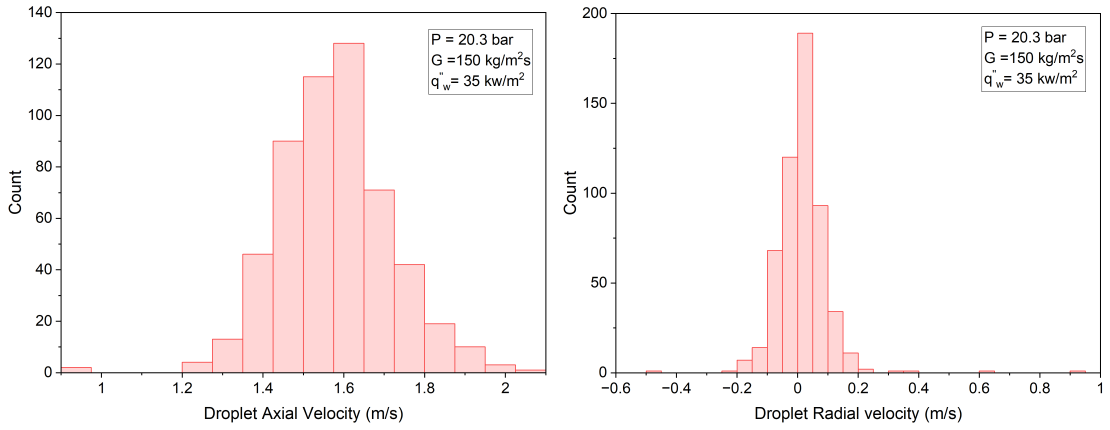

(a) Droplet axial velocity (b) Droplet radial velocity

Figure 4.10: Histograms of droplet axial and radial velocities

From the CFD simulations in Chapter 3, it has been observed that the radial position of droplets significantly influences the droplet evaporation rate. Figure 4.11 presents the radial distance of droplets from the wall, illustrating the number of droplets within each distance interval. It shows that the fewest droplets are found at the farthest distance from the wall. As the distance decreases, the droplet count gradually increases, reaching a peak. However, within 0.2 mm from the wall, the number of droplets drops sharply. This distribution closely resembles the droplet concentration profile obtained from CFD simulations in Chapter 3: due to lateral droplet transport, the droplet concentration increases progressively as droplets move closer to the wall. However, near the wall, intense evaporation caused by high vapor temperature leads to a decrease in droplet concentration. Furthermore, droplet tracking reveals that droplet-wall collisions and rebounds are observed only in rare cases. The majority of droplets primarily move axially within the vapor flow, with only minor radial displacement.

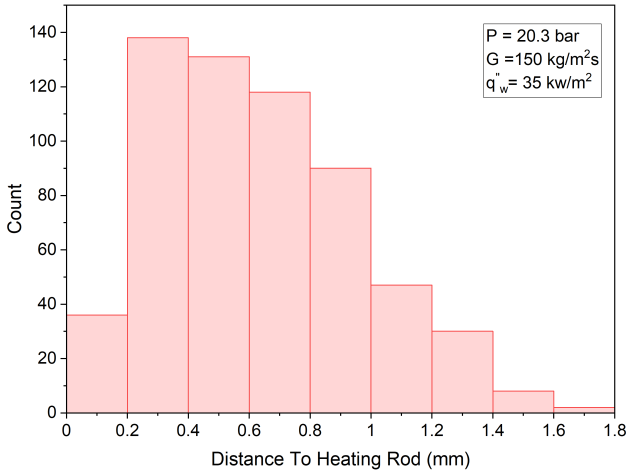

Figure 4.11: Distribution of droplets' distance from the heating tube

4.4.1 Analysis on Droplet Size

4.4.1.1 Statistical Analysis

Figure 4.12 presents the droplet size distribution under different heat flux conditions. It can be observed that as heating power increases, the overall distribution follows the same trend, shifting toward smaller sizes, indicating that more droplets become smaller while fewer droplets remain large. It can also be seen that as the heating power increases, the number of droplets that can be collected becomes less, which is consistent with the trend observed in Figure 4.6. The significant reduction in the number of droplets is primarily attributed to the increase in local steam quality caused by higher heating power. Under the same pressure and mass flux conditions, a higher heat flux results in a larger amount of liquid being converted into vapor before reaching the observation window. Specifically, as the heat flux increases from 35 to 40 kW/m², the equilibrium steam quality at the observation location rises from 1.23 to 1.43. Consequently, a greater portion of the droplets evaporates all their mass upstream, leading to a marked decrease in the number of droplets present in the observed region. Moreover, for relatively large droplets, the intensified heating over the same axial length promotes more evaporation, resulting in significantly smaller droplet sizes at the observation point.

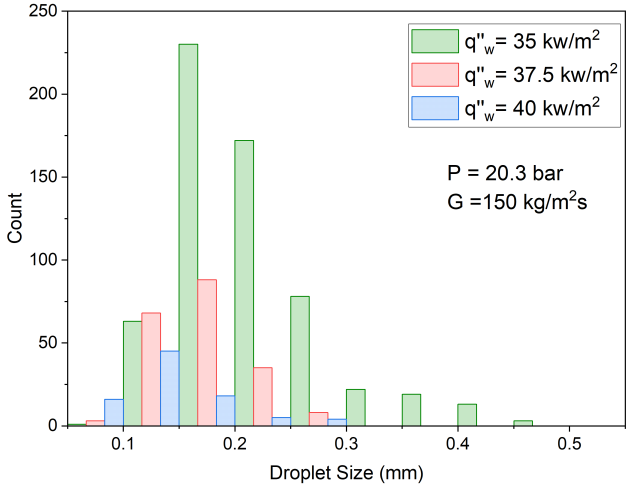

Figure 4.12: Droplet size distribution under different heat fluxes

Figure 4.13 presents droplet size distributions at three different pressures, with reduced

pressures P_R of 0.4, 0.5, and 0.8, respectively. The results indicate that as pressure increases, the droplet size distribution shifts to smaller values, and the most probable droplet size gradually decreases. This trend suggests that higher pressures lead to smaller droplet sizes, which could be attributed to the smaller surface tension of liquid at higher pressure. Additionally, at a low pressure of 0.4, the droplet size distribution follows well a gamma distribution. As the pressure increases, the peak and the curve gradually shift to the left, the left tail of the distribution curve gradually becomes invisible. At a higher pressure of 0.8, the most probable droplet size even falls within the minimum observable size range (0.04-0.09 mm). This is because this experiment cannot capture droplets smaller than 0.04 mm. Given that the droplet size follows a gamma distribution, it is likely that droplets smaller than 0.04 mm exist but are not accounted for in the measurements at higher pressures. As a result, the proportion of uncounted droplets increases with pressure, indicating that actual droplet sizes at higher pressures are smaller than the measured values. This highlights the significant influence of pressure on droplet size in the PDO region.

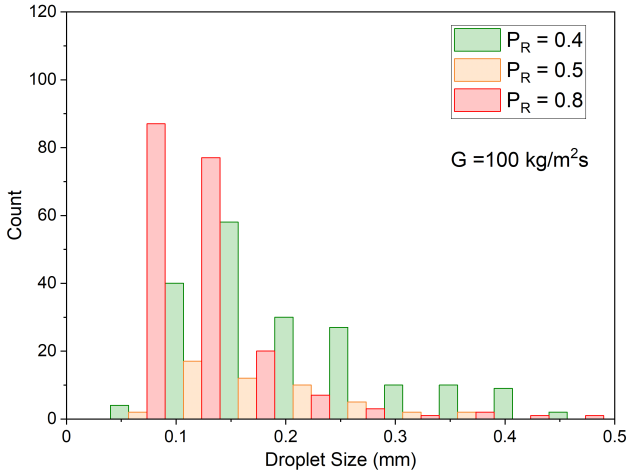

Figure 4.13: Droplet size distribution under different pressures

Figure 4.14 shows the histograms of droplet size distributions under different mass flux conditions. The cases with flow rates of 100 kg/(m²·s) and 150 kg/(m²·s) have relatively close equilibrium steam qualities: 1.33 and 1.26, respectively. It is evident that at higher mass

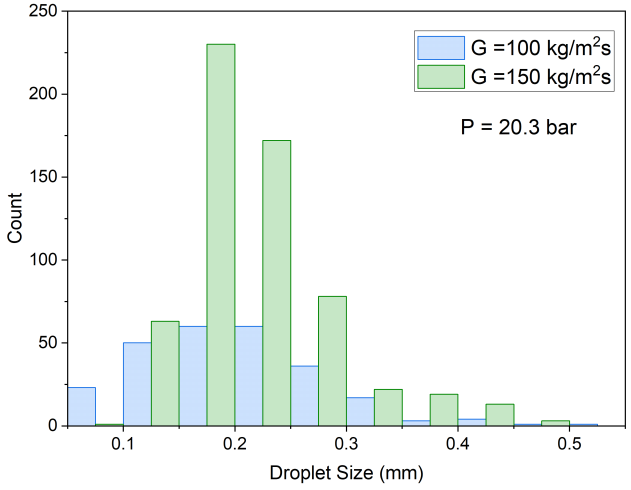

Figure 4.14: Droplet size distribution under different mass fluxes

flux, significantly more droplets are collected. While the overall size distribution and range remain similar for both mass flux conditions, the distribution at higher mass flux is notice-

ably steeper, with a sharper peak. This indicates that the proportion of small droplets is lower, and the droplet sizes are more concentrated around the most probable value. It can be attributed to the smaller wall temperature under higher mass flux—approximately 30 K lower. This leads to smaller vapor superheating and thus lower evaporation efficiency, allowing droplets to retain slightly larger sizes. However, the increased vapor velocity at higher flow rates enhances aerodynamic shear, which limits droplet maximum size. As a result, the maximum droplet size under higher mass flux does not increase significantly, despite the reduced evaporation.

4.4.1.2 Average Size Analysis

After statistical analysis of the droplet size, the measured average droplet size d_{10} is obtained for further quantitative analysis. First, the d_{10} is plotted against the thermal equilibrium steam quality x_e to observe the relation between d_{10} and x_e. As shown in Figure 4.15(a), a total of 9 cases from Table 4.1 are shown, covering different pressures and mass fluxes, indicated with different colors. Cases with the same pressure and mass flux share the same color and are fitted with rough trend curves. As shown in the figure, the red and green lines depict the variation of droplet size with x_e at reduced pressure of 0.5, with mass fluxes of 100 kg/(m²·s) and 150 kg/(m²·s), respectively. The curves indicate a negative slope between d_{10} and x_e. As x_e increases, the average droplet size decreases due to the droplets evaporation in superheated vapor. This trend can be approximated using either a linear or an exponential fit.

On the other hand, it can be seen that under different mass fluxes, the decrease rate in droplet size as x_e increases is also different. At higher flow rates, the droplet size decreases more rapidly with increasing x_e. In region with smaller steam quality, the average droplet size is larger at higher flow rates, whereas in higher steam quality regions, the average droplet size is larger at lower flow rates. Similar trends can also be found in Cumo et al. (1974).

Since Cumo only operated experiments under constant mass flux, Figure 4.15(b) plots Cumo's measured average droplet size and the corresponding equilibrium quality under different pressures. It can be seen that the average droplet size decreases as x_e increases, indicating a similar trend to that captured in the current experimental work.

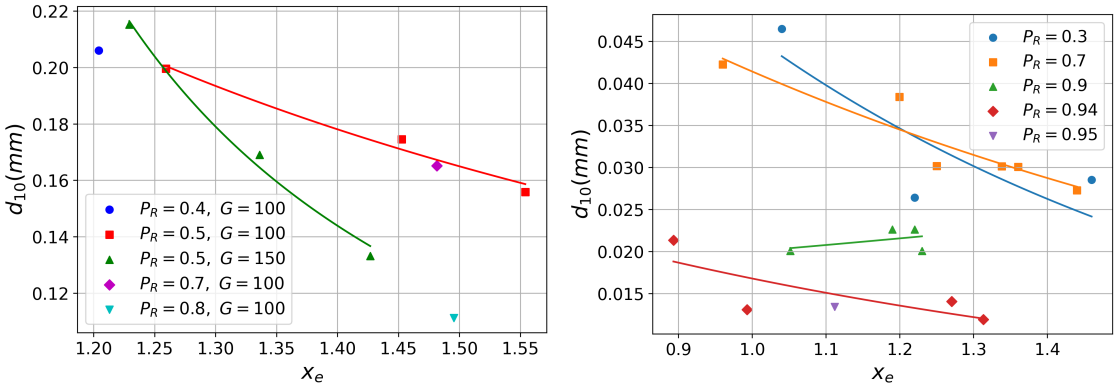

(a) With KIMOF experimental data

(b) With Cumo experimental data

Figure 4.15: Droplet mean size vs. Equilibrium steam quality

Figure 4.16(a) illustrates the variation in average droplet size for four cases with similar x_e and mass flux but different reduced pressures P_R. The black points represent experimentally measured average droplet size, while the blue line provides a rough fitting curve to highlight the trend of the droplet size variation with pressure. The results indicate

a clear trend: as pressure increases, droplet size decreases, with the reduction becoming more pronounced in the high-pressure region. A similar trend is also observed in Cumo et al. (1972). As shown in Figure 4.16(b), the measured d_{10} from Cumo exhibits a rela-

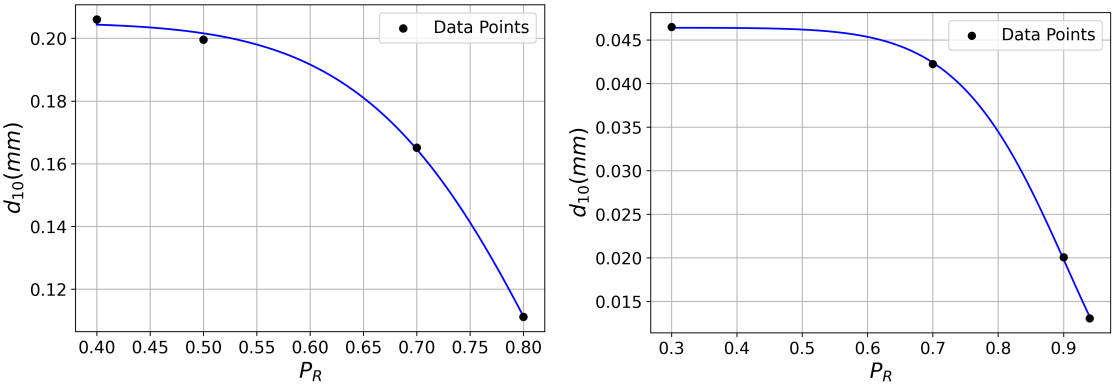

(a) With KIMOF experimental data

(b) With Cumo experimental data

Figure 4.16: Droplet mean size vs. reduced pressure

tively gradual decrease with increasing P_R in the low-pressure range. As P_R exceeds 0.7, the droplet size decreases at a significantly faster rate. The variation in droplet size with pressure can be analyzed based on the droplet formation mechanism in dispersed flow. As pressure increases, substantial changes occur in fluid properties, including reduced surface tension, a smaller density difference between phases, and lower latent heat of vaporization. The reduction in surface tension tends to produce smaller droplets, whereas the decreased density difference between phases favors larger droplets. Additionally, lower latent heat enhances droplet evaporation, further reducing droplet size. The combined effect of these factors ultimately leads to a decreasing trend in droplet size with increasing pressure. The sharp decline in droplet size at very high pressures can be attributed to the drastic changes in both surface tension and latent heat.

4.4.2 Analysis on Droplet Velocity

4.4.2.1 Statistical Analysis

By comparing the droplet velocity distributions under the same mass flux and pressure, the effect of heat flux on droplet velocity is clearly observed in Figure 4.17. In Figure 4.17(a), as the heat flux increases, the range of droplet axial velocity expands slightly, and the overall distribution shifts rightwards, indicating a general increase in velocities of droplets. Additionally, the peak position of the distribution moves to the right, suggesting a higher most probable velocity of the droplets. This increase in droplet velocity can be attributed to the increase in steam quality with higher heat flux. When the heat flux rises from 35 to 40 kW/m^2, the equilibrium steam quality x_e increases from 1.23 to 1.43. As more droplets evaporate and transit into vapor, the mass flow rate of the vapor phase increases. Furthermore, higher vapor superheating reduces vapor density, leading to an increase in vapor velocity. The enhanced vapor velocity, in turn, increases the droplet velocity due to the effect of drag force.

Figure 4.17(b) presents the droplet radial velocities under different heat fluxes. Despite variations in droplet count, the velocity distributions exhibit similar patterns across cases, with peaks concentrated around zero and symmetrically decreasing toward both sides, closely resembling a normal distribution. Most droplets have velocities smaller than 0.1 m/s. At the lowest heat flux, 7 droplets exhibit significantly higher radial velocities,

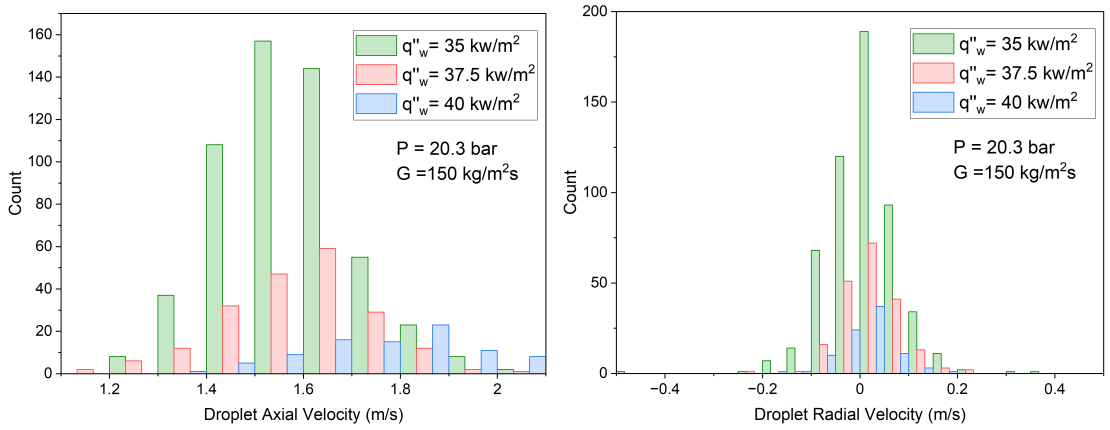

(a) Droplet axial velocity (b) Droplet radial velocity

Figure 4.17: Distribution of droplet axial and radial velocities under different heat fluxes

accounting for 1.2% of the total. Additionally, 10% of the droplets have velocities ranging from 0.1 m/s to 0.2 m/s. These results indicate that in the PDO region, most droplets maintain low radial velocities, with only a small fraction exceeding 10% of corresponding axial velocity. This trend aligns well with the CFD results presented in Chapter 3.

Figure 4.18 present comparisons of droplet axial and radial velocity distributions under different pressures. A significant shift in the axial velocity distribution is observed in Figure 4.18(a) as pressure changes. When the reduced pressure P_R increases from 0.4 to 0.8, the entire velocity profile shifts from the range of (0.8, 1.8) m/s to (0.2, 1.2) m/s. Additionally, the peak of the droplet axial velocity distribution profile decreases from about 1.2 m/s to 0.7 m/s. This trend indicates that higher pressure results in lower droplet axial velocity. Compared to the effect of heat flux in Figure 4.17, pressure has a more pronounced influence on droplet velocity. This is attributed to the substantial changes in vapor properties with increasing pressure, which lead to significant variations in vapor velocity, e.g. increase in vapor density. Since droplet velocity is primarily driven by the drag force exerted by the interfacial velocity difference, the reduction in vapor velocity at higher pressure directly contributes to the observed decrease in droplet velocity. Figure 4.18(b) presents the histograms of droplet radial velocities under different pressure conditions. The distributions exhibit a centrally symmetric normal distribution, with most droplets having relatively velocities close to zero. Additionally, the maximum radial velocity that droplets can attain remains similar across different pressure conditions.

Besides pressure, mass flux also has a significant impact on droplet velocity distribution. To examine this effect, two working conditions with similar x_e and the same pressure are selected for comparison. The results in Figure 4.19(a) show that as the mass flux increases from 100 kg/(m^2·s) to 150 kg/(m^2·s) at the reduced pressure of 0.5, the droplet velocity distribution shifts noticeably in the positive direction along the x-axis. The velocity range expands from 0.6-1.3 m/s to 1.2-2.2 m/s. However, it can also be seen that the peak velocity of the distribution curve rises approximately from 0.95 m/s to 1.5 m/s, showing a proportional increase as the mass flux increases. An analysis of the average droplet velocity also reveals that the average droplet velocity increases from 0.98 m/s to 1.58 m/s. This proportional increase suggests that the rise in droplet velocity is primarily driven by the higher vapor velocity under elevated mass flux conditions.

Figure 4.19(b) shows the histograms of droplet radial velocities under these two mass flux conditions. Both distributions exhibit a normal distribution shape, with most droplets concentrated close to zero velocities. Compared to the effects of pressure and heat flux,

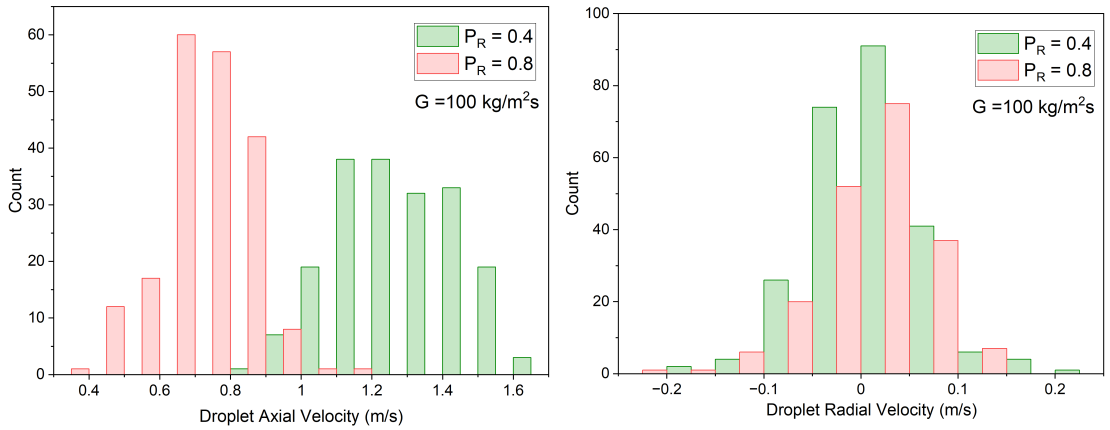

(a) Droplet axial velocity (b) Droplet radial velocity

Figure 4.18: Distribution of droplet axial and radial velocities under different pressure

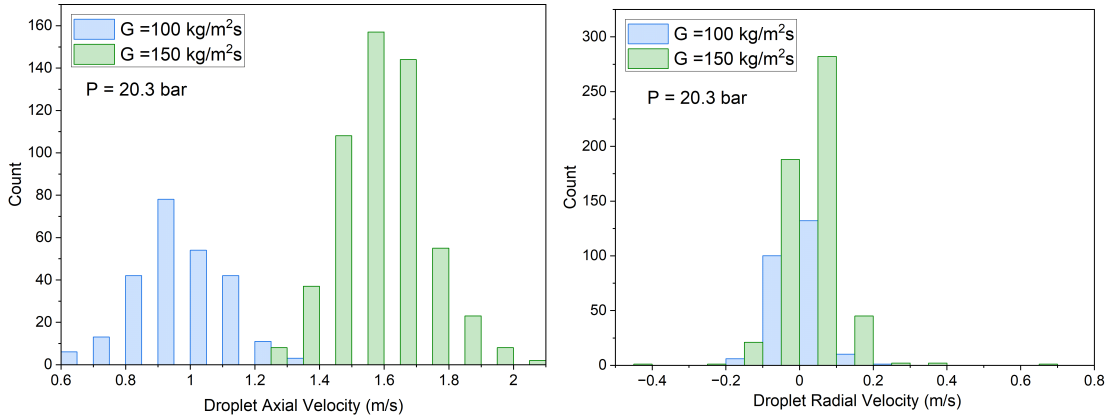

(a) Droplet axial velocity (b) Droplet radial velocity

Figure 4.19: Distribution of droplet axial and radial velocities under different mass fluxes

the influence of mass flux on droplet radial velocity is more pronounced. At higher mass flux, the peak of the velocity distribution shifts toward the position direction of x-axis. Additionally, the velocity distribution becomes broader, with a few droplets reaching higher velocities. This suggests that increasing mass flux significantly enhances the radial momentum of droplets, leading to an increases in droplet radial velocity. Despite these differences, the overall trend remains consistent: most droplets have small radial velocities, and only a small fraction exceeds around 10% of their corresponding axial velocities. This indicates that while mass flux strongly influences the maximum radial velocity, the fundamental shape of the distribution remains unchanged

4.4.2.2 Average Droplet Axial Velocity

By averaging the axial velocities of droplets, the variation of average droplet axial velocity with pressure at constant mass flux and similar steam quality is displayed in Figure 4.20(a). The variation of average droplet axial velocity with equilibrium steam quality x_e under constant mass flux and pressure is displayed in Figure 4.20(b). It is found that the change trend of droplet velocity with pressure and heat flux aligns well with the statistical analysis. Droplet velocity generally decreases as pressure increases, while a higher mass flux leads to greater vapor and droplet velocities. Additionally, an increase in x_e enhances vapor velocity, which in turn raises droplet velocity. But this effect is less significant compared

to the influence of pressure and mass flux.

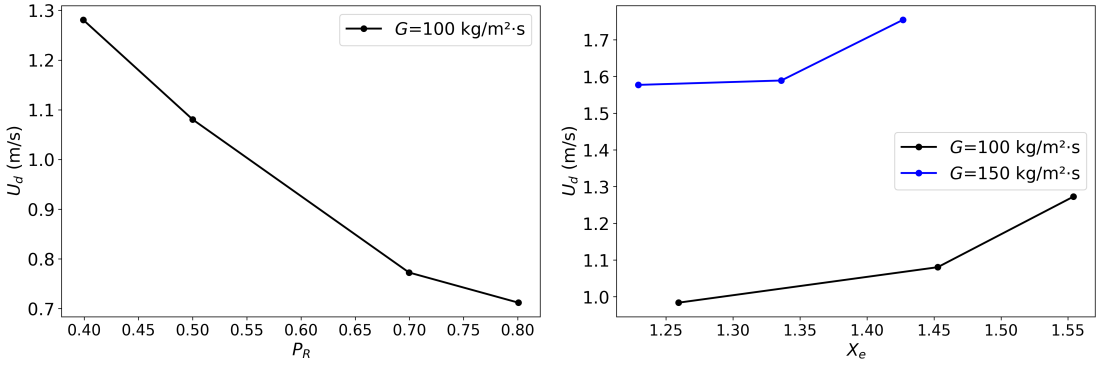

(a) Average droplet axial velocity vs. P_R (b) Average droplet axial velocity vs. x_e

Figure 4.20: Average droplet axial velocity with KIMOF experimental data

4.5 Assessment and Improvement of Droplet Size and Velocity Correlations

Numerous empirical correlations have been proposed for predicting droplet size and velocity in PDO conditions, derived either from theoretical analyses or experimental data fitting. In this subsection, the obtained average droplet size and velocity data from current work are utilized to assess the reliability of these existing correlations. Where discrepancies are identified, necessary modifications and improvements are proposed to enhance their predictive capability.

Several correlations have been developed to predict droplet size in the PDO region in previous investigations. From Equation (4.5)-(4.8) in Table 4.4, the average droplet size correlations of Cumo et al. (1974), Ueda and Kim (1982), Kataoka et al. (1983), and Yoder and Rohsenow (1983),are displayed (hereinafter referred to as Cumo, Ueda, Kataoka and Yoder).

Among them, the Kataoka correlation is developed based on the mechanism of shearing off of the roll-wave crests in annular flow. Kataoka's correlation is usually used for the prediction of droplet size at the dryout point. Yoder derived a mechanistic correlation to predict droplet size by considering the formation of droplets from the liquid film and their subsequent development until the dryout point. The x_b is the steam quality at the point of droplet originating from the liquid film. The x_{do} is the steam quality at the dryout point. Ueda conducted experiments with a heated test section and derived an empirical correlation for droplet size at dryout point by fitting the experimental data. Cumo, on the other hand, performed experiments in dispersed flow and developed a correlation based on the equilibrium steam quality x_e and data fitting.

4.5.1 Assessment of Existing Droplet Size Correlations

(A) Assessment with KIMOF Experimental Data

These correlations are evaluated against the experimental data obtained in the present study, hereafter referred to as KIMOF. Since the droplet size is obtained from the PDO region, the equilibrium steam quality x_e is used to calculate the vapor velocity in these applied correlations. The prediction results with the correlations from Cumo, Ueda, and Kataoka are shown in Figure 4.21(a), while Yoder's correlation, which significantly deviates from the others, is displayed separately in Figure 4.21(b). Among the evaluated

Table 4.4: Summary of droplet size correlations

Author	Derived from	Droplet size correlation
Cumo	Post-dryout	$\frac{Gx_e d}{2\mu_d} = 123.1(1-P_R)^{0.31}$ (4.5)
Ueda	Dryout	$\frac{d}{D_t} = 6.1\times10^{-3}\left(\frac{\sigma}{\mu_g U_g}\left(\frac{\rho_g}{\rho_l}\right)^{1.25}\right)^{0.5}$ (4.6)
Kataoka	Pre-dryout	$\frac{d}{D_t} = 0.01\frac{\sigma}{\rho_g U_g^2} Re_g^{2/3}\left(\frac{\rho_g}{\rho_l}\right)^{-1/3}\left(\frac{\mu_g}{\mu_l}\right)^{2/3}$ (4.7)
Yoder	Dryout	$\frac{d}{D_t} = \frac{(x_b-0.1)}{(x_{do}-0.1)}\frac{d_{do}}{D_t} + \int_{x_b}^{x_{do}} \frac{d}{D_t}\frac{dx}{(x_{do}-0.1)}$ (4.8)

models, Kataoka's correlation predicts the smallest droplet sizes, while Yoder's correlation significantly overestimates the average droplet size. The assessment results indicate that the Cumo and Ueda correlations demonstrate the best overall agreement with experimental data. However, discrepancies remain: Cumo's correlation underestimates droplet size at higher pressures, while Ueda's correlation, despite capturing the trend well, also tends to underestimate droplet size, necessitating further refinement.

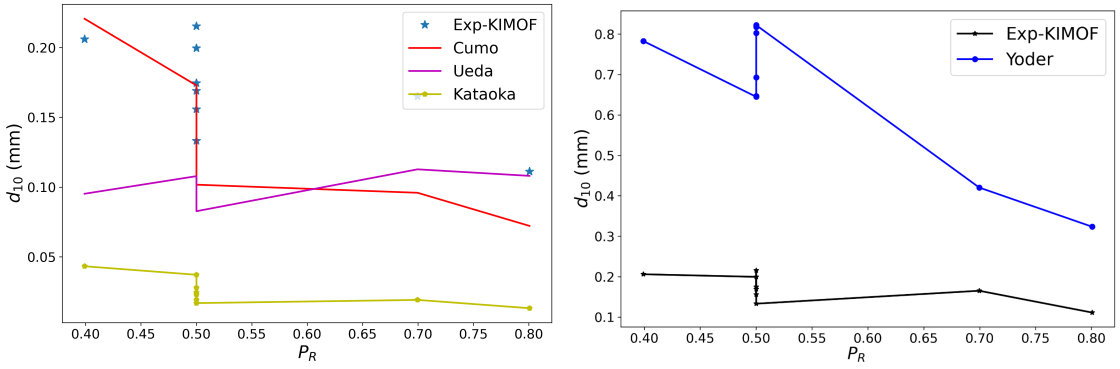

(a) Correlations of Cumo, Ueda and Kataoka

(b) Yoder correlation

Figure 4.21: Assessment of droplet size correlations with the KIMOF data

(B) Assessment with Cumo experimental data

Additional evaluation is conducted using Cumo's experimental data and displayed in Figure 4.22. In the work of Cumo et al. (1974), through a visualized test section the droplets diameter was recorded under various steam qualities and pressures at an almost constant mass flux of 900 kg/(m²·s). The Cumo correlation was developed with the most probable droplet size as the characteristic parameter to fit the experimental data. As a result, when extracting the average droplet size from Cumo's experiments, the predictions of Equation (4.5) show relatively larger deviations from the measured droplet size, particularly at in-

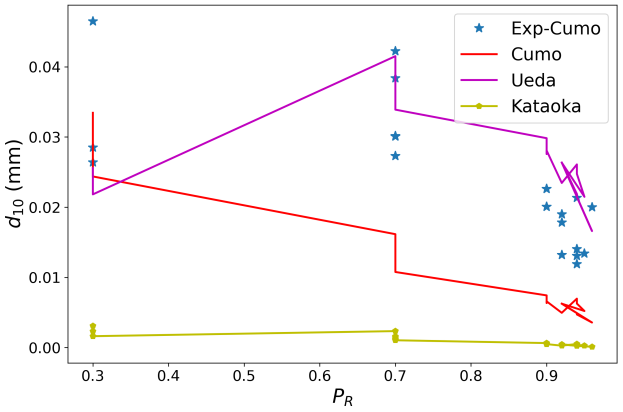

Figure 4.22: Assessment of droplet size correlations with Cumo's experiment data

termediate and high pressures. This discrepancy likely arises from the inherent difference between the most probable droplet size used in Cumo's correlation and the actual average droplet size observed in the experiments. Additionally, the Ueda correlation tends to overestimate droplet size at higher pressures and underestimate it at lower pressures, suggesting that the pressure effect may not be fully captured in its formulation. Furthermore, due to the absence of the heat flux data in Cumo's experiments, Yoder's correlation could not be evaluated under these conditions, as it explicitly relies on heat flux as an input parameter.

(C) Assessment with Ueda Experimental Data

To further evaluate the predictive accuracy of these correlations, additional assessments are conducted using Ueda's dataset. In Ueda's experiments, dryout was controlled to occur at the outlet, ensuring that the collected droplets accurately represent the droplet size at the dryout point. This dataset covers a wider mass flux range from 218 to 887 kg/(m^2·s), addressing the limited mass flux variations in the previous datasets and providing a broader basis for assessing the correlations across different mass flux conditions. As shown in Figure 4.23(a), Yoder's correlation significantly overpredicts the droplet size across all mass flux conditions. Cumo's correlation also exhibits a strong overestimation trend in Figure 4.23(b). Among the evaluated models, only Ueda's correlation demonstrates good agreement with its own dataset, indicating that it captures the mass flux dependency more accurately than the others.

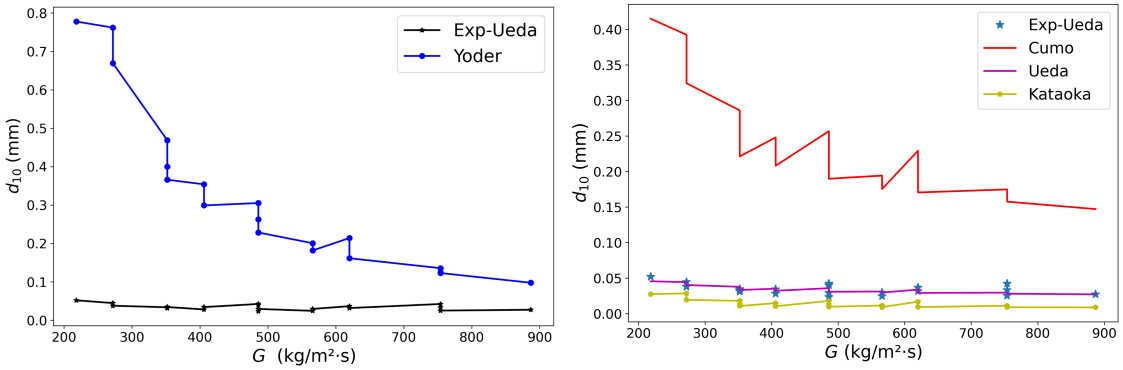

(a) Yoder correlation

(b) Correlations of Cumo, Ueda and Kataoka

Figure 4.23: Assessment of correlations with Ueda's experimental data

The assessments above reveal that Ueda's correlation shows the best performance., particularly when compared with Cumo's and Ueda's experimental data. However, it fails to capture the droplet size variation with pressure observed in the current experimental work. While Cumo's correlation provides good predictions for the present experiments, it significantly overpredicts droplet size when applied to Ueda's data. Yoder's correlation, on the other hand, consistently overpredicts all experimental data by a large margin. These findings highlight a key limitation: no existing correlation accurately predicts droplet size under all the three datasets. Therefore, a new correlation is needed to be developed by integrating the literature experimental data with the present dataset to improve overall predictive capability.

4.5.2 Improved Droplet Size Correlation

The assessments of correlations indicate that Ueda's and Cumo's correlations give reasonable prediction. From Equation (4.5) and (4.6), Cumo's correlation is developed based on the droplet Reynold number (Re) while Ueda developed their correlation based on the ratio of droplet Weber number (We) and Re. Therefore, this section applies these two dimensionless numbers and develops an improved empirical correlation for droplet size under PDO conditions.

$$Re = \frac{Gx_e d_{10}}{\mu_l} \tag{4.9}$$

$$We = \frac{\rho_v u_v^2 d_{10}}{\sigma} \tag{4.10}$$

For droplets in the vapor flow, the density ratio affects the interfacial drag effect by affecting the slip ratio, while the surface tension limited the maximum droplet size. Therefore, to analyze the pressure effect on droplet size, the trends of surface tension and the density ratio between vapor and droplets with pressure are displayed in Figure 4.24 and Figure 4.25, the data points represent the trend of fluid property changing with reduced pressure P_R. As the pressure decreases, it can be seen that the density difference between the phases increases, which indicates greater relative velocity between phases compared to conditions at higher pressure. Then the increasing weber number tends to reduce the maximum droplet size due to droplets break-up. However, simultaneously, the surface tension increases as pressure decreases, which tends to increase the droplet size. Therefore, the pressure effect on droplet size must account for both the surface tension and drag effects.

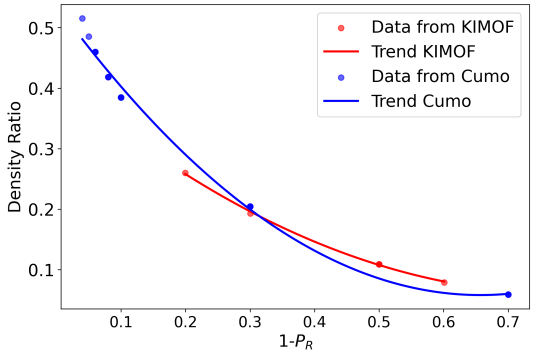

Figure 4.24: Density Ratio vs. (1-P_R)

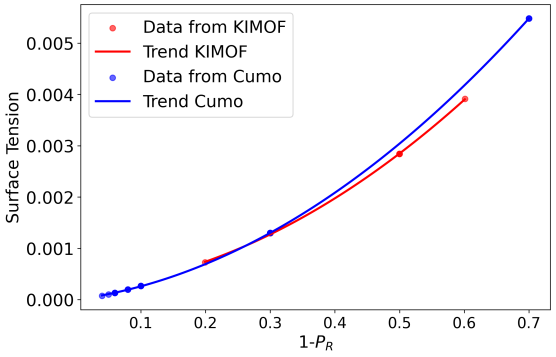

Figure 4.25: Surface Tension vs. (1-P_R)

According to Cumo et al. (1974), the droplet Reynolds number calculated with d_* exhibits a logarithmic and linear proportionality to the reduced pressure. However, as shown

in the Figure 4.26, the calculated droplet Reynolds number from Equation (4.9) with experimental data of Cumo and KIMOF, the relationship between the droplet Reynolds number and $(1 - P_R)$ significantly deviates from linearity, especially for the data from Cumo. In Ueda's correlation, the term $\sigma/(\mu_g U_g)$ represents the ratio of the droplet Weber

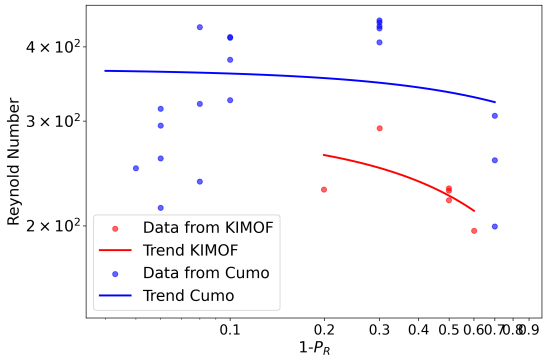

Figure 4.26: Relationship of Re vs. (1-P_R)

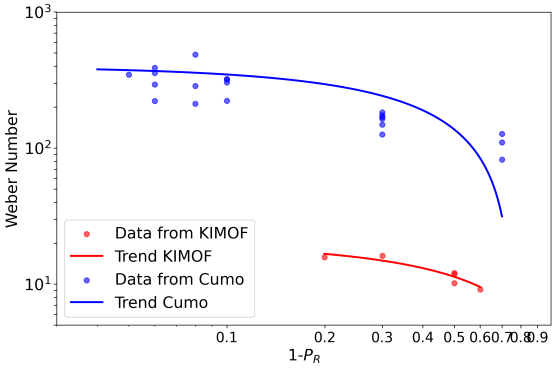

Figure 4.27: Relationship of We vs. (1-P_R)

number to the droplet Reynolds number. The tube diameter is used for the purpose of obtaining a dimensionless droplet size, implying a linear proportionality between the droplet size and the tube diameter. This assumption, however, lacks physical support. As the Weber number is plotted against varying pressure, as shown in Figure 4.27, a well-fitted curve is observed. Therefore, the Weber number defined in Equation (4.10) is selected as the characteristic dimensionless number for analyzing the droplet size in the current study.

To develop a correlation with the droplet Weber number, the relationships between various influencing parameters and the Weber number are systematically investigated. As discussed earlier, the effect of pressure on droplet size arises from the combined influence of surface tension and the phases density ratio. While the surface tension component is inherently accounted for within the definition of the Weber number, the effect of the density ratio must be explicitly considered. The relationship between the Weber number and the density ratio is therefore analyzed and presented in Figure 4.28. It is observed that the Weber number exhibits a clear positive and approximately linear correlation with the density ratio. Therefore, by fitting the experimental data from KIMOF and Cumo, a correlation

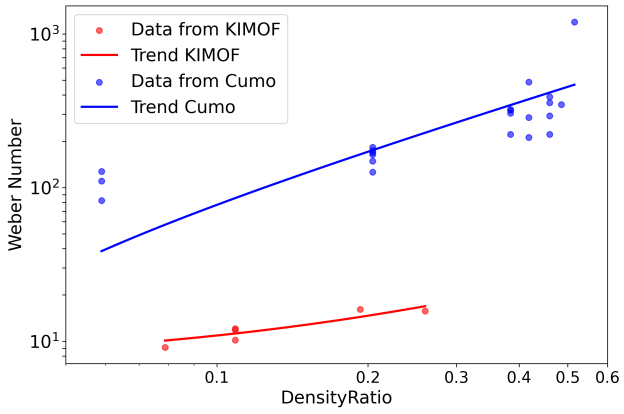

Figure 4.28: Relationship of We vs. Density Ratio

based on the droplet Weber number is developed, as shown in Equation (4.11), relating the vapor Reynolds number Re_v and the density ratio ρ_v/ρ_d. As shown in Figure 4.29, the points are the experimental data and the dashed line is the predicted Weber number against the pressure $(1 - P_R)$. By comparing with the Weber number calculated from

the experimental droplet size, the correlation in Equation (4.11) accurately predicts the relationship between the Weber number and pressure across different mass flux conditions.

$$\frac{\rho_v u_v^2 d_{10}}{\sigma} = 3 \times 10^{-4} \, \mathrm{Re}_v^{1.2} \left(\frac{\rho_v}{\rho_d} \right) \tag{4.11}$$

where the vapor velocity u_v and vapor Reynolds number Re_v are calculated as:

$$u_v = \frac{G x_e}{\rho_v} \tag{4.12}$$

$$\mathrm{Re}_v = \frac{G D_t}{\mu_v} \tag{4.13}$$

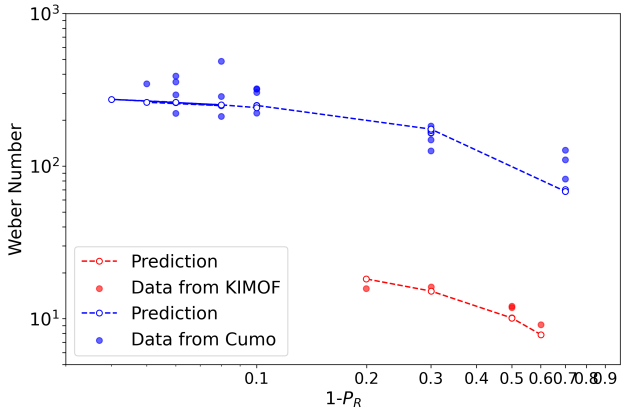

Figure 4.29: Comparison of predicted and experimental We as the variation of (1-P_R)

Besides, based on Equation (4.11), the average droplet sizes predicted by the newly developed correlation are presented in Figure 4.30, together with the results from Ueda's and Cumo's empirical correlations. Figure 4.30(a) shows the comparison between the pre-

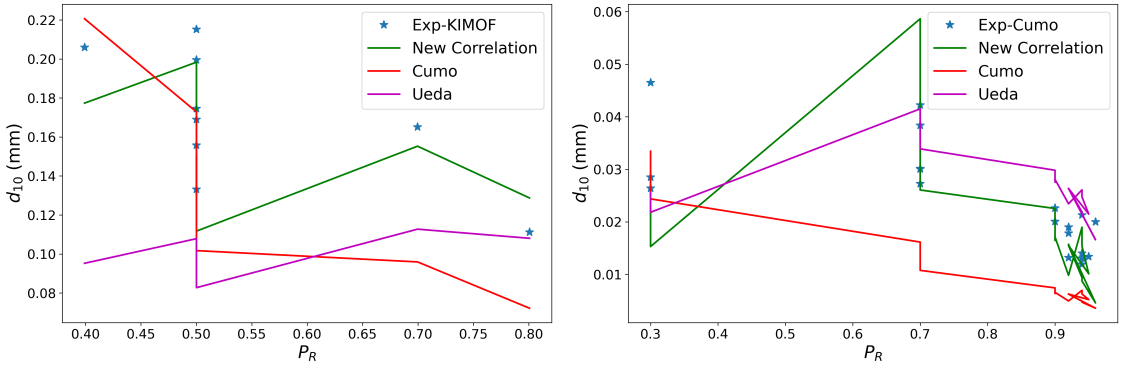

(a) Correlations of Cumo, Ueda and Kataoka

(b) Yoder correlation

Figure 4.30: Comparison of the predicted d_{10} with experiment data from KIMOF and Cumo

dicted droplet sizes and the KIMOF experimental data, as a function of reduced pressure. It can be observed that the new correlation exhibits the best agreement with the experimental results and accurately captures the variation of droplet size with pressure, which is not well predicted by the Ueda and Cumo correlations. A similar trend is found in

Figure 4.30(b), where Cumo's experimental dataset is used for assessment. The newly developed correlation consistently outperforms the other two empirical models, particularly under high-pressure conditions, where it provides significantly more accurate predictions of droplet size.

Additionally, to further evaluate the generalizability of the new correlation, droplet size data from Ueda's experiments—which were not involved in the model development—are employed for validation. Figure 4.31 presents the predicted droplet sizes as a function of mass flux, along with Ueda's measurements. It is evident that the new correlation maintains high predictive accuracy for these independent data, further confirming its robustness and applicability beyond the specific conditions used during its formulation.

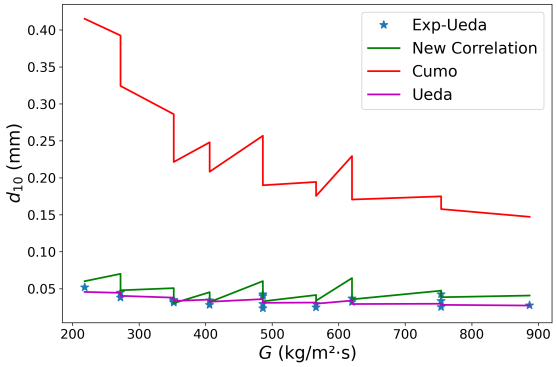

Figure 4.31: Assessment of predicted d_{10} with experiment data from Ueda

4.5.3 Droplet Velocity Correlation

The slip ratio correlation developed in Yoder and Rohsenow (1983) is selected and assessed with the present data points. As shown in Equation (4.14), the slip ratio is predicted to be proportionally to droplet size and boiling number. The inverse relationship between the density ratio and the slip ratio indicates that as pressure increases and the density difference decreases, the density ratio increases, leading to a smaller slip ratio. This trend is consistent with the behavior shown in Figure 4.18(a). On the other hand, as steam quality increases, the slip ratio decreases accordingly. At the same time, the droplet velocity increases with the rise in steam quality, aligning with the trend observed in Figure 4.17(a). During the assessment, the actual steam quality is assumed to be 1.0, as these cases have thermal equilibrium steam quality significantly larger than 1.0. Vapor properties, such as $\rho_{v,e}$ are estimated based on the equilibrium vapor temperature.

The predicted droplet velocity is plotted against the experimental average droplet velocity in Figure 4.32. It can be seen that Yoder's slip ratio correlation predicts the droplet velocity with good accuracy. Overall, Yoder's correlation is shown to provide reliable predictions and is well aligned with the experimental data.

$$S_{\text{cal}} = \frac{U_v}{U_d} = 1 + 2.31 \left[\frac{\rho_d}{\rho_{v,e}} \frac{1}{x_a} \frac{q''_w}{G h_{lg} C_D} \frac{d}{D_t} \right]^{0.5} \tag{4.14}$$

The vapor velocity U_v is given by:

$$U_v = \frac{G x_a}{\rho_{v,e}} \tag{4.15}$$

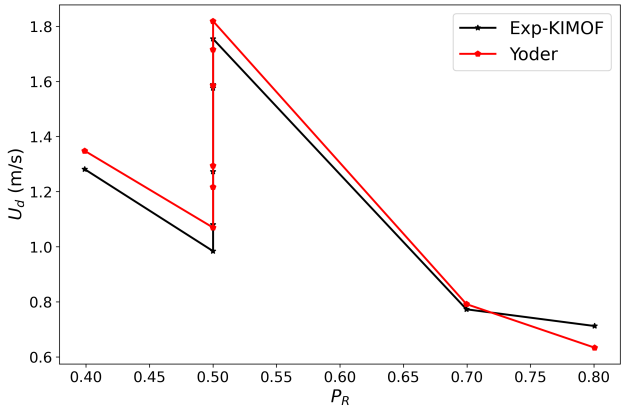

Figure 4.32: Comparison of the predicted droplet velocity with Yoder's slip ratio correlation and the experimental data

4.6 Chapter Summary

This chapter presents an experimental investigation on the droplet behaviors in the PDO region. The droplet dynamics inside the flow channel are captured and recorded into image sequences. By post-processing the continuous images, droplet size, position, and velocity information are obtained under various conditions, including different pressures, mass fluxes, and heat fluxes. Correlations of droplet size and velocity are assessed and improved using the experimental data from the present study and existing literature. Key findings include:

- As heat flux increases, steam quality at the observation window also increases, resulting in a decrease in droplet size. A clear inverse relationship between steam quality and droplet size is observed by comparing the average droplet size with the equilibrium steam quality.
- An increase in pressure leads to a reduction in droplet size. The decrease rate of droplet size becomes more pronounced at high pressure ranges.
- Correlations from the literature are evaluated using the experimental data from the current study, as well as from the works of Cumo and Ueda. Among these, Yoder's equation consistently overpredicts the droplet size, while Kataoka's equation consistently underpredicts it. In contrast, Ueda's and Cumo's correlations provide more reasonable predictions. However, Cumo's correlation performs poorly when compared with Ueda's data, while Ueda's correlation fails to accurately predict the droplet size measured in the present study.
- A new correlation for the average droplet size under PDO conditions is developed. The inclusion of the droplet Weber number accounts for surface tension effects, while the interfacial drag effect, which varies with pressure, is incorporated using the density ratio. Additionally, the vapor Reynolds number is introduced to better capture turbulence effects on droplet size. Assessment with droplet datasets of Cumo, Ueda and KIMOF demonstrates the high prediction accuracy of the new correlation.
- Droplet axial velocity is significantly affected by variations in both pressure and mass flux. The pronounced impact from pressure is mainly attributed to the variation in fluid density. In comparison, the effect of heat flux is relatively minor, leading to a slight increase in droplet velocity as a result of higher steam quality.
- Droplet radial velocity follows a close standard normal distribution, with most droplets concentrated around radial velocities close to zero. The effect of mass flux on the

radial velocity distribution is more significant compared to the influence of pressure and heat flux variations.

- Based on the average droplet velocity obtained from experiments, Yoder's slip ratio correlation accurately predicts droplet velocity.

Overall, the experimental results presented in this chapter provide valuable insights into droplet dynamics in the PDO region. The effects of pressure, heat flux, and mass flux on droplet size and velocity are thoroughly investigated. The validated slip ratio correlation from Yoder will be recommended for the droplet velocity prediction in the PDO models. The newly developed correlation offers a more accurate prediction of droplet size, enhancing the overall understanding of droplet behavior in the PDO region.

5. Development and Assessment of PDO Heat Transfer Model

This chapter presents an improved mechanistic model for PDO heat transfer that incorporates key physical phenomena influencing heat and mass transfer. Building on a one-dimensional framework, the prediction of interfacial heat transfer in the PDO region is enhanced by integrating insights from CFD simulations and experimental results. The proposed model distinguishes between droplet evaporation in the central and the near-wall regions, accounting for lateral droplet motion and non-uniform vapor temperature to better represent vapor-droplet interactions. Additionally, the droplet deposition model is updated to reflect the influence of evaporation within the vapor flow. Furthermore, the new droplet size correlation developed from the experimental work in Chapter 4 is implemented. The proposed model is validated against experimental data from literature under a wide range of thermal-hydraulic conditions. Comparisons with existing PDO heat transfer models and published droplet size correlations demonstrate the improved accuracy and robustness of the present PDO model.

5.1 Model Description

In the PDO region, the heated wall is no longer covered by a continuous liquid film. The vapor is continuously heated by convective heat transfer from the wall and becomes superheated. The presence of droplets in the PDO region slows the speed of vapor superheating and limits the increase in wall temperature. Given the high wall temperature, droplets rarely contact with the wall, preventing efficient heat transfer (Kendall and Rohsenow, 1978). To prioritize improvements in the interfacial heat transfer model while minimizing potential errors, the present PDO heat transfer model neglects direct wall-droplet heat transfer and radiation heat transfer. A 1-D approach is employed to account for the development of vapor flow and droplet iteratively along the heated length. The main improvement lies in the calculation of interfacial heat transfer, which is enhanced by dividing the flow region into a central region and a near-wall region. Additionally, the deposition model between these regions is refined for PDO conditions.

5.1.1 1-D Approach with Mass and Energy Balance

The 1-D approach employed in the model development is illustrated in Figure 5.1. The proposed model takes the dryout point as the starting location for calculations, discretizes the

flow domain into coarse nodes along the mainstream direction, and solves for key parameters such as wall temperature and vapor temperature at each node under the boundary condition of pressure P, mass flux G, wall heat flux q''_w and tube diameter D_t.

At the beginning of the calculation, the steam quality x_{do}, droplet size d_{do} and vapor void fraction α_{do} at the dryout point must be initialized. It is assumed that at this point, the vapor and droplets are in thermal equilibrium, both at the saturation temperature, and the actual steam quality equals the equilibrium steam quality. The initial droplet size at the dryout point evaluated through correlations developed in Chapter 4. In addition, the vapor void fraction at dryout point, α_{do}, is required for interfacial heat transfer calculations and is determined using Equation (2.77), which depends on the slip ratio S. According to the assessment in Chapter 4, Equation (4.14) from Yoder and Rohsenow (1983) is employed to calculate the slip ratio in PDO region.

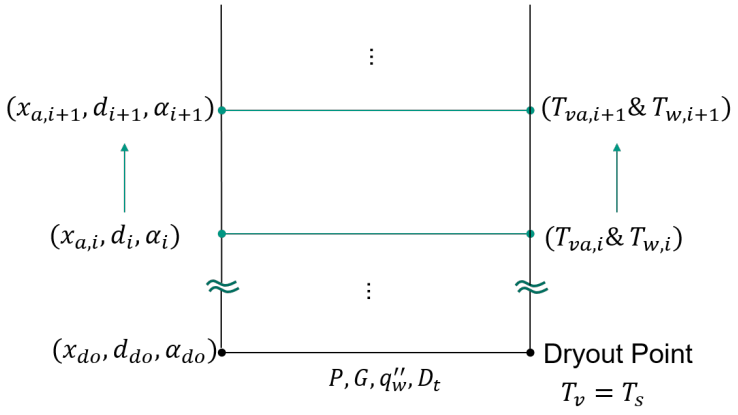

Figure 5.1: Schematic of 1-D approach

After initialization, the interfacial heat transfer within each cell Q_{vd} is calculated. Then the droplet evaporation rate is determined. The steam quality, droplet size and vapor void fraction in the next node, $x_{d,i+1}$, d_{i+1}, α_{i+1}, are then computed based on the droplet evaporation rate. The thermal energy change in the vapor phase is determined as the difference between the heat obtained from the wall and the heat transferred to the droplets. This allows for the calculation of the vapor temperature at the next node $T_{va,i+1}$. Subsequently, using the vapor temperature and convective heat transfer coefficient, the wall temperature $T_{w,i+1}$ is also obtained.

Compared to two-dimensional or three-dimensional models, one-dimensional models have a lower computational cost and better convergence, making them well-suited for rapid analysis and parameter optimization in engineering applications. However, the assumption of uniformity in radial direction used in previous instigation may introduce certain uncertainties. To address this limitation, the proposed model divides each cell into two regions when calculating interfacial heat transfer, allowing for a more accurate representation of the heat transfer mechanism.

5.1.2 Two-Region Model

From the CFD simulation in Chapter 3, over 50% of droplet evaporation occurs in the near-wall region, which occupies only 25% of the total flow area. This indicates that the droplet evaporation rate in the near-wall region is nearly three times higher than that in the central region. Given this substantial variation in droplet evaporation across radial positions, the interfacial heat transfer in the mechanistic model needs to be treated differently than with the averaging methods commonly used in the literature. In this study, as shown in

Figure 5.2, a two-region model is developed by dividing the entire flow region radially into a central region and a near-wall region at radial position of r_{cr} to account for the difference in evaporation density. Simulation analysis shows that the intense evaporation near the wall is primarily due to the elevated vapor temperature. Consequently, the boundary between the central region and the near-wall region is defined by the vapor temperature profile T_v.

As the droplets absorb heat from superheated vapor and evaporate into vapor with saturated temperature, the new generated vapor absorbs heat from the superheated vapor and also increases the mass flow rate of vapor flow. The evaporation effect on vapor temperature and vapor velocity profile is included in the newly developed two-region model. A vapor temperature profile for the PDO region is fitted according to CFD results in Chapter 3, providing the vapor temperature for calculating interfacial heat transfer in the near-wall region. Additionally, the droplet lateral movement from the central region to the near wall region is included in the two-region model. Through qualitative and quantitative analysis of the CFD simulation results, the vapor temperature profiles and droplet deposition are modeled and implemented into the mechanistic model for a more reliable prediction of interfacial heat transfer. The wall temperature then can be obtained by employing the wall-vapor convective heat transfer model developed by Yu (2019).

In the current two-region model, the following assumptions are made:

- All droplets are assumed to be spherical, with uniform size and axial velocity in two regions at the same axial elevation.
- At the dryout point, droplets are assumed to be evenly distributed along the radial direction and at saturated temperature.

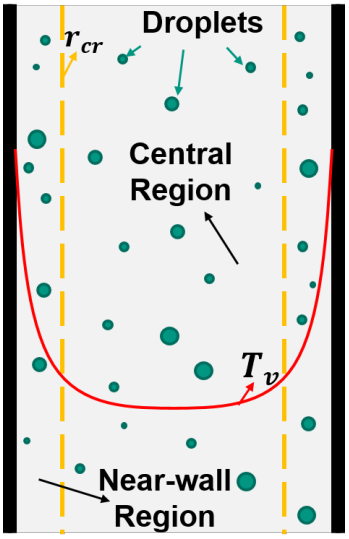

Figure 5.2: Schematic of two-region model and vapor temperature profile (Xia and Cheng, 2025a)

A detailed description of the two-regions model for interfacial heat transfer calculations is provided in the following sections.

5.1.3 Development of Interfacial Heat Transfer Model

5.1.3.1 Two Regions Separation

In Figure 5.3, a typical profile of vapor superheating $T_{v,sup}$ along the radial direction in the PDO region is represented by the red dotted line. The black dashed line represents

the superheat degree of bulk vapor temperature $T_{b,sup}$. A high temperature gradient is observed across the radial direction. The vapor superheating decreases sharply from the wall to the position of $y^+ = 300$, marked by the green dashed line. In this region, the vapor temperature significantly exceeds the bulk temperature. Using the bulk temperature to calculate interfacial heat transfer fails to capture the near-wall effects and is likely introduce a substantial prediction error. Therefore, the flow region is divided into near-wall region and a central region at $y^+ = 300$. The interfacial heat transfer is calculated separately within these two regions. Sensitivity analysis indicates that the predicted wall superheating is not that sensitive to the selection of y^+ value of the separation line.

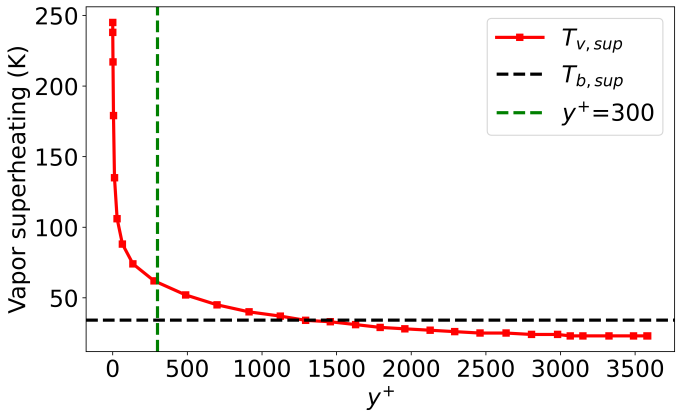

Figure 5.3: Profile of vapor temperature in radial direction from CFD simulation in Chapter 3 (Xia and Cheng, 2025a)

5.1.3.2 Droplet Evaporation in Two Regions

Figure 5.4 illustrates the separation of regions from the top view and the calculation process of droplet evaporation over a distance increment Δz from the front view. In the front view, the green rectangle marks the central region, while the two red rectangles denote the near-wall regions. Droplets initially enter the central region and the near-wall region with mass flow rates of $m_{d,c0}$ and $m_{d,n0}$, respectively. During their travel over the axial distance of Δz, droplets evaporate and decrease in size according to the amount of heat they gain from the surrounding vapor. The interfacial heat flow rates in the near-wall region $Q_{vd,n}$ and in the central region $Q_{vd,c}$ are calculated separately, each contributing to the reduction of $m_{d,n0}$ and $m_{d,c0}$. The total interfacial heat transfer between droplets and superheated vapor in this step is represented by the sum of $Q_{vd,c}$ and $Q_{vd,n}$, contributes to an increase in the actual steam quality x_a and vapor void fraction α. In addition to evaporation, droplets are transported from the central region toward the near-wall region, as indicated by the blue arrow and quantified by m_{dep}, representing the net droplet deposition rate.

Given the steep gradient in vapor temperature near the wall, this model, unlike Yu's PDO model (Yu, 2019) which employs an average temperature of wall temperature and bulk temperature, fits a correlation for the vapor temperature profile in the PDO region. From CFD results in Chapter 3, a profile of dimensionless vapor temperature T^+ is correlated and shown below:

$$T^+ = Pr_{vw} \cdot y^+, \quad \text{if } y^+ < y^+_{tr} \tag{5.1a}$$

$$T^+ = 0.6 \cdot \frac{Pr_{vwb}}{k_\Theta} \cdot \ln(y^+) + b_0, \quad \text{if } y^+ \geq y^+_{tr} \tag{5.1b}$$

where y^+_{tr} is the crossing point of the Equations (5.1). Pr_{vw} is the Prandtl number of vapor at the wall temperature T_w, and Pr_{vwb} is the Prandtl number of vapor at the average

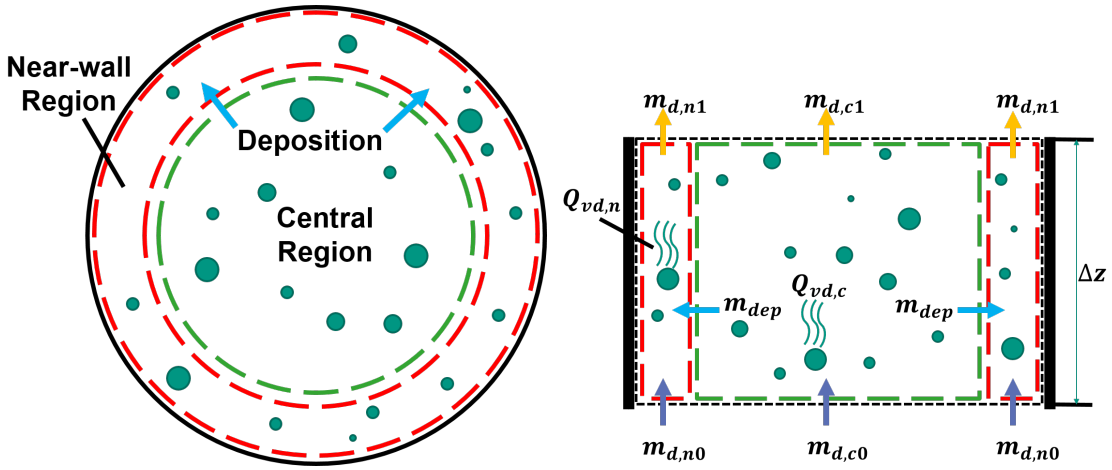

(a) Top view (b) front view

Figure 5.4: Evaporation and deposition of droplets in the new two-region model (Xia and Cheng, 2025a)

temperature of wall temperature and vapor bulk temperature T_{vb}. k_Θ is the Karman constant, and the value of b_0 is determined by the energy balance. With this correlation, the vapor temperature in the radial direction can be calculated as:

$$T_{v,y} = T_w - \frac{T^+ q''_w}{\rho_v c_{p,v} u^*} \tag{5.2}$$

With the vapor temperature known at various radial positions, the near-wall region is discretized laterally into N small slices using logarithmic spacing. In each slice, the vapor temperature is determined, and the corresponding heat transfer in the near-wall region $Q_{vd,n}$ is then calculated. $Q_{vd,c}$ is calculated with the average vapor temperature in the central region, as the temperature gradient in this region is small. The expressions for $Q_{vd,n}$ and $Q_{vd,c}$ are given as follows:

$$Q_{vd,n} = \frac{\sum_{i=0}^{N}(T_{v,i} - T_s) A_{n,i} h_{vd,n}(1-\alpha_n)\Delta z}{d} \tag{5.3}$$

$$Q_{vd,c} = \frac{(T_{vc} - T_s) A_c h_{vd,c}(1-\alpha_c)\Delta z}{d} \tag{5.4}$$

The average vapor temperature in the central region T_{vc} is given by:

$$T_{vc} = \frac{T_{vb} A_t - \sum_{i=0}^{N} T_{v,i} A_{n,i}}{A_c} \tag{5.5}$$

The selection of interfacial heat transfer coefficient correlation is based on the range of the relative Reynolds number Re_d:

For $Re_d \leq 250$ (Lee and Ryley, 1968):

$$h_{vd} = \frac{(2 + 0.74 Re_d^{0.5} Pr_v^{1/3}) k_v}{d} \tag{5.6}$$

For $250 < Re_d \leq 450$ (Ranz et al., 1952):

$$h_{vd} = \frac{(2 + 0.6 Re_d^{0.5} Pr_v^{1/3}) k_v}{d} \tag{5.7}$$

For $Re_d > 450$ citepHughmark1967:

$$h_{vd} = \frac{(2 + 0.27 Re_d^{0.62} Pr_v^{1/3}) k_v}{d} \tag{5.8}$$

where

$$Re_d = \frac{\rho_v |u_d - u_v| d}{\mu_v} \tag{5.9}$$

The vapor properties are calculated according to the average vapor temperature of each region.

According to the definition of void fraction, the ratio of the liquid fraction can be expressed as shown in Equation (5.10). The liquid volume fractions in the two regions are then obtained by combining Equations (5.10) and (5.11). S is the slip ratio and calculated by Equation (4.14).

$$\frac{1 - \alpha_c}{1 - \alpha_n} = \frac{m_{d,c}}{m_{d,n}} \cdot \frac{u_{d,n}}{u_{d,c}} \cdot \frac{A_n}{A_c} \tag{5.10}$$

$$(1 - \alpha_n) A_n + (1 - \alpha_c) A_c = (1 - \alpha) A_t \tag{5.11}$$

According to Lee's experimental data (Lee and Durst, 1982) shown in Figure 3.14, the droplet axial velocity changes slightly by approaching to the near-wall region. Therefore, the difference of droplet axial velocity in two regions is ignored. The liquid fractions in both regions are determined based on the ratio of droplet mass flux in two regions. After obtaining the values of $Q_{vd,n}$ and $Q_{vd,c}$, the change in droplet mass flow is iterated across the two regions over the distance of Δz. This allows the calculation of the mass flow rate at the outlet of the current step, which also serves as the inlet for the next step:

$$m_{d,c1} = m_{d,c0} - m_{dep} - \frac{Q_{vd,c}}{h_{lg}} \tag{5.12}$$

$$m_{d,n1} = m_{d,n0} + m_{dep} - \frac{Q_{vd,n}}{h_{lg}} \tag{5.13}$$

The amount of droplet deposition between the two regions, m_{dep}. The steam quality at this elevation is calculated with:

$$x_a = 1 - \frac{m_{d,c1} + m_{d,n1}}{m_{in}} \tag{5.14}$$

5.1.3.3 Droplet Deposition Between Two Regions

Previous research on droplet deposition has shown that droplets in the gas phase tend to move toward the wall. This droplet deposition phenomenon is caused by the radial fluctuation velocity of the gas phase. Figure 5.5 presents a schematic of the dimensionless vapor fluctuation velocity profile v'^{+}, depicted by a purple line based on the work of Laufer (1954). The radial velocity fluctuation of the vapor increases from the wall over a short distance and then decreases as it approaches the tube center. The near-wall region extends from the wall to $y_{cr}^{+} = 300$, where a high gradient of vapor velocity fluctuation occurs. To address droplet lateral movement within this region, the near-wall region is divided into the wall boundary region and the transition region, with $y_{cw}^{+} = 30$ as the separation line. The wall boundary region and transition region have droplet concentrations C_{nw} and C_{nt}, respectively. The droplet concentration in the central region is denoted as C_c. Simulation

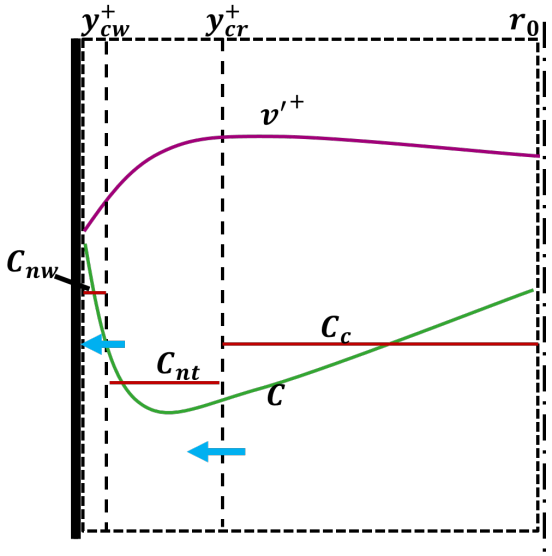

Figure 5.5: Profiles of vapor fluctuation velocity and droplet concentration (Xia and Cheng, 2025a)

results from the CFD investigation in Chapter 3 show that the droplet concentration profile has a V-shaped distribution under the turbulent dispersion, as represented by a green line in Figure 5.5. In combination with the vapor velocity fluctuation profile, droplets gain momentum and exhibit random motion within the flow due to the stochastic fluctuations of the vapor phase. Droplets are distributed radially according to the vapor velocity fluctuation profile. As a result, a concentration valley forms in the transition region following the profile of vapor fluctuation velocity. The droplet lateral movement from the central region to the near-wall region can thus be approximated as being driven by the concentration difference between the central region and the transition region.

The deposition rate from the central region to the near-wall region is calculated with the particle diffusion equation:

$$m_{\text{dep}} = (D + \varepsilon_d)\frac{dC}{dy}A_{cr} \tag{5.15}$$

where A_{cr} is the deposition area, representing the surface area of the boundary between the central region and the near-wall region. ε_d is the droplet turbulent diffusivity, while D is the droplet molecular diffusivity. Compared to turbulent dispersion (Yang and Lee, 1991; Lee and Wiesler, 1987), the molecular diffusion is too small to be considered. dC is the concentration difference from the central region to the transition region, which can be estimated by the difference of C_c and C_{nt}. Thus, Equation (5.15) can be rewritten as a difference equation:

$$m_{dep} = \varepsilon_d \frac{C_c - C_{nt}}{\Delta y}A_{cr} \tag{5.16}$$

The droplet concentrations in the central and near-wall regions are calculated using the liquid void fraction:

$$C_c = (1 - \alpha_c)\rho_d \tag{5.17}$$

$$C_n = (1 - \alpha_n)\rho_d \tag{5.18}$$

To calculate the net deposition rate, the droplet concentration within the transition region, C_{nt}, is required.

From Hinze (1959), and Lee and Wiesler (1987), for short diffusion times, the droplet turbulent diffusivity ε_d can be expressed as:

$$\varepsilon_d = \eta_e^2 \varepsilon_v \tag{5.19}$$

where ε_v is the vapor eddy viscosity, and η_e^2 is the fluctuation amplitude of the droplet relative to that of the vapor in the turbulent core. By obtaining ε_v and η_e^2, the droplet turbulent viscosity can be calculated. These two parameters need to be modified to fit the PDO conditions.

The following sections describe the calculations of the three unknown parameters C_{nt}, ε_v, and η_e^2 in the current deposition model.

Calculation of C_{nt}:

Based on the mechanism of lateral droplet movement near the wall, the droplet within the wall boundary region is governed by the possibilities of droplets entering versus exiting this region, which is influenced by the disparity in vapor fluctuation velocities between the transition and wall boundary regions. Thus, the droplet concentration ratio c_{ow} between the wall boundary region and the transition region is quantitatively represented by the ratio of their respective average vapor fluctuation velocities:

$$\frac{C_{nw}}{C_{nt}} = \frac{v'_{v,nt}}{v'_{v,nw}} = c_{ow} \tag{5.20}$$

Experimental data from Laufer (1954) is displayed in Figure 5.6. Beal (1970) fitted the

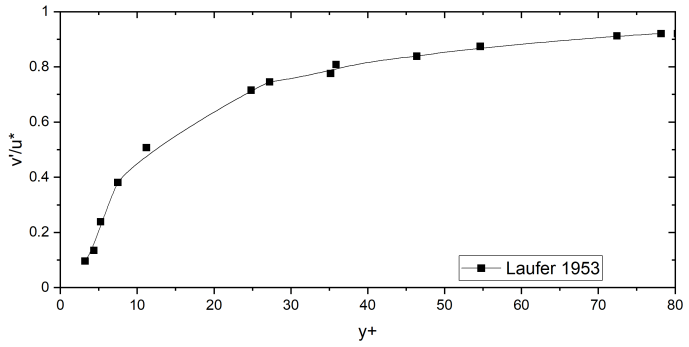

Figure 5.6: Profile of dimensionless fluctuation velocity of gas in radial direction

experimental data and obtained the following correlations:

$$\frac{v'_v}{u^*} = 0.05y^+, \quad 0 \leq y^+ \leq 10 \tag{5.21}$$

$$\frac{v'_v}{u^*} = 0.5 + 0.0125(y^+ - 10), \quad 10 \leq y^+ \leq 30 \tag{5.22}$$

The average fluctuation velocity in the wall boundary region and transition region can be estimated as:

$$v'_{v,nw} = 0.48u^* \tag{5.23}$$

$$v'_{v,nt} \approx 0.93u^* \tag{5.24}$$

$$c_{ow} = 1.9375 \tag{5.25}$$

With this ratio, the droplet concentration in the transition region can be calculated as:

$$C_{nt} = \frac{C_n A_n}{A_{nt} + c_{ow} A_{nw}} \tag{5.26}$$

Calculation of ε_v:

The eddy viscosity of vapor ε_v is considered to not be constant across the turbulent core. Kays (1966) and Reichardt (1951) fitted the radial profile of vapor eddy viscosity as:

$$\varepsilon_v = \frac{k_\Theta r_0 u^*}{6}\left[1 - \left(\frac{r}{r_0}\right)^2\right]\left[1 + 2\left(\frac{r}{r_0}\right)^2\right] \tag{5.27}$$

which is referenced from single-phase experiments. To implement it for the dispersed flow, Equation (5.27) needs to be modified considering the droplet evaporation effect.

From the work of Reichardt (1951), the Equation (5.27) is used to generate a profile of dimensionless axial velocity u^+. A relationship between u^+ and ε_v can be found as:

$$\varepsilon_v = \frac{\mu y_r^+ d\left(\frac{r}{r_0}\right)^2}{d(u^+)} \tag{5.28}$$

A u^+ correlation for single-phase flow is then obtained in Reichardt (1951) by combining Equation (5.27) and (5.28):

$$u^+ = 2.5 \ln\left(y^+ \frac{1.5\left(1 + \frac{r}{r_0}\right)}{1 + 2\left(\frac{r}{r_0}\right)^2}\right) + 5.5 \tag{5.29}$$

In the PDO region, droplets absorb heat from the vapor and evaporate into vapor, which modifies the vapor velocity profile. Therefore, when the u^+ profile in Equation (5.29) is applied to describe the velocity profile in the PDO region, it slightly differs from the CFD simulated u^+ profile. Thus, the u^+ correlation is modified according to the CFD simulated vapor velocity profile as:

$$u^+ = 2.5 \cdot c_{ofu} \ln\left(y^+ \frac{1.5\left(1 + \frac{r}{r_0}\right)}{1 + 2\left(\frac{r}{r_0}\right)^2}\right) + b_1 \tag{5.30}$$

$$c_{ofu} = 0.88 \cdot (Pr_{vwb})^{0.3} (Pr_s)^{0.1} \tag{5.31}$$

The c_{ofu} accounts for the effect of droplet evaporation on the vapor velocity profile. Therefore, from Equation (5.28) and (5.30), the ε_v in the PDO region accounting for the droplet evaporation effect can be rewritten as:

$$\varepsilon_v = \frac{k_\Theta r_0 u^*}{6 \cdot c_{ofu}}\left[1 - \left(\frac{r}{r_0}\right)^2\right]\left[1 + 2\left(\frac{r}{r_0}\right)^2\right] \tag{5.32}$$

Calculation of η_e^2:

The parameter η_e^2 represents the lag effect of droplet motion relative to the vapor fluctuation. For smaller particles, which are light enough to be carried by the continuous flow, $\eta_e^2 \approx 1$. However, for larger droplets, they cannot follow the turbulence components of vapor. Therefore, to accurately describe droplet motion in the PDO region, η_e^2 needs to be modified, considering the relative displacement between the droplets and the vapor phase.

The calculation of η_e^2 is based on the turbulence analysis in Hinze (1959):

$$\eta_e^2 = [1 + f_1(\omega_e)]^2 + f_2^2(\omega_e) \tag{5.33}$$

where

$$f_1(\omega_e) = \frac{\omega_e \left(\omega_e + c\sqrt{\frac{\pi\omega_e}{2}}\right)(b-1)}{\left(a + c\sqrt{\frac{\pi\omega_e}{2}}\right)^2 + \left(\omega_e + c\sqrt{\frac{\pi\omega_e}{2}}\right)^2} \tag{5.34}$$

$$f_2(\omega_e) = \frac{\omega_e \left(a + c\sqrt{\frac{\pi\omega_e}{2}}\right)(b-1)}{\left(a + c\sqrt{\frac{\pi\omega_e}{2}}\right)^2 + \left(\omega_e + c\sqrt{\frac{\pi\omega_e}{2}}\right)^2} \tag{5.35}$$

The ω_e is the most energetic frequency of fluid oscillation Lee and Wiesler (1987):

$$\omega_e = 67.6\, Re^{0.43} \tag{5.36}$$

a represents the interfacial drag effect. In the previous model of Hinze (1959), a is calculated according to Stokes' law:

$$a = \frac{36\mu}{(2\rho_d + \rho_v)d^2} \tag{5.37}$$

But the droplets have larger size compared to solid particles. Here, a drag force considering spherical drag law is included. Equation (5.37) can be rewritten as:

$$a = \frac{36\mu}{(2\rho_d + \rho_v)d^2\tau} \tag{5.38}$$

Where

$$\tau = \frac{24}{C_D\, Re_d} \tag{5.39}$$

C_D is the drag coefficient. Previously, $C_D = \frac{24}{Re_d}$, which implies $\tau = 1$. In the current model, C_D is calculated using the correlation developed by Morsi and Alexander (1972):

$$C_D = a_1 + \frac{a_2}{Re_d} + \frac{a_3}{Re_d^2} \tag{5.40}$$

The values of a_1, a_2, and a_3 vary depending on the range of Re_d (Morsi and Alexander, 1972).

With the obtained C_{nt}, η_e^2, and ε_v, Equation 5.16 for calculating droplet deposition mass flow rate in the PDO region is rewritten as:

$$m_{dep} = \frac{\eta_e^2\, k_\Theta r_0 u^*}{6 \cdot c_{ofu}} \left[1 - \left(\frac{r}{r_0}\right)^2\right] \left[1 + 2\left(\frac{r}{r_0}\right)^2\right] \frac{dC}{dy} A_{cr} \tag{5.41}$$

Where

$$r = r_{cr}, \quad dC = 2(C_c - C_{nt}), \quad dy = \frac{r_{cr} + r_0}{2}, \quad A_{cr} = 2\pi r_{cr} \Delta z$$

5.1.4 Wall-Vapor Convective Heat Transfer

Many correlations exist for predicting convective heat transfer between the wall and vapor. The model developed by Yu (2019) is employed. Yu divided the flow region along the heated length into a developing PDO region and a fully developed PDO region. In the developing PDO region, the convective heat transfer coefficient between the wall and vapor is described as a combination of the boiling heat transfer $h_{wv,NB}$ and the single-phase convective heat transfer $h_{wv,f}$:

$$h_{wv} = (1 - K_{wv})h_{wv,f} + K_{wv}h_{wv,NB} \tag{5.42}$$

Where $h_{wv,NB}$ is the nucleate boiling heat transfer coefficient (Chen, 1966), and $h_{wv,f}$ is the single vapor convective heat transfer coefficient. Yu (2019) modified the correlation with the viscosity ratio:

$$h_{wv,fdev} = 0.03675\frac{k_{vb}}{D_t}Re_{vb}^{0.743}Pr_{vb}^{0.4}\left(\frac{\mu_{vb}}{\mu_{vw}}\right)^{0.1} \tag{5.43}$$

where

$$Re_{vb} = \frac{GD_t x_a}{\mu_v \alpha} \tag{5.44}$$

$$Pr_{vb} = \frac{C_{p,v}\mu_v}{k_v} \tag{5.45}$$

A correlation of K_{wv} was fitted by Yu (2019) with experimental data:

$$K_{wv} = \frac{1}{1 + \left(\frac{10^4}{Re_v^{1/6.0}}\right)\left(\frac{L_{poi}}{L_{dev}}\right)^{2.5}} \tag{5.46}$$

L_{poi} is the heated length from the dryout point to the current calculation point, estimated by equilibrium quality difference. L_{dev} is predicted as:

$$L_{dev} = 900\, Re_v^{-0.008}\left(Bo + 10^{-4}\right)\left(\frac{\mu_d}{\mu_{vs}}\right)^{-0.55} \tag{5.47}$$

Where the boiling number Bo is:

$$Bo = \frac{q''_w}{Gh_{lg}} \tag{5.48}$$

and the Reynolds number is given by:

$$Re_v = \frac{GD_t}{\mu_{vs}} \tag{5.49}$$

5.2 Assessment of the Proposed PDO Model

In this part, the proposed model is assessed with KIT R-134a PDO experimental data (Köckert et al., 2021; Rensch et al., 2024) and KTH water PDO experimental data (Becker et al., 1983). The experimental data with void fraction at dryout point over 80% are selected from the database and used for the model assessment. The new developed droplet size correlation and validated Yoder droplet velocity correlation are implement. The newly developed droplet size model from Equation (4.11) in Chapter 4 is utilized to calculate the

droplet initial size at the dryout point. In the PDO heat transfer prediction, the interfacial heat transfer power is calculated by:

$$Q_{vd} = q''_{vd} \cdot A_d = h_{vd}(T_v - T_d) \cdot \pi d_{20}^2 \cdot \left(\frac{1-\alpha}{\frac{\pi}{6} d_{30}^3} \right) \cdot A_f \Delta z \tag{5.50}$$

or equivalently:

$$Q_{vd} = h_{vd}(T_v - T_d) \cdot \frac{6(1-\alpha) A_f \Delta z}{d_{32}} \tag{5.51}$$

Where A_f denotes the flow cross-sectional area, and A_d represents the interfacial heat transfer area. From Equation (5.50), the interfacial heat transfer area is the product of the droplet number and single droplet surface area. The droplet sizes d_{20} and d_{30} in Equation (5.50) correspond to the volume-mean diameter and surface-mean diameter, respectively. Consequently, the droplet size relevant for calculating interfacial heat transfer power is the sauter mean diameter d_{32}, which accounts for the effect of the droplet size distribution. According to Ueda's work (Ueda and Kim, 1982), a correction factor of 1.5 is applied to the arithmetic mean diameter d_{10} to obtain d_{32}. Therefore, based on Equation (4.11), the droplet size at dryout point is predicted by:

$$\frac{\rho_v u_v^2 d_{32}}{\sigma} = 1.5 \cdot 3 \times 10^{-4} Re_v^{1.2} \left(\frac{\rho_v}{\rho_d} \right) \tag{5.52}$$

The wall superheating predicted by the proposed model is validated against experimental data. The profile of the predicted wall superheating and heat transfer in PDO region are further analyzed using intermediate parameters obtained during the simulation, such as vapor superheating and interfacial heat transfer power. In addition, the performance of the proposed model and the literature models is evaluated by comparing their predicted heat transfer coefficients *htc* with experimental values and analyzing the corresponding prediction errors. Droplet size correlations from the literature are also implemented into the proposed PDO model for comparison.

5.2.1 Assessment with KIT R-134a Experimental Data

The database used for the assessment comes from Karlsruhe Institute of Technology (KIT) Model Fluid Facility (KIMOF). The refrigerant R-134a flows upward through a vertical round tube. This tube is uniformly heated and has an internal diameter of 10 mm and a heated length of 3000 mm. Detailed information about the experimental investigation can be found in the work of Rensch et al. (2024) and Köckert et al. (2021). A total of 4685 data points are selected with a selection criterion of a dryout void fraction over 80%. The parameter ranges of the selected KIT R-134a experimental data are:

Working Fluid:	R-134a
Heated Length:	3000 mm
Tube Inner Diameter:	10 mm
Pressure:	1.10 – 3.25 MPa
Mass Flux:	300 – 1500 kg/(m^2·s)
Heat Flux:	20 – 140 kW/m^2

5.2.1.1 Wall Temperature

In Figure 5.7, the scatter plot compares the wall superheating predicted by the proposed model with the experimentally measured values, based on the 4760 data points from KIT R-134a. Significant deviations between predicted and measured wall superheating predominantly occur in the regions close to the dryout point. A detailed error analysis of all data points reveals that the majority of points with larger deviations fall within 0.2 m downstream of the dryout location. This corresponds to the period of wall temperature jumping, where the flow has not yet stabilized into a dispersed flow, referred to as the developing PDO region.

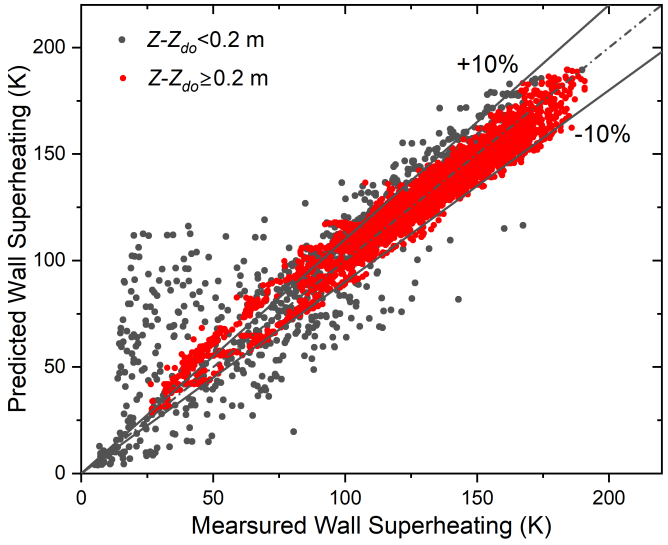

Figure 5.7: Comparison of predicted wall superheating and KIT R-134a measured wall superheating

Since the proposed model is developed for fully developed PDO heat transfer, all points within 0.2 m downstream of the dryout location are marked with black dots. It can be observed that the majority of predictions with errors exceeding the ±10% margin correspond to these points in black dots. The red dots in Figure 5.7 refer to the points that fall within the developed PDO region. Approximately 92% of the 3752 red data points in the developed PDO region fall within the ±10% error range. This indicates the high reliability of the model in predicting heat transfer in the developed PDO region.

5.2.1.2 Parameter Analysis

In the PDO region, the wall temperature profile exhibits two possible trends: increasing or decreasing with steam quality increase. Figure 5.8 illustrates the wall superheating profile at mass flux 300 kg/m^2·s and pressure 2.8 MPa, which displays an increase in the wall superheating as heat flux increases. Although the proposed model slightly underestimates the wall temperature, it accurately captures the temperature profile at low mass flux and also the effect of heat flux: higher heat flux results in larger wall temperature jumps and an increased maximum wall temperature in the PDO region.

The predicted superheating of vapor, ΔT_{vb}, at different heat flux is plotted against the distance from the dryout point, which is represented by the difference of equilibrium quality x_e and steam quality at the dryout point x_{do} in Figure 5.9(a). Since the proposed model assumes thermal equilibrium condition at dryout, the vapor superheating starts from 0 at the dryout point and increases with the distance from the dryout point. Figure 5.9(a)

shows that cases under different heat fluxes have close profiles of vapor superheating. At the end of the heated length, the vapor superheating has its maximum value of 30 K.

The predicted heat transfer coefficients by the proposed model are calculated according to Equation (5.53) to illustrate the variation of convective heat transfer under different conditions:

$$htc_{vb} = \frac{q''_w}{T_{w,cal} - T_{vb}} \tag{5.53}$$

In Figure 5.9(b), it can be seen that the three cases under different heat fluxes have close profiles of htc_{vb}. The htc_{vb} has an increasing trend in the developed PDO region since the droplet evaporation increases the vapor mass flux, enhancing the wall vapor convective heat transfer. However, since the degree of vapor superheating continuously increases at a relatively large rate, the effect of vapor superheating is stronger than the enhancement on convective heat transfer. Consequently, the wall superheating steadily rises in the PDO region.

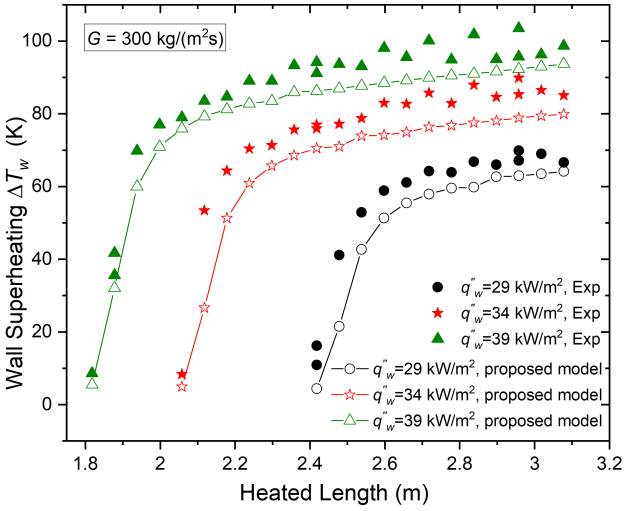

Figure 5.8: Wall superheating comparison between the proposed model and experimental data at low mass flux of pressure 2.8 MPa

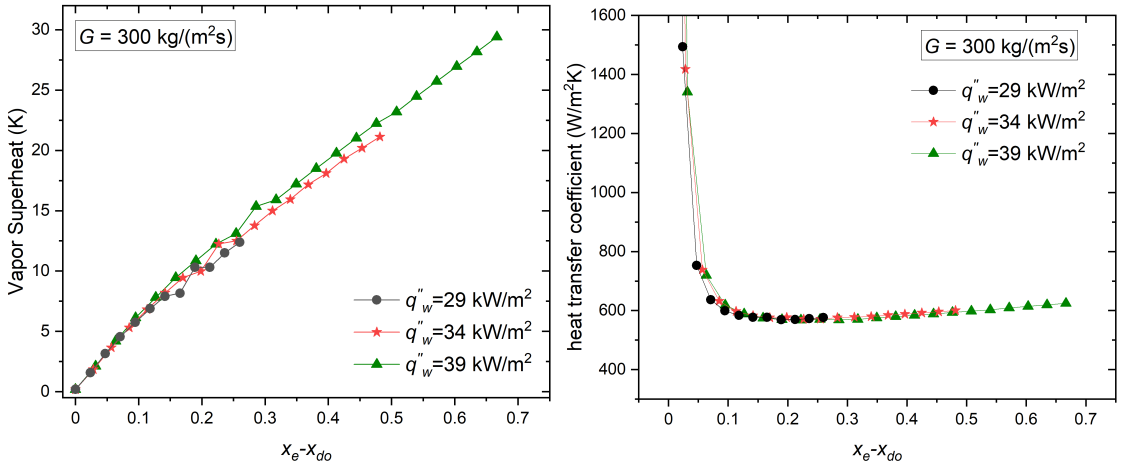

(a) ΔT_{vb} (b) htc_{vb}

Figure 5.9: Predicted superheating degree of bulk vapor ΔT_{vb} and predicted heat transfer coefficient htc_{vb} under low mass flux of pressure 2.8 MPa

Figure 5.10 presents the wall superheating profiles at high mass flux 1500 kg/m^2·s and pressure 1.1 MPa, where a decrease in wall temperature occurs in the developed PDO region. The proposed model reproduces this behavior in very high accuracy.

The predicted vapor superheating is displayed in Figure 5.11(a). At high mass flux, the profiles of vapor superheating at different heat fluxes are similar to each other. The increase rate of vapor superheating is slow and relatively small compared to that at low mass fluxes. The heat transfer coefficients htc_{vb} under high mass fluxes for three different heat fluxes are also displayed in Figure 5.11(b). The profile of htc_{vb} demonstrates an initial decline, followed by a significant increase in the developed PDO region. Due to the enhancement in the heat transfer coefficient outweighing the effect of the slowly rising vapor superheating, the wall temperature exhibits a decreasing trend under this condition.

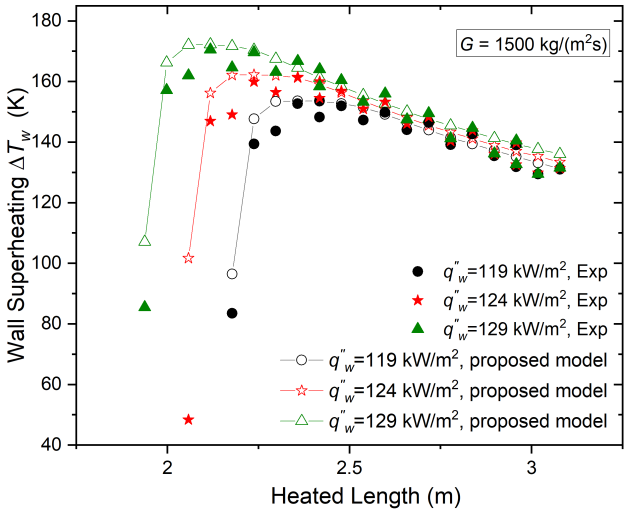

Figure 5.10: Wall superheating comparison between the proposed model and experimental data at high mass flux of pressure 1.1 MPa

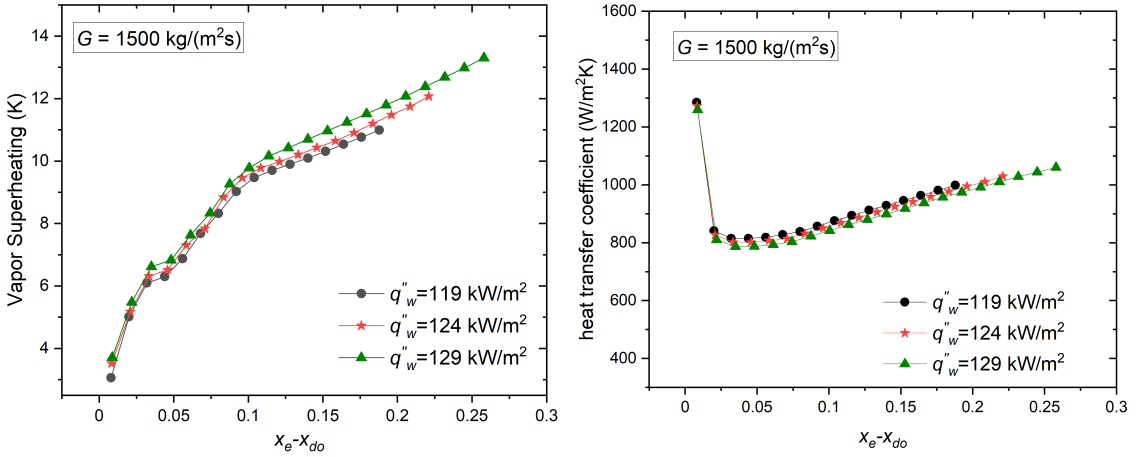

(a) ΔT_{vb} (b) htc_{vb}

Figure 5.11: Predicted superheating degree of bulk vapor ΔT_{vb} and predicted heat transfer coefficient htc_{vb} under high mass flux of pressure 1.1 MPa

The analysis of the results at different mass fluxes and heat fluxes reveals that variations in heat flux do not significantly affect the heat transfer pattern in the proposed model. Instead, mass flux is the primary factor influencing the wall temperature trend in the PDO region. To minimize the impact of other parameter variations, results obtained with three

mass fluxes at the same pressure and heat flux are selected for further analysis.

Figure 5.12 presents the profiles of wall superheating at constant pressure of 1.6 MPa (reduced pressure of 0.4) and heat flux of 94 kW/m^2 for 3 mass fluxes. The proposed model captures the developing trend of the PDO wall superheating well in different mass fluxes.

To understand the difference in wall superheating profiles predicted by the proposed model, the vapor temperature and interfacial heat transfer are displayed in Figure 5.13(a) and Figure 5.13(b), respectively. Figure 5.13(a) indicates that the increase rates of vapor

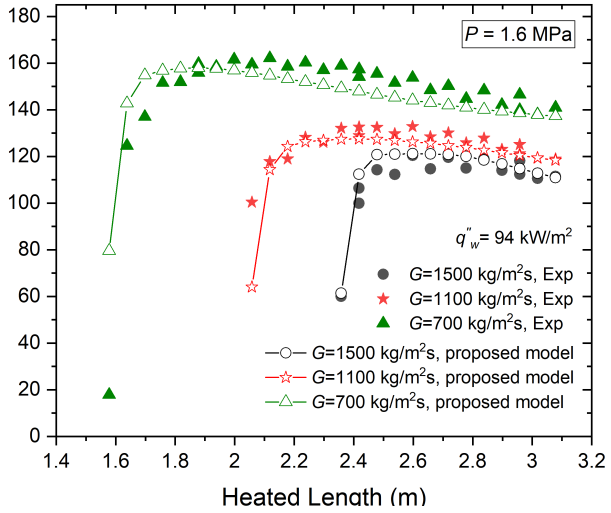

Figure 5.12: Wall superheating comparison between proposed model and experimental data under various mass fluxes

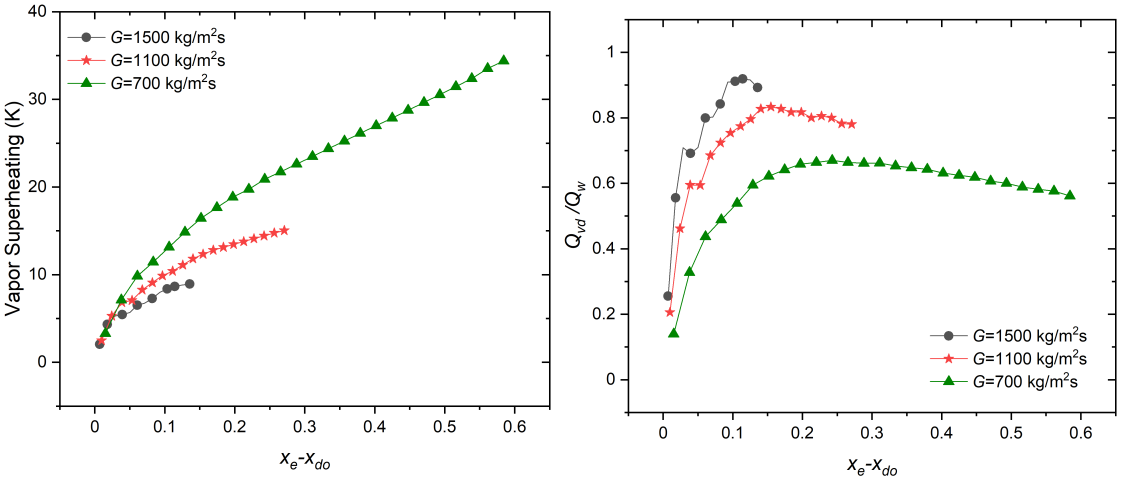

(a) ΔT_{vb} (b) htc_{vb}

Figure 5.13: Predicted superheating degree of bulk vapor ΔT_{vb} and predicted heat transfer coefficient htc_{vb} under various mass fluxes

superheating under different mass fluxes vary significantly. At low mass flux, the maximum superheat of bulk vapor reaches up to 35 K while at high mass flux it is only 10 K. This difference in vapor superheating can be explained in Figure 5.13(b), which displays the ratio of the heat power transferred from vapor to droplet Q_{vd} divided by the total heat power from the heated wall Q_w. It shows that the proportion of interfacial heat transfer

under different mass fluxes also differs greatly. At low mass flux, the interfacial heat transfer proportion reaches only about 60%, while at high mass flux, it approaches nearly 95%.

Analysis of intermediate parameters revealed that the disparity in interfacial heat transfer is primarily attributed to the larger portion of liquid left in the PDO region and the smaller droplet size caused by increased vapor velocity at high mass flux, which leads to a higher droplet interfacial area. Consequently, interfacial heat transfer efficiency is significantly enhanced under high mass flux conditions. Additionally, the convective heat transfer under high mass flux is highly efficient due to higher Reynolds number. As a result, the predicted wall temperature shows a decreasing trend in the developed PDO region.

5.2.2 Assessment with KTH Water Experimental Data

The KTH experimental data in water (Becker et al., 1983) is selected to further evaluate the proposed model. The KTH experiment is conducted in a vertically oriented tube, which is electrically and uniformly heated, with water flowing upwards. A total of 3968 data points, meeting the criterion of a void fraction greater than 80%, are selected for assessment. Here are the parameter ranges of the selected data points:

Working Fluid:	Water
Heated Length:	7000 mm
Tube Inner Diameter:	14.9 mm, 10 mm
Pressure:	3 – 16 MPa
Mass Flux:	500 – 3000 kg/(m^2·s)
Heat Flux:	147 – 1295 kW/m^2

5.2.2.1 Wall Temperature

Figure 5.14 presents a comparison of the predicted with the measured wall superheating based on KTH water data. To ensure the data in the fully developed PDO region, 3003

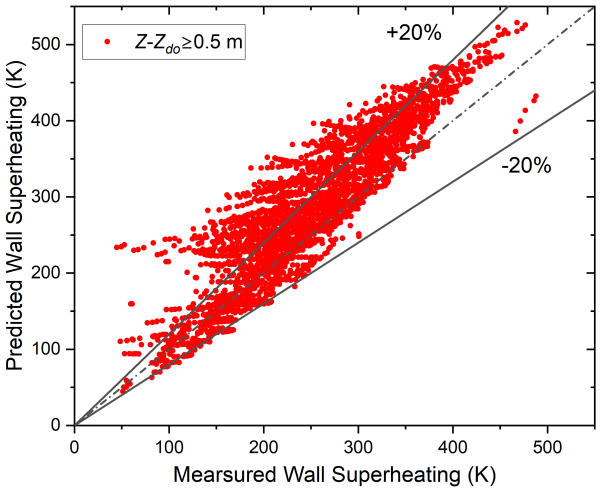

Figure 5.14: Comparison of the predicted wall superheating with the measured wall superheating

points located at least 0.5 m away from the dryout points are included. The scatter plot

reveals a slightly larger deviation with respect to the comparison with the KIT R-134a data in Figure 5.7. Despite this, approximately 67% fall within the ±20% margin, and 89% of the data points fall within the ±30% error margin, indicating that the model demonstrates reasonable predictive accuracy for the water data.

5.2.2.2 Parameter Analysis

Figures 5.15(a) and 5.15(b) present the profiles of the wall superheating for water at different heat fluxes under low and high mass fluxes, respectively. Consistent with the trends observed for the R-134a dataset in Figures 5.8 and 5.10, the wall superheating in water exhibits a gradual increase at low mass fluxes and a reduced slope under high mass fluxes in the developed PDO region. Differently, wall superheating in the PDO region for water is significantly higher than that observed for R-134a.

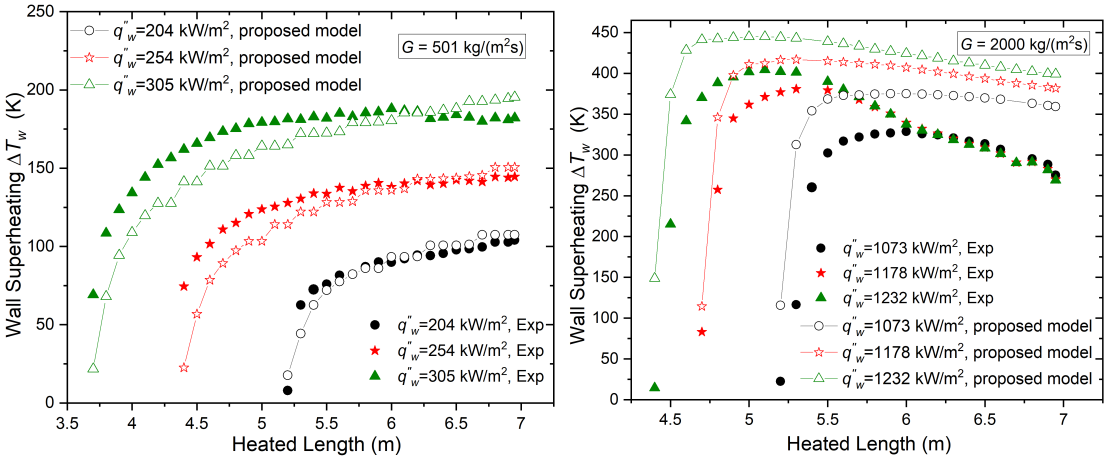

(a) Low mass flux of pressure 16 MPa

(b) High mass flux of pressure 5 MPa

Figure 5.15: Wall superheating comparison between proposed model and experimental data

Figure 5.15(a) shows that the predicted profile of the wall superheating aligns closely with the experimental results at different heat fluxes under low mass fluxes. Despite localized deviations as heat flux increases, the overall trend of the wall superheating profile is well captured. Figure 5.15(b) shows the wall superheating profile at high mass fluxes under different heat fluxes. Although the model overpredicts the wall superheating, it successfully captures the decreasing trend of the wall superheating at high mass fluxes. These results demonstrate that the model effectively predicts the wall superheating trends of water under both low and high mass flux conditions.

The actual vapor superheating and the interfacial heat transfer for water cases are also analyzed. As shown in Figure 5.16(a), the vapor superheating increases linearly with equilibrium steam quality at low mass fluxes, reaching up to 60 K. However, in Figure 5.16(b), the vapor superheating at high mass fluxes initially rises more steeply due to the sharp jump in wall temperature. Compared to the R-134a cases, the difference in vapor superheating between low and high mass fluxes is less pronounced, which may be attributed to the higher wall superheat predicted for water.

Analysis of the interfacial heat transfer in Figures 5.17(a) and 5.17(b) reveals that, at high mass fluxes, the contribution of interfacial heat transfer rapidly increases from zero to a dominant level, eventually stabilizing at approximately 90%. However, considering the overpredicted wall and vapor temperatures, this proportion may actually be underestimated under water conditions. This discrepancy could be mitigated by employing

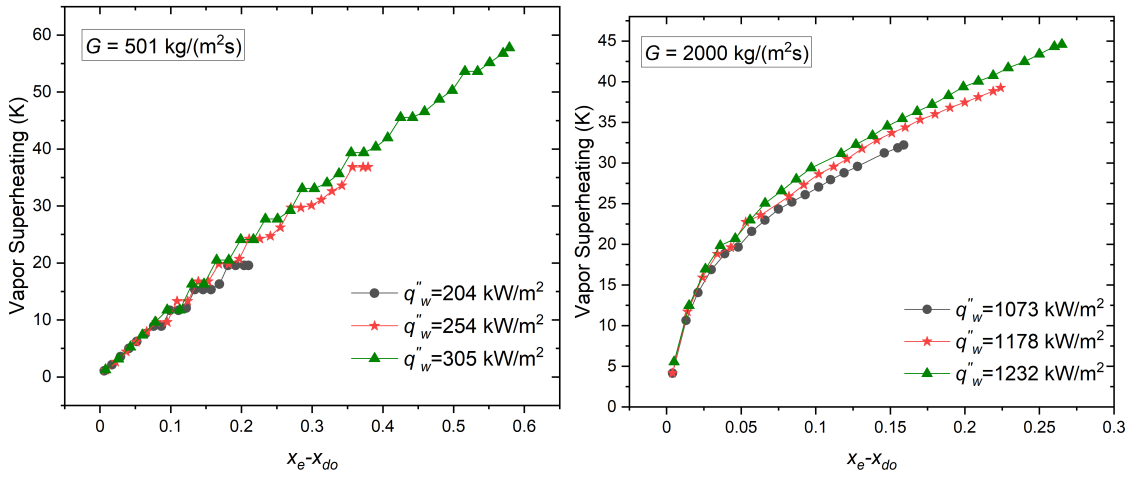

(a) Low mass flux of pressure 16 MPa (b) High mass flux of pressure 5 MPa

Figure 5.16: The predicted vapor superheating ΔT_{vb}

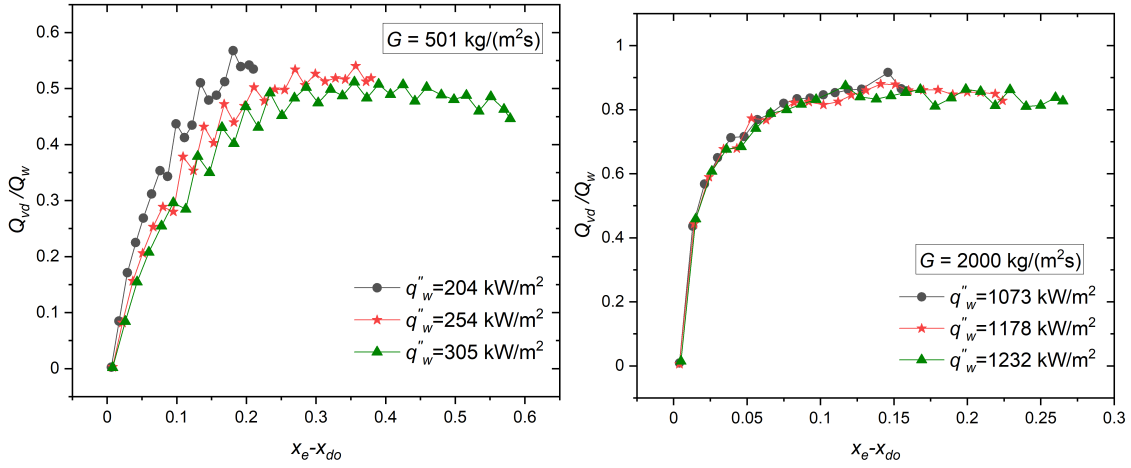

(a) Low mass flux of pressure 16 MPa (b) High mass flux of pressure 5 MPa

Figure 5.17: The predicted ratio of interfacial heat transfer power and total heat power from the wall

an improved droplet size model calibrated with water-specific data. Conversely, at low mass fluxes, the proportion of the interfacial heat transfer rises more gradually, peaking at around 60%. Along the heated length, droplet consumption reduces the droplet concentration, leading to a slight decrease in the proportion of interfacial heat transfer.

5.3 Comparison with literature models and correlations

5.3.1 Comparison with Existing PDO Models

Four models from the literature, i.e., Groeneveld equilibrium correlation (Groeneveld and Delorme, 1976), Chen non-equilibrium correlation (Chen et al., 1979), Rohsenow non-equilibrium differential model (Rohsenow, 1988), and Yu non-equilibrium mechanistic model (Yu, 2019), are selected for comparison with the proposed model. To quantitatively evaluate the predictive performance of these models, the heat transfer coefficient htc is defined as:

$$htc = \frac{q''_w}{T_w - T_{vs}} \tag{5.54}$$

For each data point, the error parameter is defined by:

$$\text{error}(i) = \frac{htc_{\text{cal}}(i) - htc_{\text{exp}}(i)}{htc_{\text{exp}}(i)} \tag{5.55}$$

where $htc_{\text{cal}}(i)$ is the predicted heat transfer coefficient of the i-th point, calculated using the predicted wall temperature, and $htc_{\text{exp}}(i)$ is the measured heat transfer coefficient, calculated from the measured wall temperature. Moreover, the mean error (ME) and root-mean-square (RMS) of the error parameter are defined as:

$$\text{ME} = \frac{1}{n}\sum_{i=1}^{n}\text{error}(i) \tag{5.56}$$

$$\text{RMS} = \sqrt{\frac{1}{n}\sum_{i=1}^{n}\text{error}(i)^2} \tag{5.57}$$

Accordingly, Table 5.1 exhibits the prediction errors of the proposed model and the four selected models from literature against the KIT R-134a experimental database. As can be seen, the Yu's (Yu, 2019) mechanistic model as well as the proposed mechanistic model perform better compared with other models. The proposed model, with a mean error of 0.32% and RMS of 18.42%, achieves the best prediction accuracy among the five models. The comparison with four selected models from the literature shows an obvious improvement by the proposed model.

Table 5.1: Assessment of various models based on the KIT R-134a experimental data

Model	**ME (%)**	**RMS (%)**
Proposed model	0.32	18.42
Yu model	4.39	24.35
Groeneveld model	17.22	44.13
Chen model	-25.00	48.39
Rohsenow model	41.20	52.91

As the assessment with R-134a data, the prediction errors of the heat transfer coefficient of the water dataset are calculated according to Equation (5.54)-(5.57) and compared with the four selected models, as summarized in Table 5.2. Among these models, Varone and Rohsenow (1986) demonstrated the smallest mean error of -3.91% and relatively small RMS error of 29.07%. However, considering its poor performance with the R-134a experimental data, the better performance with the water dataset might be attributed to Rohsenow's Nusselt correlation developed partially based on test data from water. In contrast, the proposed model still performs well for the water dataset by giving the smallest RMS error. This suggests that, while the proposed model generally underpredicts the *htc* in water PDO experimental data, it exhibits minimal error scattering. This is also illustrated in Figure 5.14, where the data points lie slightly above the diagonal line, indicating a slight underestimation of the heat transfer coefficient. This shows the proposed model can generally well predict the PDO heat transfer in both R-134a and water conditions.

Table 5.2: Comparison of the predicted heat transfer coefficient with the KTH experimental

Model	ME (%)	RMS (%)
Proposed model	-12.26	28.65
Rohsenow model	-3.91	29.07
Yu model	-13.36	29.68
Chen model	-23.13	51.39
Groeneveld model	58.31	100.16

5.3.2 Comparison with Existing Droplet Size Correlations

Several correlations for predicting the initial droplet size are implemented; among them, Yoder's correlation(Yoder and Rohsenow, 1983) and Ueda's droplet size correlation (Ueda and Kim, 1982) are selected to give a comparison in this section to facilitate a comparative analysis of droplet initial size. Implement Yoder's and Ueda's droplet size correlations instead of the new developed droplet size correlation into the current proposed PDO model, the results of predicted wall temperature and *htc* are showed below.

5.3.2.1 Wall Superheating

The predicted wall superheating related to the KIT R-134a database with Ueda's and the Yoder's correlations are shown in Figures 5.18. It is evident that Ueda's correlation worsens

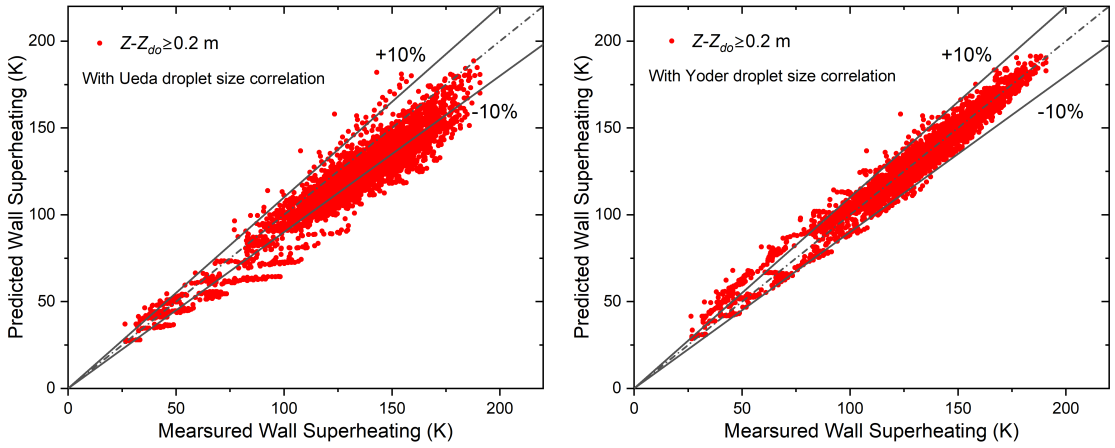

(a) With Ueda's droplet size correlation

(b) With Yoder's droplet size correlation

Figure 5.18: Predicted vs. measured wall superheating with the implement of varying droplet size correlations to proposed model (KIT database)

the wall superheating prediction, leading to a significant underestimation for a larger number of points. In contrast, the Yoder droplet size correlation provides much better prediction accuracy. Compared to the prediction results with new developed correlation shown in Figure 5.7, the predicted wall superheating using the Yoder correlation show only minor discrepancies, as seen in Figure 5.18(b).

Implementing the new droplet size correlation into the KTH Water database yields comparable overall performance. Figure 5.19 compare the predicted wall superheating with

the measured data using the Yoder's and the Ueda's droplet size correlation. As shown in Figure 5.19(a), Ueda's correlation substantially underestimates wall superheating for a significant portion of the cases. In contrast, Figure 5.19(b) shows that more predicted points using the Yoder size correlation fall within the +20% margin, indicating a slight tendency of better prediction results of wall superheating. However, the new size correlation helps the proposed PDO model improve accuracy in the high wall superheating region: data points that previously lay beyond the +20% margin now fall within it. This improvement

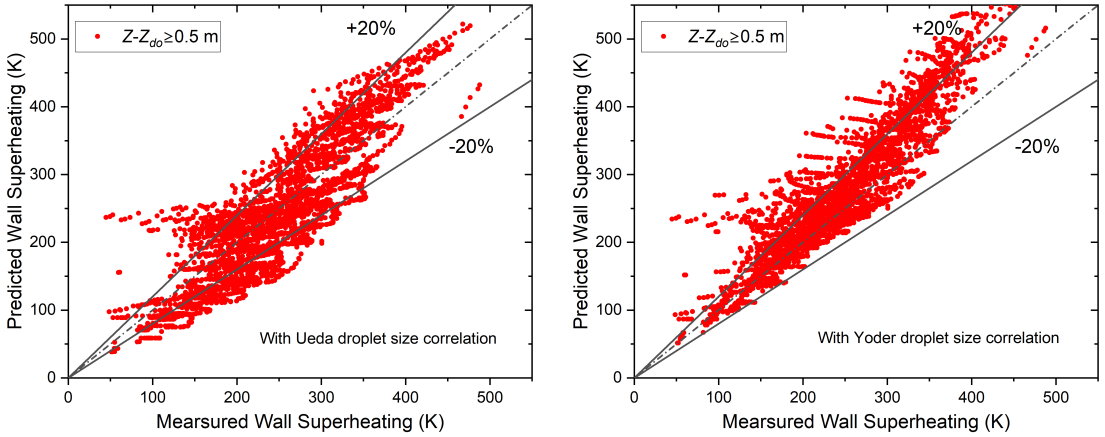

(a) With Ueda's droplet size correlation

(b) With Yoder's droplet size correlation

Figure 5.19: Predicted vs. measured wall superheating with the implement of varying droplet size correlations to proposed model (KTH database)

is consistent with observations from the KIT R-134a database, where the new correlation also effectively reduces overprediction under high wall superheating conditions.

5.3.2.2 Heat Tranfer Coefficient

The prediction errors of heat transfer coefficients with different droplet size correlations are displayed in Table 5.3. By analyzing the ME and RMS of the predicted heat transfer coefficient with Yoder's, Ueda's, and the new correlations, the proposed model with new droplet size correlation has smallest ME and RMS error, showing that the implement of new correlation in the proposed model improves the model prediction accuracy further. On the other hand, the implement of Ueda's correlation in proposed model performs very poorly for the KIT R-134a database. The prediction errors of heat transfer coefficients using

Table 5.3: Prediction errors of htc with various droplet size correlations based on the KIT R-134a experimental data

Model	**ME (%)**	**RMS (%)**
Proposed model with New correlation	0.32	18.42
Proposed model with Yoder correlation	-0.6	18.87
Proposed model with Ueda correlation	7.98	23.69

different droplet size correlations for the KTH water database are summarized in Table 5.4. Ueda's correlation yields the lowest mean error when implemented in the proposed model for the KTH water database. However, as illustrated in Figure 5.19(a), Ueda's correlation tends to significantly underpredict wall superheating, which is undesirable from a safety

analysis perspective. The implementation of the new droplet size correlation achieves the best performance for the KIT R-134a database but it provides slightly less accurate predictions than Yoder's correlation in the KTH water database. Nevertheless, the overall differences are minor. In both cases, the new correlation demonstrates superior overall performance compared to the existing models from the literature.

Table 5.4: Prediction errors of htc with various droplet size correlations based on the KTH Water experimental data

Model	ME (%)	RMS (%)
Proposed model with Yoder correlation	-11.68	27.69
Proposed model with New correlation	-12.26	28.65
Proposed model with Ueda correlation	1.93	32.99

5.3.2.3 Analysis on Predicted Droplet Size

To understand the variation in prediction results under different droplet size correlations, the droplet sizes at dryout points are calculated and presented in the Figure 5.20 and 5.21. For comparison, droplet sizes predicted by correlations of Equation (5.52), Yoder (1980) and Ueda and Kim (1982) are also presented.

Figure 5.20 displays the predicted droplet size with R-134a database. Figure 5.20(a) illustrates the variation of the predicted droplet size with inlet mass flux. Generally, all the predicted droplet sizes decrease with increasing mass flux. However, the droplet size predicted by the new correlation decreases more sharply as mass flux increases. At very high mass flux ranges, the predicted droplet size by the new correlation remains nearly constant as mass flux increases. The Ueda's correlation always provides the smallest droplet size predictions, which well explains the underprediction of wall superheating observed in Figure 5.18(a).

A mass flux of 300 kg/(m^2·s) is selected to investigate the effect of pressure on the predicted droplet size, as results at low mass flux are available over a wider pressure range. In Figure 5.20(b), the predicted droplet size initially increases with pressure and then decreases at higher pressures. The new correlation captures this turning trend similarly to Ueda's correlation, with a noticeable decrease in droplet size when the reduced pressure exceeds 0.7. In contrast, Yoder's correlation predicts a decrease beginning at a reduced pressure of 0.4. The droplet sizes predicted by the new correlation are significantly smaller than those predicted by Yoder's model at low pressures. Therefore, the smaller predicted wall superheating observed in the prediction results of new droplet size correlation can be explained by the smaller droplet sizes at low pressures, as lower pressure conditions typically result in higher wall temperatures in the PDO region.

The predicted droplet size with the water database are displayed in Figure 5.21. In the calculations, the model constrains droplet sizes exceeding 1 mm to a maximum of 1 mm. As shown in Figure 5.21(a), the predicted droplet size decreases with increasing mass flux, showing a similar trend as it does in the R-134a database.

In Figure 5.21(b), a mass flux of 500 kg/(m^2·s) is selected for examining the effect of pressure on the predicted droplet size. At low pressures, the predicted droplet size of the new correlation is close to that of Ueda's correlation and is significantly smaller than the Yoder's prediction. Similarly, this smaller droplet size at low pressure explains the smaller wall superheating predicted in Figure 5.14.

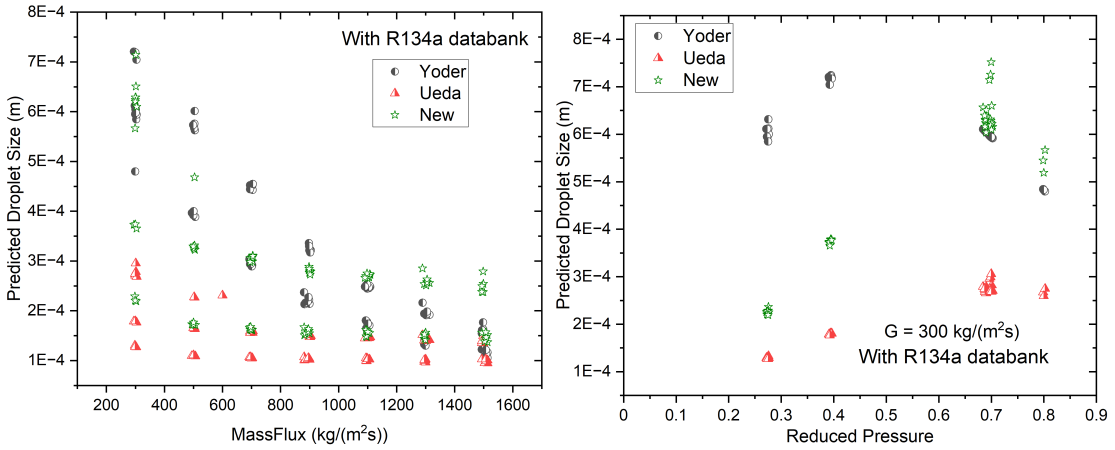

(a) Predicted droplet size vs. mass flux (b) Predicted droplet size vs. P_R

Figure 5.20: Predicted droplet size at dryout point with KIT database

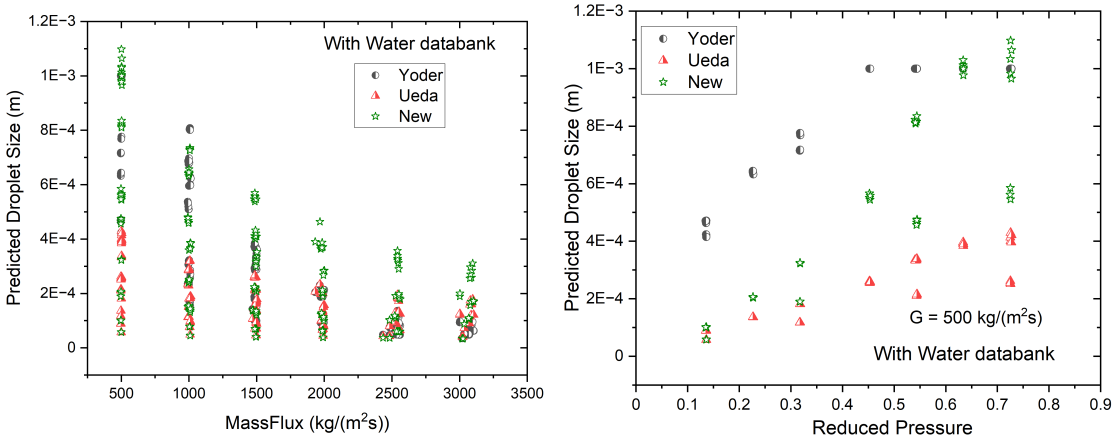

(a) Predicted droplet size vs. mass flux (b) Predicted droplet size vs. P_R

Figure 5.21: Predicted droplet size at dryout point with KTH database

The newly developed droplet size correlation demonstrates comparable accuracy to Yoder's correlation in predicting heat transfer coefficients, as both yield similar droplet size predictions. Moreover, the improved accuracy of the new correlation, particularly in high wall superheating cases, highlights its potential to enhance model reliability and performance in regions where existing correlations struggle. By capturing key physical mechanisms more effectively, the new droplet size model provides a more comprehensive representation of heat transfer behavior at extreme conditions. However, the current development and assessment of the new correlation are based on a limited set of experimental data on droplet size. Further experimental validation is required to refine and validate the proposed droplet size correlation over a broader parameter range.

5.4 Chapter Summary

This chapter introduces a two-region model for describing the process of interfacial heat transfer in the PDO region. The following results are obtained from the analyses of the PDO heat transfer in upward flow within a uniformly heated vertical tube, and its assessment with experimental data obtained in water and R-134a:

- A two-region model that considers the droplet evaporation in the central region and

near-wall region separately is developed for improving the prediction of interfacial heat transfer. A radial vapor temperature profile is fitted for interfacial heat transfer calculations. A new approach for counting the droplet lateral movement between the central and near-wall regions is also incorporated.

- Based on the single-phase correlation from literature and vapor parameters from CFD simulations, an improved correlation for the radial vapor temperature profile is fitted, which can account for the effect of droplet evaporation on the vapor temperature distribution.
- Since existing deposition correlations are inadequate for predicting droplet movement from the central region to the near-wall region, a new deposition correlation tailored to the two-region framework is derived. For applicability to PDO heat transfer, this correlation is further refined by incorporating vapor velocity profiles fitted from CFD simulations and accounting for the drag force on large droplets.
- A total of more than 8000 data points from both the KIT R-134a database and the KTH water database are selected to assess the proposed model. For the KIT R-134a database, 92% of the data points fall within a $\pm 10\%$ error margin related to the wall superheating, while for the KTH water database, 89% of the data points fall within a $\pm 30\%$ error margin. The model effectively predicts wall superheating in the developed PDO region across a wide range of operating conditions and working fluids.
- With the present mechanistic model, two different behaviors of wall superheating at different mass fluxes can be well explained. When the effect of the increased wall vapor convection outweighs the rise in vapor superheating, the wall superheating exhibits a decreasing trend. Conversely, when the vapor superheating increase dominates, the wall superheating continues to rise.
- When comparing the heat transfer coefficient with four existing prediction models from the literature, the proposed model demonstrates significantly improved accuracy for the KIT R-134a database and slightly better performance for the KTH water database. These results indicate that the present model provides reliable predictions on PDO heat transfer, offering a substantial improvement over existing models.
- During the assessment of droplet size correlations, Ueda's correlation, despite achieving reasonable accuracy with experimental data, performs poorly in PDO heat transfer, particularly when applying to the KIT R-134a database. Yoder's correlation performs well in PDO heat transfer prediction but exhibits large deviations when compared with the experimental droplet size data. In contrast, the new correlation demonstrates a satisfying performance in both the PDO heat transfer model and comparison with the experimental data of droplet size, indicating its superior reliability and overall accuracy.

6. Summary and Outlook

Summary

The current study investigates the droplet behaviors and heat transfer mechanisms in the PDO region through numerical simulations, experimental studies, and model development. The primary objectives are to enhance the understanding of droplet dynamics, improve droplet size and velocity correlations, and refine interfacial heat transfer models for more accurate analysis of PDO heat transfer and droplet behaviors. The most important original works and conclusions are summarized as follows:

Original Works

- CFD simulation on droplet behaviors and radial distribution of vapor parameters in PDO conditions.
- Experimental investigation of droplet behaviors in PDO conditions, leading to the development of a new droplet size correlation based on experimental data.
- Development and improvement of interfacial heat transfer model by incorporating CFD-derived findings.
- Mechanistic model development and refinement, integrating insights from CFD simulations and experimental results.

Conclusions

- Numerical simulation of droplet dynamics in the PDO region is conducted using a discrete particle model in ANSYS Fluent. The results show strong agreement with experimental data, validating the applied numerical methods and assumptions. The droplet mass flux exhibits a W-shaped radial distribution, with smaller droplets in the near-wall region due to higher evaporation rates. The contribution of near-wall evaporation to overall droplet evaporation is significant, emphasizing the importance of accurate initial droplet size estimation. Analysis of droplet deposition and entrainment reveals that evaporation inhibits deposition and enhances entrainment, with smaller droplets exhibiting higher deposition velocities. Higher wall temperatures further intensify evaporation, influencing droplet deposition behavior.

- The experimental investigation employs a high-speed camera to capture droplet parameters in the PDO region. By analyzing the image sequences, droplet size, velocity, and spatial distribution under various operating conditions are obtained. Results indicate that the radial droplet velocity distribution follows a standard normal distribution, while the axial velocity follows a shifted normal distribution, both strongly influenced by pressure and mass flux. Droplet size decreases with increasing heat flux and pressure. The observed trends in droplet size with respect to steam quality and pressure are consistent with findings reported in the literature. Existing literature correlations are evaluated and exhibit varying levels of predictive accuracy. To improve prediction, a new droplet size correlation is developed based on the Weber number, density ratio, and vapor Reynolds number, which significantly enhances predictive performance.
- Building on these findings, an improved mechanistic model for PDO heat transfer is developed. The model accounts for radial variation in droplet evaporation and lateral movement, leading to more accurate interfacial heat transfer representation. A new deposition correlation is proposed, considering vapor velocity profiles and drag forces on large droplets. The model is validated using experimental data from KIT (R-134a) and KTH (water), showing superior predictive accuracy over existing models. It also successfully captures trends in wall superheat under various inlet conditions and incorporates the newly developed droplet size correlation. Sensitivity analysis confirms that this correlation performs well in PDO model predictions.

Outlook

Despite the improvements achieved in this study, several aspects require further investigation:

- **CFD simulation limitations:** Current simulations focus on highly dry conditions due to the DPM applicability limit (droplet volume fraction $< 10\%$). However, typical PDO void fractions may reach 80%, requiring improved models for liquid volume fractions in the 10–20% range. Droplet collisions under such conditions should also be considered.
- **Additional experimental studies:** Further experiments on droplet behavior in PDO conditions are needed to further validate the proposed correlations.
- **Deposition modeling:** While deposition modeling has been improved, additional research should focus on incorporating droplet-induced turbulence modification in the near-wall region.
- **Heat transfer in the developing PDO region:** Significant discrepancies between predicted and measured data in the developing PDO region indicate a need for further study. Effects of wall-droplet heat transfer must be included for better accuracy.
- **Radiative heat transfer:** Although radiative transfer is negligible under typical conditions, it can become significant at high wall temperatures and should be included to extend the model's applicability.
- **Overestimation in water conditions:** The overestimation of heat transfer observed for water requires further analysis to identify and resolve the underlying causes.

Bibliography

Ahmad, S. (1970), "Axial distribution of bulk temperature and void fraction in a heated channel with inlet subcooling." *Journal of Heat Transfer*, 92, 595–609.

Akao, F., Araki, K., Mori, S., und Moriyama, A. (1980), "Deformation behaviors of a liquid droplet impinging onto hot metal surface." *Transactions of the Iron and Steel Institute of Japan*, 20, 737–743.

Andreani, M. und Yadigaroglu, G. (1989), "Dispersed flow film boiling: an investigation of the possibility to improve the models implemented in the nrc computer codes for the reflooding phase of the loca." Technical Report NUREG/IA-0042, PSI.

Andreani, M. und Yadigaroglu, G. (1997), "A 3-d eulerian-lagrangian model of dispersed flow film boiling including a mechanistic description of the droplet spectrum evolution-i. the thermal-hydraulic model." *International journal of heat and mass transfer*, 40, 1753–1772.

Anglart, H., Li, H., und Niewinski, G. (2018), "Mechanistic modelling of dryout and post-dryout heat transfer." *Energy*, 161, 352–360.

Annunziato, A., Cumo, M., und Pallazzi, G. (1983), "Post dry-out heat transfer in uncovered core accidents." In *Thermal hydraulics of nuclear reactors*, international topical meeting on nuclear reactor thermal hydraulics (ANS); Santa Barbara, CA (USA).

ANSYS Fluent (2021 R1), *ANSYS Fluent Theory Guide, ANSYS, Inc., Canonsburg.*

Bajorek, S. M. und Young, M. Y. (2000), "Direct-contact heat transfer model for dispersed-flow film boiling." *Nuclear Technology*, 132, 375–388.

Baumeister, K., Hamill, T., Schoessow, G., und Schwartz, F. (1965), "Film boiling heat transfer to water drops on a flat plate." Technical Report NASA TMX-52103, National Aeronautics and Space Administration · Washington, D.C.

Beal, S. K. (1970), "Deposition of particles in turbulent flow on channel or pipe walls." *Nuclear Science and Engineering*, 40, 1–11.

Beard, K. V. und Pruppacher, H. R. (1971), "A wind tunnel investigation of the rate of evaporation of small water drops falling at terminal velocity in air." *Journal of Atmospheric Sciences*, 28, 1455–1464.

Beattie, D. (1973), "A note on the calculation of two-phase pressure losses." *Nuclear Engineering and Design*, 25, 395–402.

Becker, K., Ling, C., Hedberg, S., und Strand, G. (1983), "An experimental investigation of post dryout heat transfer." Technical Report KTH-NEL-33, Royal Inst. of Tech.

Bennett, A., Hewitt, G., Kearsey, H., und Keeys, R. (1968), "Heat transfer to steam-water mixtures flowing in uniformly heated tubes in which the critical heat flux has been exceeded." Technical Report REP/AERE-R-5373, Atomic Energy Research Establishment, Harwell, Eng.

Birkhold, F. (2007), *Selektive katalytische Reduktion von Stickoxiden in Kraftfahrzeugen: Untersuchung der Einspritzung von Harnstoffwasserlösung*. Dissertation, University of Karlsruhe.

Bishop, A. A., Sandberg, R. O., und Tong, L. (1965), *Forced Convection Heat Transfer at High Pressure after the Critical Heat Flux*. New York, N.Y.: ASME.

Cebeci, T. und Bradshaw, P. (1984), *Physical and Computational Aspects of"Convective Heat Transfer*. Springer, New York.

Chan, S. und Grolmes, M. (1975), "Hydrodynamically-controlled rewetting." *Nuclear Engineering and Design*, 34, 307–316.

Chen, J. (1966), "Correlation for boiling heat transfer to saturated fluids in convective flow." *Industrial and engineering chemistry process design and development*, 5, 322–329.

Chen, J., Ozkaynak, F., und Sundaram, R. (1979), "Vapor heat transfer in post-chf region including the effect of thermodynamic non-equilibrium." *Nuclear Engineering and Design*, 51, 143–155.

Cheng, X., Feuerstein, F., Klingel, D., und Yu, D. (2018), "Mechanistic prediction of post dryout heat transfer and rewetting." *Kerntechnik*, 83, 203–207.

Cumo, M., Farello, G., Ferrari, G., und Palazzi, G. (1974), "On two-phase highly dispersed flows." *Journal of Heat Transfer*, 96, 496–503.

Cumo, M., Farello, G. E., und Ferrari, G. (1972), "The influence of curvature in post dryout heat transfer." *International Journal of Heat and Mass Transfer*, 15, 2045–2062.

Dittus, F. und Boelter, L. (1930), "Heat transfer in automobile radiators of the tubular type." *University of California Publications in Engineering*, 2, 443–461.

Dougall, R. (1963), *Film boiling on the inside of vertical tubes with upward flow of the fluid at low qualities*. Ph.D. thesis, Massachusetts Institute of Technology.

Downingm, C. G. (1966), "The evaporation of drops of pure liquids at elevated temperatures: Rates of evaporation and wet-bulb temperatures." *AIChE Journal*, 12, 760–766.

Era, A., Gaspari, G., Hassid, A., Milani, A., und Zavattarelli, R. (1966), "Heat transfer data in the liquid deficient region for steam-water mixtures at 70 kg/cm^2 flowing in tubular and annular conduits." Technical Report No. 11, Centro Informazioni Studi Esperienze, Italy.

Evans, D., Webb, S., und Chen, J. (1983), "Measurements of axially varying non-equilibrium in post critical-heat-flux boiling in a vertical tube." Technical Report NUREG/CR-3363, Lehigh Univ., USA. Inst. of Thermo-Fluid Engineering and Science.

Forslund, R. und Rohsenow, W. (1966), "Thermal non-equilibrium in dispersed flow film boiling in a vertical tube." Technical Report 75312-44, Cambridge, Mass.: MIT Dept. of Mechanical Engineering.

Forslund, R. und Rohsenow, W. (1968), "Dispersed flow film boiling." *Journal of Heat Transfer*, 90, 399–407.

Friedlander, S. K. und Johnstone, H. F. (1957), "Deposition of suspended particles from turbulent gas streams." *Industrial And Engineering Chemistry*, 49, 1151–1156.

Friend, W. L. und Metzner, A. B. (1958), "Turbulent heat transfer inside tubes and the analogy among heat, mass, and momentum transfer." *AIChE Journal*, 4, 393–402.

Frossling, N. (1938), "Uber die verdungtung fallenden tropfen." *Gerlands Beitrage Zur Geophysik*, 52, 170–216.

Ganic, E. N. (1976), *Post critical heat flux heat transfer*. Ph.D. thesis, Massachusetts Institute of Technology.

Ganić, E. und Rohsenow, W. (1977), "Dispersed flow heat transfer." *International Journal of Heat and Mass Transfer*, 20, 855–866.

Ganić, E. und Mastanaiah, K. (1981), "Investigation of droplet deposition from a turbulent gas stream." *International Journal of Multiphase Flow*, 7, 401–422.

Griffith, R. (1960), "Mass transfer from drops and bubbles." *Chemical Engineering Science*, 12, 198–213.

Groeneveld, D. (1972), *The thermal behaviour of a heated surface at and beyond dryout*. Ph.D. thesis, University of Western Ontario.

Groeneveld, D. und Delorme, G. (1976), "Prediction of thermal non-equilibrium in the post-dryout regime." *Nuclear Engineering and Design*, 36, 17–26.

Groeneveld, D. und Moeck, E. (1969), "An investigation of heat transfer in the liquid deficient regime." Technical Report AECL-3281(Rev.), Atomic Energy of Canada Ltd., Chalk River (Ontario). Chalk River Nuclear Labs.

Guo, Y. und Leung, L. (2005), "Developing film boiling heat transfer in tubes." In *The 11th International Topic Meeting on Nuclear Thermal-Hydraulics (NURETH11), Avignon, France*.

Guo, Y. und Mishima, K. (2002), "A non-equilibrium mechanistic heat transfer model for post-dryout dispersed flow regime." *Experimental thermal and fluid science*, 26, 861–869.

Hadaller, G. und Banerjee, S. (1969), "Heat transfer to superheated steam in round tubes." Technical Report WDI-147, AECL.

Heineman, J. (1960), "An experimental investigation of heat transfer to superheated steam in round and rectangular channels." Technical Report ANL-6213, Argonne National Lab.

Herkenrath, H., Mörk-Mörkenstein, P., Jung, K., und Weckermann, F. (1967), "Wärmeübergang am wasser bei erzwungener strömung im bereich von 140 bis 250 bar." Technical Report EUR 3658d, Europäische Atomgemeinschaft.

Hinze, J. O. (1959), *Turbulence*, 2nd edition. McGraw-Hill, New York.

Hughmark, G. A. (1967), "Mass and heat transfer from rigid spheres." *AIChE Journal*, 13, 1219–1221.

Hynek, S. (1969a), *Forced-convection, dispersed-flow film boiling*. Ph.D. thesis, Massachusetts Institute of Technology.

Hynek, Scott Josef; Rohsenow, W. M. B. A. E. (1969b), "Forced-convection, dispersed-flow film boiling." Technical Report 70586-63, Massachusetts Institute of Technology, Heat Transfer Laboratory.

Iloeje, Rohsenow, W. M., und Griffith, P. (1989), "Three-step model of dispersed flow heat transfer (post chf vertical flow." *Nigerian Journal of Technology*, 13, 1–15.

Issapour, I. und Lee, S. L. (1990), "Droplet deposition from a mist flow on a parallel vertical wall." *Particle & Particle Systems Characterization*, 7, 70–73.

Kastounis, A. (1987), "Post dryout correlations and models compared to experimental data from different fluids." In *Heat and Mass Transfer in Refrigeration and Cryogenics*, 152–164, Bougard, J., Afgan, N. (Eds.), Hemisphere, Washington, DC.

Kataoka, I., Ishii, M., und Mishima, K. (1983), "Generation and size distribution of droplet in annular two-phase flow." *Journal of Fluids Engineering*, 105, 230–238.

Kays, W. M. (1966), *Convective Heat and Mass Transfer*. McGraw-Hill, New York.

Keizo, M., Isao, K., und Kaichiro, M. (2005), "Post-dryout heat transfer analysis model with droplet lagrangian simulation." In *13th international conference on nuclear engineering*, Beijing (China).

Keizo, M., Isao, K., und Kaichiro, M. (2006), "Post-dryout heat transfer analysis model with droplet lagrangian simulation." *JSME International Journal Series B Fluids and Thermal Engineering*, 49, 377–383.

Kendall, G. und Rohsenow, W. (1978), "Heat transfer to impacting drops and post critical heat flux dispersed flow." Technical Report MIT-56987-100, Cambridge, Mass.: Heat Transfer Laboratory, Dept. of Mechanical Engineering.

Kim, Y. und Ban, C.-H. (2000), "Heat transfer correlation to predict the evaporation of a water droplet in superheated steam during reflood phase of a loca." *Journal of Energy Engineering*, 9, 261–268.

Köckert, L., Feuerstein, F., Yu, D., Klingel, D., und Cheng, X. (2018), "Experimental study of post-dryout heat transfer and rewetting in a r- 134a cooled vertical tube at comparable water cooled reactor pressure conditions." In *The 12th International Topical Meeting on Reactor Thermal-Hydraulics, Operation, and Safety (NUTHOS-12)*, Qingdao (China).

Köhler, W. und Hein, D. (1986), "Influence of the wetting state of a heated surface on heat transfer and pressure loss in an evaporator tube." Technical Report NUREG/IA-0003, Nuclear Regulatory Commission, Washington, DC (USA). Office of Nuclear Regulatory Research; Kraftwerk Union AG, Erlangen (Germany, FR).

Koizumi, Y., Ueda, T., und Tanaka, H. (1979), "Post-dryout heat transfer to r-113 upward flow in a vertical tube." *International Journal of Heat and Mass Transfer,*, 22, 669–678.

Kumari, N., Bahadur, V., Hodes, M., Salamon, T., Kolodner, P., Lyons, A., und Garimella, S. V. (2010), "Analysis of evaporating mist flow for enhanced convective heat transfer." *International Journal of Heat and Mass Transfer*, 53, 3346–3356.

Kuznetsov, G., Strizhak, P., und Volkov, R. (2020), "Heat exchange of an evaporating water droplet in a high-temperature environment." *International Journal of Thermal Sciences*, 150, 106227.

Köckert, L., Badea, A. F., Cheng, X., Yu, D., und Klingel, D. (2021), "Studies on heat transfer in r-134a vertical flow." *International Journal of Advanced Nuclear Reactor Design and Technology*, 3, 44–53.

Köckert, L., Liu, W., und Cheng, X. (2024), "Post-dryout heat transfer in circular tubes using r-134a: experiment and correlation assessment." *Heat and Mass Transfer*, 60, 1453–1466.

Laufer, J. (1954), "The structure of turbulence in fully developed pipe flow." Technical Report 1174, NACA.

Laverty, W. und Rohsenow, W. (1964), "Film boiling of saturated liquid flowing upward through a heated tube: high vapor quality range." Technical Report 9857-32, Cambridge, Mass.: MIT Dept. of Mechanical Engineering.

Lee, K. und Ryley, D. (1968), "The evaporation of water droplets in superheated steam." *Journal of Heat Transfer*, 90, 445–451.

Lee, R. und Almenas, K. (1982), "Droplet deposition above a quench front during reflood." *Trans. Am. Nucl. Soc.*, 43.

Lee, S. L. und Durst, F. (1982), "On the motion of particles in turbulent duct flows." *International Journal of Multiphase Flow*, 8, 125–146.

Lee, S. L. und Wiesler, M. A. (1987), "Theory on transverse migration of particles in a turbulent two-phase suspension due to turbulent diffusion-i." *International Journal of Multiphase Flow*, 13, 99–111.

Li, H. und Anglart, H. (2015), "Cfd model of diabatic annular two-phase flow using the eulerian-lagrangian approach." *Annals of Nuclear Energy*, 77, 415–424.

Li, H. und Anglart, H. (2016), "Prediction of dryout and post-dryout heat transfer using a two-phase cfd model." *International Journal of Heat and Mass Transfer*, 99, 839–850.

Liesch, K., Raemhild, G., und Hofmann, K. (1975), "Zur Bestimmung des Wärmüberganges und der kritischen Heizflächenbelastung im Hinblick auf besondere Verhältnisse in den Kühlkanälen eines DWR bei schweren Kühlmittelverlustunfällen." Technical Report MRR 150, Laboratorium für Reaktorregelung und Anlagensicherung.

Lin, J., Zhang, X., Huang, X., und Chen, L. (2022), "Numerical simulation study on the flow and heat transfer characteristics of subcooled n-heptane flow boiling in a vertical pipe under external radiation." *Energies*, 15.

Lin, T., Jou, J., und Hwang, C. (1989), "Turbulent forced convective heat transfer in two-phase evaporating droplet flow through a vertical pipe." *International Journal of Multiphase Flow*, 15, 997–1009.

Liu, B. und Ilori, T. (1974), "Aerosol deposition in turbulent pipe flow." *Environmental Science and Technology*, 8, 351–356.

Lopes, J. C. und Dukler, A. E. (1985), "Droplet sizes, dynamics and deposition in vertical annular flow." Technical Report NUREG/CR-4424, Houston Univ., TX (USA). Dept. of Chemical Engineering.

Malhotra, A. und Kang, S. (1984), "Turbulent prandtl number in circular pipes." *International Journal of Heat and Mass Transfer*, 27, 2158–2161.

Mastanaiah, K. und Ganic, E. N. (1981), "Heat transfer in two-component dispersed flow." *Journal of Heat Transfer*, 103, 300–306.

Mawatari, T. und Mori, H. (2016), "An experimental study on characteristics of post-chf heat transfer in the high subcritical pressure region near to the critical pressure." *Journal of Thermal Science and Technology*, 11, JTST0006–JTST0006.

McCoy, D. und Hanratty, T. (1977), "Rate of deposition of droplets in annular two-phase flow." *International Journal of Multiphase Flow*, 3, 319–331.

Meholic, M. (2011), *The development of a non-equilibrium dispersed flow film boiling heat transfer modeling package*. Ph.D. thesis, The Pennsylvania State University.

Miropolskiy, Z. L. (1963), "Heat transfer in film boiling of a steamwater mixture in steam cenerating tubes." *Teplonergetika*, 10, 49–53.

Moose, R. und Ganić, E. (1982), "On the calculation of wall temperatures in the post dryout heat transfer region." *International Journal of Multiphase Flow*, 8, 525–542.

Morsi, S. A. und Alexander, A. J. (1972), "An investigation of particle trajectories in two-phase flow systems." *Journal of Fluid Mechanics*, 55, 193–208.

Nijhawan, S., Chen, J., Sundaram, R., und London, E. (1980), "Measurement of vapor superheat in post-critical-heat-flux boiling." *Journal of Heat Transfer*, 102, 465–470.

Nishikawa, K., Yoshida, S., Mori, H., und Takamatsu, H. (1983), "An experiment on the heat transfer characteristics in the post-burnout region at high subcritical pressures." *Nuclear Engineering and Design*, 74, 233–239.

Nishikawa, K., Yoshida, S., Mori, H., und Takamatsu, H. (1986), "Post-dryout heat transfer to freon in a vertical tube at high subcritical pressures." *International journal of heat and mass transfer*, 29, 1245–1251.

Paleev, I. und Filippovich, B. (1966), "Phenomena of liquid transfer in two-phase dispersed annular flow." *International Journal of Heat and Mass Transfer*, 9, 1089–1093.

Parker, J. D. und Grosh, R. J. (1961), "Heat transfer to a mist flow." Technical Report ANL-6291, Argonne National Laboratory Subcontract.

Plummer, D., Iloeje, O., Rohsenow, W., Griffith, P., und Ganic, E. (1974), "Post critical heat transfer to flowing liquid in a vertical flow." Technical Report 72718-91, Massachusetts Institute of Technology, Heat Transfer Laboratory.

Ranz, W., Marshall, W., et al. (1952), "Evaporation from drops." *Chem. Eng. Prog*, 48, 141–146.

Reichardt, H. (1951), "Vollstandige darstellung der turbulenten geschwindigkeitsverteilung in glatten leitungen." *Zeitschrift für Angewandte Mathematik und Mechanik*, 31, 208–219.

Renksizbulut, M. und Yuen, M. C. (1983), "Experimental Study of Droplet Evaporation in a High-Temperature Air Stream." *Journal of Heat Transfer*, 105, 384–388.

Rensch, N., Köckert, L., Badea, A. F., und Cheng, X. (2024), "Experimental investigation of post-dryout heat transfer with r-134a at high pressures." *Nuclear Science and Engineering*, 1–20.

Rohsenow, W. (1988), "Post dryout heat transfer prediction method." *International communications in heat and mass transfer*, 15, 559–569.

Saha, P. (1980), "A nonequilibrium heat transfer model for dispersed droplet post-dryout regime." *International Journal of Heat and Mass Transfer*, 23, 483–492.

Schnitter, R. (1982), *Untersuchungen zum Warmeübergang bei Vertikalen und Horizontalen Rohrströmungen im Post-dryout-bereich.* Ph.D. thesis, TU-Hannover.

Shah, M. M. (2017), "Comprehensive correlation for dispersed flow film boiling heat transfer in mini/macro tubes." *International Journal of Refrigeration*, 78, 32–46.

Shah, M. und Siddiqui, M. (2000), "A general correlation for heat transfer during dispersed-flow film boiling in tubes." *Heat transfer engineering*, 21, 18–32.

Shi, J., Sun, B., Han, W., Zhang, G., Li, Y., und Yang, L. (2016a), "Numerical simulation of dryout and post-dryout heat transfer in a straight-pipe once-through steam generator." *Applied Thermal Engineering*, 105, 132–141.

Shi, J., Sun, B., Zhang, G., Song, F., und Yang, L. (2016b), "Prediction of dryout and post-dryout wall temperature at different operating parameters for once-through steam generators." *International Journal of Heat and Mass Transfer*, 103, 66–76.

Song, M. (2021), *Modelling of CHF and Post-CHF Heat Transfer for Trans-critical Transients.* Ph.D. thesis, Karlsruher Institut für Technologie (KIT).

Sozer, A., Anklam, T., und Dodds, H. (1984), "Convection-radiation heat transfer to steam in rod bundle geometry." *Nuclear technology*, 67, 452–462.

Sugawara, S. (1990), "Droplet deposition and entrainment modeling based on the three-fluid model." *Nuclear Engineering and Design*, 122, 67–84.

Sun, K., Gonzalez-Santalo, J., und Tien, C. (1976), "Calculations of combined radiation and convection heat transfer in rod bundles under emergency cooling conditions." *Journal of Heat Transfer*, 98, 414–420.

Swenson, H. S., Carver, J. R., und Szoeke, G. (1962), "The Effects of Nucleate Boiling Versus Film Boiling on Heat Transfer in Power Boiler Tubes." *Journal of Engineering for Power*, 84, 365–371.

Tatterson, D. F., Dallman, J. C., und Hanratty, T. J. (1977), "Drop sizes in annular gas-liquid flows." *AIChE Journal*, 23, 68–76.

Torfeh, S. und Kouhikamali, R. (2015), "Numerical investigation of mist flow regime in a vertical tube." *International Journal of Thermal Sciences*, 95, 1–8.

Ueda, T. (1979), "Entrainment rate and size of entrained droplets in annular two-phase flow." *Bulletin of JSME*, 22, 1258–1265.

Ueda, T. und Kim, K. (1982), "Dryout heat flux and size of entrained drops in a flow boiling system." *Bulletin of JSME*, 25, 225–233.

Varone, A. F. und Rohsenow, W. M. (1986), "Post dryout heat transfer prediction." *Nuclear Engineering and Design*, 95, 315–327.

Varone, A. (1990), *The influence of the dispersed phase on the convective heat transfer in dispersed flow film boiling.* Ph.D. thesis, Massachusetts Institute of Technology.

Vojtek, I. (1978), "Auswertung der 25-Stabbündel-Versuche mit dem Rechenprogramm BRUDIVA." Technical Report GRS-A-208, Gesellschaft für Anlagen- und Reaktorsicherheit (GRS).

Winterton, R. (1998), "Where did the dittus and boelter equation come from?" *International Journal of Heat and Mass Transfer*, 41, 809–810.

Wu, P., Ren, Y., Feng, M., Shan, J., Huang, Y., und Yang, W. (2022), "A review of existing supercritical water reactor concepts, safety analysis codes and safety characteristics." *Progress in Nuclear Energy*, 153, 104409.

Xia, Z. und Cheng, X. (2025a), "A new mechanistic model for post-dryout heat transfer based on two-region approach." *International Journal of Heat and Mass Transfer*, 245, 127035.

Xia, Z. und Cheng, X. (2025b), "Numerical investigation on droplet lateral movement in post-dryout region." *International Journal of Heat and Mass Transfer*, 237, 126448.

Xia, Z., Cheng, X., und Liu, W. (2024), "Cfd simulation on droplet behavior in post-dryout region." *Kerntechnik*, 89, 124–132.

Yang, Z. H. und Lee, S. L. (1991), "On the droplet deposition and mist supercooling in a turbulent channel flow." *Particle & Particle Systems Characterization*, 8, 72–78.

Yao, W. und Morel, C. (2004), "Volumetric interfacial area prediction in upward bubbly two-phase flow." *International Journal of Heat and Mass Transfer*, 47, 307–328.

Yoder, G. und Rohsenow, W. (1983), "A solution for dispersed flow heat transfer using equilibrium fluid conditions." *Journal of Heat Transfer*, 105, 10–17.

Yoder, GL; Rohsenow, W. (1980), "Dispersed flow film boiling." Technical Report 85694-103, Massachusetts Institute of Technology. Heat Transfer Laboratory.

Yu, D. (2019), *Analysis and Modelling of Full-Range Post-Dryout Heat Transfer in Vertical Tubes*. Ph.D. thesis, Karlsruher Institut für Technologie.

Yuen, M. und Chen, L. (1978), "Heat-transfer measurements of evaporating liquid droplets." *International Journal of Heat and Mass Transfer*, 21, 537–542.

Zhong, Y., Hu, L., Chen, D., Liu, H., Yuan, D., und Liu, W. (2019), "CFD simulation on the flow and heat transfer characteristics of mist flow in wire-wrapped rod bundle." *Nuclear Engineering and Design*, 345, 62–73.

List of Publications

During Ph.D.

Xia, Zihan, & Cheng, Xu. (2025), "A new mechanistic model for post-dryout heat transfer based on two-region approach," *International Journal of Heat and Mass Transfer*, 245, 127035.

Xia, Zihan, & Cheng, Xu. (2025), "Numerical investigation on droplet lateral movement in post-dryout region," *International Journal of Heat and Mass Transfer*, 237, 126448.

Xia, Zihan, Cheng, Xu, & Liu, Wei. (2024), "CFD simulation on droplet behavior in post-dryout region," *Kerntechnik*, 89(2), 124–132.

Xia, Zihan, & Cheng, Xu. (2024), "Investigation on Development of New Mechanistic Model for Post Dryout Heat Transfer," *Proceedings of the 31st International Conference on Nuclear Engineering (ICONE-31)*.